ABSTRACT

PROPAGATION AND SCATTERING OF BEAM WAVES IN VEGETATION USING SCALAR TRANSPORT THEORY

by

Michael Yu-Chi Wu

Vegetation is a very complex propagation medium, and multiple scattering effects play a significant role in the propagation of microwave and millimeter (mm)-wave signals through foliage. At frequencies above 1 GHz, both the coherent and incoherent field components have to be taken into account and vegetation has to be modeled as a random medium of discrete scatterers having a wide variety of sizes and shapes. Multiscattering can be studied effectively by using transport theory. In prior studies, theories have been developed for microwave and mm-wave propagation in vegetation using transport theory for continuous wave and pulsed signals. In this study, the theory has been extended to the more realistic cases of incident fields in the form of pulsed beam waves that are confined within a specified solid angle. Such spherical or diverging incident beam waves are very important in many practical applications since millimeter, optical and acoustic waves are often confined within a small conical angle. For spherical beam waves that propagate in vegetation, the range dependence, the effects of angular spread (beam broadening), and pulse broadening are determined. Pulse broadening is important especially in digital communications, where it may cause intersymbol interference and—depending on the data rate—a significant increase in bit error rate.

The specific problem that is analyzed is that of a periodic sequence of spherical pulses incident from free space (air) onto a forest region (vegetation). The forest is modeled as a half-space of randomly distributed particles, which scatter and absorb electromagnetic energy. The incident pulse train under investigation, as mentioned before, is a characteristic of the radiation produced by a microwave or mm-wave antenna.

PROPAGATION AND SCATTERING OF BEAM WAVES IN VEGETATION USING SCALAR TRANSPORT THEORY

by

Michael Yu-Chi Wu

A Dissertation

Submitted to the Faculty of

New Jersey Institute of Technology

in Partial Fulfillment of the Requirements for the Degree of

Doctor of Philosophy in Electrical Engineering

Department of Electrical and Computer Engineering

January 2008

APPROVAL PAGE

PROPAGATION AND SCATTERING OF BEAM WAVES IN VEGETATION USING SCALAR TRANSPORT THEORY

Michael Yu-Chi Wu

Dr. Gerald M. Whitman, Dissertation Advisor — Date
Professor of Electrical and Computer Engineering, NJIT

Dr. Felix K. Schwering — Date
Chief Scientist (retired), CECOM, Fort Monmouth, NJ

Dr. Gregory A. Kriegsmann — Date
Distinguished Professor of Mathematical Sciences, NJIT

Dr. Edip Niver — Date
Professor of Electrical and Computer Engineering, NJIT

Dr. Peter G. Petropoulos — Date
Associate Professor of Mathematical Sciences, NJIT

Dr. Marek Sosnowski — Date
Professor of Electrical and Computer Engineering, NJIT

Dr. Leonid Tsybeskov — Date
Professor of Electrical and Computer Engineering, NJIT

BIOGRAPHICAL SKETCH

Author: Michael Yu-Chi Wu

Degree: Doctor of Philosophy

Date: January 2008

Undergraduate and Graduate Education:

- Doctor of Philosophy in Electrical Engineering,
  New Jersey Institute of Technology, Newark, NJ, 2008
- Master of Science in Electrical Engineering,
  New Jersey Institute of Technology, Newark, NJ, 2001
- Master of Science in Computer Science,
  New Jersey Institute of Technology, Newark, NJ, 2000
- Bachelor of Science in Electrical Engineering,
  New Jersey Institute of Technology, Newark, NJ, 1998

Major: Electrical Engineering

Publication:

Whitman, G. M. , Scherwing, F. K., Wu, M. Y. (2007, June). Collimated Beam Wave Pulse Propagation and Scattering in Vegetation Using Scalar Transport Theory. IEEE Transactions on Antennas and Propagation 55(6), 1599-1612.

To my father, Ming Hong Wu.【吳明宏】

To my mother, Diane Li-Chun Wu.【吳楊麗娟】

To my elder brother, Andrew Yu-Bing Wu.【吳宇浜】

To my younger sister, Cheryl Tsai-Luen Wu.【阮吳采瑜】

And to my youngest sister, Rachel Tsai-Han Wu.【吳采涵】

Regards,

Michael Yu-Chi Wu

吳宇奇敬

ACKNOWLEDGMENT

I would like to express my sincere gratitude to Dr. Gerald M. Whitman as a professor and as a research advisor for his patience, guidance, and elucidation on theories and concepts throughout this dissertation. I would also like to thank Dr. Felix K. Schwering for his generous contributions to the analytical development of the theory presented here. Moreover, I am grateful to Dr. Peter G. Petropolous for sharing some of the ideas to the numerical problem. Special thanks are given to Dr. Felix K. Schwering, Dr. Gregory A. Kriegsmann, Dr. Edip Niver, Dr. Peter G. Petropolous, and Dr. Marek Sosnowski, and Dr. Leonid Tsybeskov for serving on the dissertation committee.

I would like to express my appreciation to Greg Recine for his generosity in helping me gain access to the BeoWulf clusters at Stevens Institute of Technology; and Gedeliah Wolosh and David Perel for their assistance in expediting my use of kong.njit.edu, the AMD Opteron Clusters.

In addition, I would like to thank my parents, Dr. Ming-Hong Wu and Diane Wu, for supporting me and encouraging me to complete this research and dissertation.

TABLE OF CONTENTS

TABLE OF CONTENTS

(Continued)

LIST OF FIGURES

LIST OF FIGURES
(Continued)

LIST OF FIGURES
(Continued)

Figure Page

TABLE OF DISCRETE VARIABLES

Variable	Definition
c	Speed of the wave. Note: $c = 299,792,458\left[\text{m/s}\right]$ for the speed of the wave in the air region.
$\sigma_s, \sigma_a, \sigma_t$	Scatter, absorption, and extinction (total) cross-section per unit volume; these coefficients determine how much energy the objects (trees, leaves, etc.) in the random medium (vegetation) are scatter and absorb, and they are obtained empirically. Note: $\sigma_t = \sigma_s + \sigma_a$
$\Delta\gamma_s, \alpha$	These parameters are used in the phase function or the scatter power function of the discrete scatterers and are used to determine the pattern how the power is scattered
W_0	The albedo; note: $W_0 = \sigma_s / \sigma_t$
n, z_0, z_0', R_0, R_0'	The defining parameters of the transmitting antenna: cosine power factor of the pattern function (it determines the spherical beam width) and the on-axis distance between the transmitting antenna placed externally to the random medium (vegetation) and the random medium; note: $z_0' = \sigma_t z_0$ and $R_0' = z_0' / \cos\theta_0$.
ω_c	Carrier angular frequency of the pulse trains
$\overline{r}, \overline{r}'$	Positional vector, i.e. $\overline{r}' = \sigma_t \overline{r} = \rho'\hat{\rho} + z'\hat{z}$
∇, ∇'	Gradient and normalized gradient
ρ, ρ'	ρ is the positional radius on the *xy* plane; note: $\rho = \sqrt{x^2 + y^2}$. $\rho' = \sigma_t \rho$ is the normalized ρ.
z, z'	z is the normalized distance into the vegetation (penetration depth). $z' = \sigma_t z$ is the normalized z.
ϕ_x	Azimuthal angle in the *xy*-plane measured positive from the positive *x*-axis; note: $\tan\phi_x = y / x$; see Ψ.

TABLE OF DISCRETE VARIABLES
(Continued)

Variable	Definition
θ_0, μ_0	θ_0 is the radiation angle of the transmitting antenna, measured positively from the positive direction of the z-axis; note: $\tan\theta_0 = \rho / z$; $\mu_0 = \cos\theta_0$ used for change of variable θ_0.
R, R'	Positional radius and normalized positional radius from the transmitting antenna at z_0 to the point of observation in the forest. $R = \sqrt{\rho^2 + (z + z_0)^2}$ and $R' = \sigma_t R = \sqrt{\rho'^2 + (z' + z_0')^2}$.
x, y, x', y'	Positions and normalized positions in the rectangular coordinate system; see ρ and ϕ_x for the cylindrical coordinate representations.
t, t'	Time and normalized time; note: $t' = \sigma_t c t$.
ω, ω', T	Angular frequency and the period of the beam pulse trains; note: $\omega = 2\pi / T$.
$\hat{s}, \hat{s}', \gamma$	Scatter and in-scatter directional unit vectors; γ is the angle between $\hat{s}$ and $\hat{s}'$. Note: $\hat{s} \cdot \hat{s}' = \cos\gamma = \cos\theta\cos\theta' + \sin\theta\sin\theta'\cos(\psi - \psi')$.
θ, θ', μ	The scatter and in-scatter angle measured positively from the positive direction of the z-axis; note: $\mu = \cos\theta$
ϕ, ϕ'	The scatter and in-scatter azimuthal angle measured on the xy-plane from the x-axis; see ψ.
ψ, ψ'	Scatter and in-scatter angle measured from the ρ-axis on the xy-plane; it is also a reduced variable as used in the radiative transfer equation, i.e., $\psi = \phi - \phi_x$ and $\psi' = \phi' - \phi_x$.
θ_M, ψ_M	Main beam direction or Pointing direction of the receiving antenna
θ_R, ψ_R	Direction of observation
$d\Omega, d\Omega'$	Differential scatter and in-scatter solid angle; note: $d\Omega = \sin\theta d\theta d\psi$.

TABLE OF DISCRETE VARIABLES
(Continued)

Variable	Definition
υ	The transformed variable for Fourier-cosine series of t'
k, k'	The transformed variable for Fourier-Hankel Transform of ρ, ρ'
m, l	The transformed integral variables for spherical harmonics of θ, ψ
u, u'	The transformed variable for Fourier-cosine transform of z, z'
N , $\bar{N}$	N is the last integer designated for m, l; it is used to determine the size of the problem. Note: N is an odd number, and $\bar{N}=N+1$ is the total number and is set to be divisible by four.
M	The total number in the series pertaining to the spherical harmonics (i.e., the total number of m, l); note: $M=(N+1)(N+2)/2=\bar{N}(\bar{N}+1)/2$.
N_b	The total number of usable eigensolutions obtained from the homogeneous solution; note: $N_b=(N+1)^2/4=\bar{N}^2/4, \bar{N}=N+1$
f_υ	Forcing function specified by the time-dependent Fourier-cosine series of the incident beam pulse trains
α_0	A Gaussian factor determining the basic characteristics of the incident beam pulse train
g_l	The coefficients for the spherical harmonics independent of ψ or, equivalently, the Fourier-Legendre series of the phase function
P_{RAD}	Radiated power transmitted and is set to 4π for convenience
S_{AVE}	Average Poynting vector of the incident beam wave
U_l^m	Normalized factor for the Associate Legendre polynomials in the spherical harmonics, determined from their orthogonal properties; note: $U_l^m=\sqrt{2(l+m)!/\left((2l+1)(l-m)!\right)}$.

TABLE OF DISCRETE VARIABLES
(Continued)

Variable	Definition
$C^m_{l,l'}$	Normalized forcing coefficients for the boundary condition, obtained from the half range associate orthogonal Legendre polynomial pairs
$\delta_m, \delta_{m0}, \delta_{m,l}$	Kronecker Delta function; note: $\delta_{m,l} = \begin{cases} 1, & m=l \\ 0, & m \neq l \end{cases}$, $\delta_m = \delta_{m0} = \delta_{m,0}$
ε_m	$\varepsilon_m = \begin{cases} 2, & m=0 \\ 1, & m=1,2,\ldots \\ 0, & m=-1 \end{cases} = \delta_m - \delta_{m,-1} + 1$
V^m	Normalized factor for the cosine factor in the spherical harmonics, determined from their orthogonal properties; note: $V^m = \sqrt{\pi \varepsilon_m}$.

CHAPTER 1

INTRODUCTION

For line-of-sight communication, cellular communication in particular, current interest centers on radio-link performance, and how it is affected by wave attenuation, fading and co-channel interference. When vegetation —such as a forest—lies along the path of a radio-link, strong multiscattering effects affect the radio performance.

There are two methods that are usually used to study multiscattering effects in random media, such as a forest—namely—analytical theory and transport theory. [1] Analytical theory is a very rigorous mathematical approach based on Maxwell's Equations. Since it is very complicated, strong simplifications are required to obtain any feasible solution, thus limiting its usefulness to restricted parameter ranges. In contrast, radiative transfer theory deals [1-5] with the transfer of energy through the multscattering medium and is developed heuristically from the conservation of energy principle in radiation space. The transport equation is equivalent to Boltzmann's equation found in the kinetic theory of gases and in neutron transport theory and is less rigorous than the analytic theory. However, the transport theory has been very successfully applied in the study of many radiation problems, such as optical propagation through the atmosphere, remote sensing and radiation from stars.

In previous work, continuous wave (CW) millimeter wave and plane wave pulse propagation in vegetation were studied by using the scalar transport theory [6-11]. In these

studies, interests focused on the determination of the range and the directional dependency of the received power as well as on the pulse broadening and distortion. The scalar transport equation is capable of specifying the total energy density of radiation in two orthogonal polarizations, but not polarization or depolarization effects; see [8] for experimental justification of their neglect in these studies for millimeter waves in vegetation. In the earlier developed theory for a plane wave incident upon the forest half-space, it was shown that the range dependency in the forest—treated as a random medium—is not simply an exponential decay at a constant attenuation rate. What actually occurs for the received power is a high attenuation rate at short distances into the medium that evolves into a much lower attenuation rate at large distances. The theory explains this in terms of the interaction between the coherent and incoherent field components. The coherent component—dominating at short distances—is highly attenuated by absorption and scattering while the incoherent component—generated by the scattering of the coherent component—does not lose power by further multiple scattering but scatters into itself, thus dominating at large distances into the forest, which in turn decreases at a greater reduced attenuation rate. In the transition region between the high and low attenuation regimes, significant beam broadening and pulse broadening occur.

Following these studies, the scalar time-dependent equation of radiative transfer was used to develop a theory for the propagation and scattering of narrowband, pulsed, collimated beam waves of finite cross-section in a medium, characterized by many random discrete scatterers (vegetation) that scatters energy strongly in the forward scattering direction. Applications include the scattering

of millimeter-waves in vegetation and the scattering of optical beams in the atmosphere. Strong forward scattering occurs at millimeter and optical frequencies since all of the scattered objects in the forest or in the atmosphere are large compared to the wavelength.

In this study, the scalar time-dependent equation of radiative transfer is used to develop a theory for the propagation and scattering of narrowband pulsed beam waves in a medium that is characterized by many random discrete scatterers (vegetation) which are assumed to scatter energy strongly in the forward scattering direction. Of interest are the range and directional dependency of received power, pulse broadening and distortion, and in addition the effect of a finite beam width when the incident field is not a plane wave.

CHAPTER 2

PROBLEM FORMULATION

2.1 Problem Setup

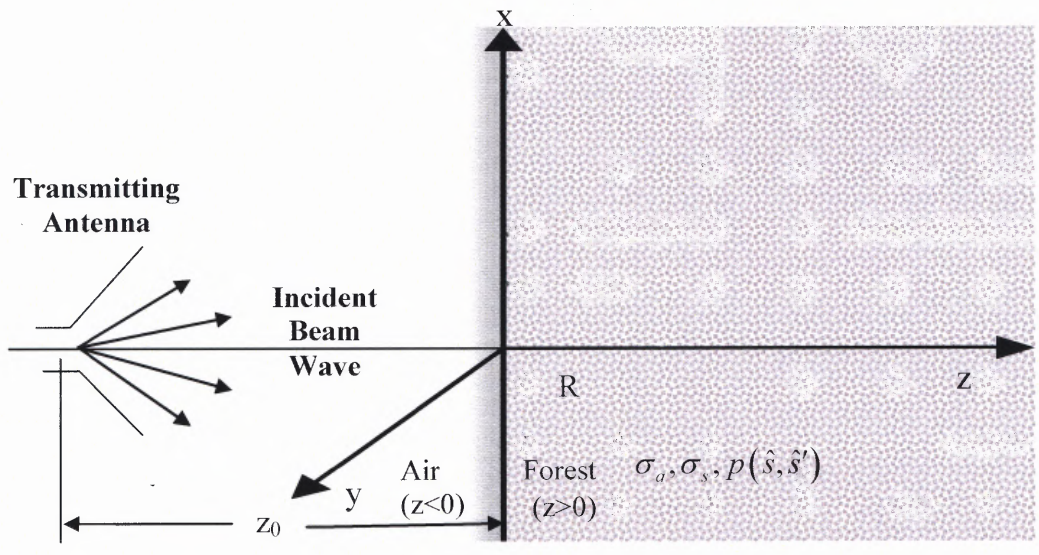

Figure 1 Beam wave pulse train incident onto a forest half-space

In this study, vegetation (a forest) is modeled as a statistically homogeneous half-space of randomly distributed particles that scatter and absorb electromagnetic energy as shown in Figure 1. A periodic sequence of pulses is taken to be incident from free-space onto the planar boundary of the forest. This incident pulse train is taken to be a diverging (spherical) beam wave (as opposed to the collimated (cylindrical) beam wave previously studied [11]). Such an incident pulsed beam wave constituents, for example, the radiation emitted by a transmitting microwave or millimeter wave antenna that is located in free-space outside a forest half-space. This situation is an important practical problem currently of interest to military and commercial applications.

2.2 Incident Divergent Beam Wave Pulse Train

Figure 1 illustrates the situation. The incident field traveling in the air region toward the boundary plane of the random medium takes the form of an idealized, diverging, periodically pulsed beam wave with a Gaussian time dependence. The magnitude of the instantaneous Poynting vector field of this beam wave in the R -direction is taken to be

$$S_R(\rho,z,t) = 2S_{AVE} f\left(t - R/c\right)\sin^2\left[\omega_c\left(t - R/c\right)\right]. \tag{1}$$

c is the wave velocity. S_{AVE} is time-average Poynting vector magnitude and is expressed

$$S_{AVE} = \frac{F(\theta_0)}{R^2} = \frac{P_{RAD} D(\theta_0)}{4\pi}, \tag{2}$$

where $F(\theta_0)$ is the radiation intensity pattern function, $D(\theta_0)$ is the directive gain, and P_{RAD} is the power radiated by the antenna. For $P_{RAD} = 4\pi$, then $F(\theta_0) = D(\theta_0)$.

The antenna pattern function is chosen to be given by

$$F(\theta_0) = \begin{cases} \dfrac{2(n+1)\cos^n(\theta_0)}{1-\cos\theta_{0M}^{n+1}}, & 0 \le \theta_0 \le \theta_{0M}, 0 \le \psi \le 2\pi \\ 0, & \text{elsewhere} \end{cases}, \tag{3}$$

where n is a positive integer and $F(\theta_0) \equiv F(\cos\theta_0)$ is normalized, such that

$$\iint_{4\pi} F(\cos\theta_0)\, d\Omega = 1. \tag{4}$$

For $n \gg 1$, the pattern function decreases to very small values near $\theta_0 = 0$.

$$F(\theta_0) \cong \begin{cases} 2(n+1)\cos^n(\theta_0), & 0 \le \theta_0 \le \theta_{0M}, 0 \le \psi \le 2\pi \\ 0, & \text{elsewhere} \end{cases}, \tag{5}$$

since $\cos^{n+1}\theta_{0M} \ll 1$. Numerical results in Chapter 4 are obtained for (5) to permit comparisons to the collimated beam case, which has been verified in comparison to a second solution method, the quadrature method in [11]. Hence, the comparison between the spherical beam case using (5) as presented here and the cylindrical case presented in [11] substantiates the theory to be presented below.

The function $f(t)$ in (1) determines the time dependence of the pulses (i.e. the pulse envelope). It is a positive and an even function of time t that is periodic with period T, i.e. $f(t + pT) = f(t)$, where p is an integer, and $f(t)$ is normalized, such that

$$\frac{1}{T}\int_{-T/2}^{T/2} f(t)dt = 1 \,. \tag{6}$$

For Gaussian incident beam pulses, $f(t)$ takes the form

$$f(t) = \frac{\alpha_0}{\sqrt{\pi}} e^{-(\alpha_0 t/T)^2} \quad , \quad -\frac{T}{2} \le t \le \frac{T}{2} \quad , \quad \alpha_0 \equiv \text{const} \,. \tag{7}$$

Since the function $f(t)$—defining the incident, beam wave pulses—is an even function, it can be represented by the real part of the Fourier series or the Fourier-cosine series:

$$f(t) = \sum_{\upsilon=0}^{\infty} f_\upsilon \cos(\upsilon\omega t) \,, \tag{8}$$

where

$$\omega = \frac{2\pi}{T} \quad , \quad f_\upsilon = \frac{\varepsilon_\nu}{T}\int_{-T/2}^{T/2} f(t)\cos(\upsilon\omega t)dt \,. \tag{9}$$

Hence, after substituting (7) into (9), the unknown coefficients are obtained as

$$f_\upsilon = \varepsilon_\upsilon e^{-(\pi\upsilon/\alpha_0)^2} \quad , \quad \varepsilon_\upsilon = \begin{cases} 1, & \upsilon = 0 \\ 2, & \upsilon \neq 0 \end{cases} . \tag{10}$$

α_o has to be chosen large enough to ensure that the Gaussian function in (7) approaches to zero as $t \to \pm T/2$, allowing the limits of the integration in (9) to be replaced by $\pm\infty$. Finally, the factor—$2\sin^2[\omega_c(t-R/c)]=1-\cos[2\omega_c(t-R/c)]$—in (1) characterizes the oscillations of the carrier within the pulse envelope; $\omega_c / 2\pi$ is the carrier frequency, which is assumed to be much bigger than the pulse repetition rate—$1/T$—so that numerous carrier oscillations can occur in one pulse.

In order to apply the transport theory, the incident beam needs to be characterized in terms of the specific intensity *I*, which is the basic quantity of the transport theory and is defined as the power per unit area and per unit solid angle being transmitted at a given point and in a given direction to the random medium. From (1) through (10), the specific intensity ofthe incident beam takes the form:

$$I_{inc} = S_{AVE} f\left(t - R/c\right)\left[\frac{\delta(\theta-\theta_0)\delta(\psi)}{\sin(\theta_0)}\right], z \le 0, \tag{11}$$

with

$$f(t-R/c) = \mathrm{Re}\left\{\sum_{\upsilon=0}^{\infty} f_\upsilon e^{i\upsilon\omega(t-R/c)}\right\}, \tag{12}$$

Where f_υ is given by (10) for the Gaussian pulses in (7). In (11), $\delta(\zeta)$ is the Dirac delta function, θ is defined as the scattering angle, which is measured positive from the positive z-axis direction (see Figure 2). The δ-function appears in (11) because the incident beam has a well-defined direction ($\theta = \theta_0$ and $\psi=0$) at any point in the air-region (z<0). In the forest region (z>0), the specific intensity has a continuous spectrum of directions which replaces the δ-function.

The carrier oscillations at the frequency $\omega_c / 2\pi >> 1/T$ at any given frequency, which in the air region are expressed by the term $2\sin^2[\omega_c(t-z/c)]$, tend to be obscured in the forest half-space due to the multiple scattering processes that take place in this random medium. Hence, in (11), this term has been replaced by unity, its average value. More precisely, individual multiscattering wave trains—crossing a given point (ρ,ϕ_x,z) in the random medium in a given direction (θ,ϕ) and at a given time *t*—tend to travel on many different paths, and their phases will be random, particularly because ω_c is so large that small changes in path length will result in significant differences in the phase. Thus, replacing $2\sin^2(\omega_c(t-z/c))$ in (11) by unity is well justified.

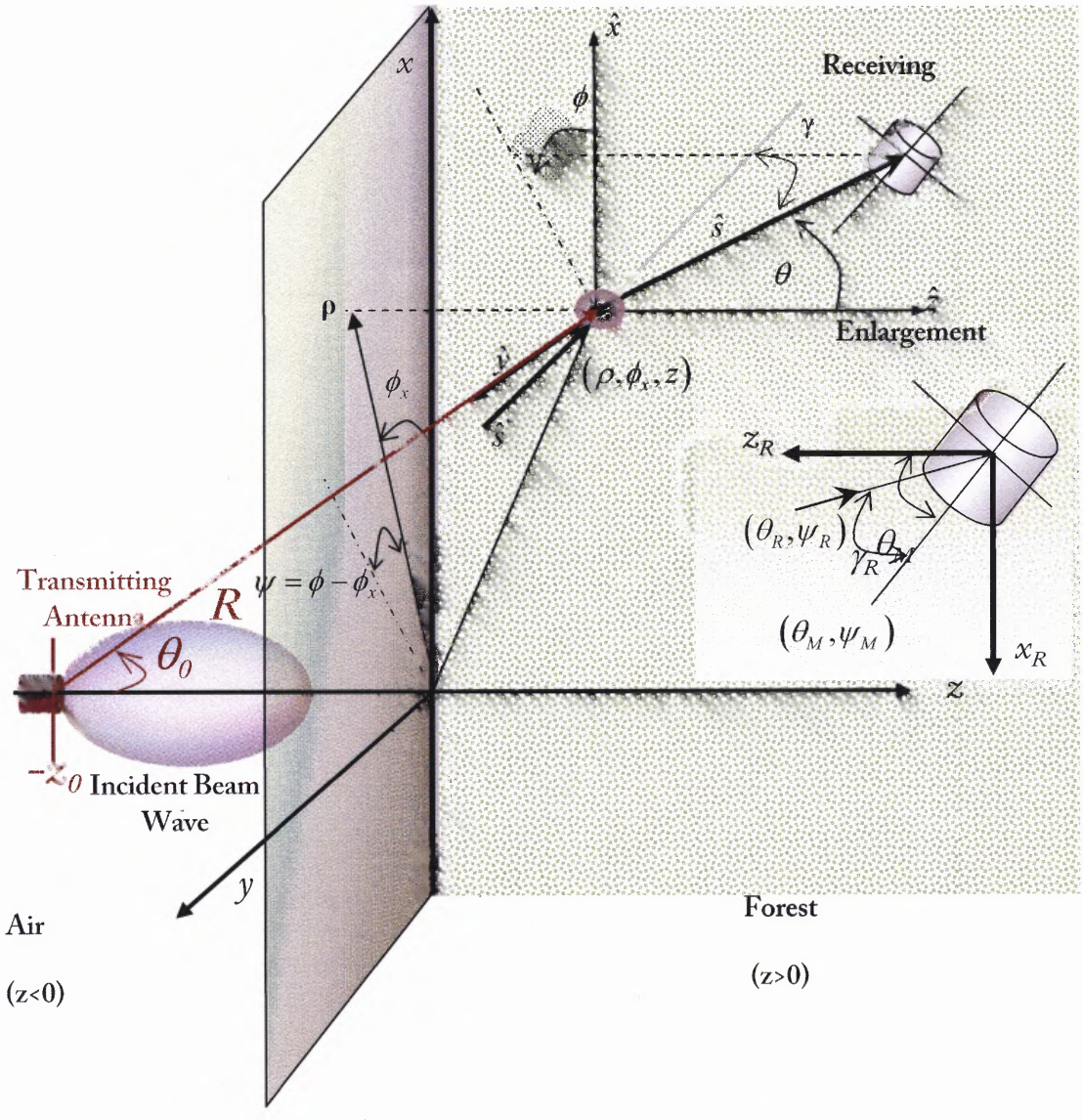

Figure 2 Basic geometry for scattering in the forest half-space of an incident beam wave pulse train. The "sphere" represents a scatter point in the forest. The tilted cylinder represents a receiving antenna, which is shown enlarged. The brown cylinder is the transmitting antenna, and the ellipsoid next to the brown cylinder is the incident beam wave.

2.3 Phase Function

In transport theory, the random scattering medium is characterized by an absorption cross-section per unit volume σ_a, a scattering cross-section per unit volume σ_s, and a power scatter or phase

function $p(\hat{s},\hat{s}')$. The phase function depends on both the incident power directional unit vector $\hat{s}'$ or, equivalently, the in-scatter angles (θ',ϕ') and the scatter power directional unit vector $\hat{s}$ or, equivalently, the out-scatter angles (θ,ϕ) for each scatter event (see Figure 2).

Since scattering surfaces in a forest essentially have random orientations, it is reasonable to assume that a forest scatters energy symmetrically about the direction of the incident radiation. Hence, the scattering, which occurs at each point in a forest, can be characterized by a phase function that depends only on the angle γ between $\hat{s}'$ and $\hat{s}$, where $\gamma=\cos^{-1}(\hat{s}'\cdot\hat{s})$; therefore, the phase function is expressed as

$$p(\hat{s},\hat{s}') = p(\hat{s}\cdot\hat{s}') = p(\gamma)\,. \tag{13}$$

In addition, since all the scattering objects in a forest are large compared to the wavelength at millimeter-wave and optical frequencies, the forest scatters energy strongly in the forward direction but weakly in all other directions. As such, the scattering function is assumed to be characterized by a strong narrow lobe, centered about γ=0 and superimposed over an isotropic background. This type of scattering function can analytically be expressed as a Gaussian function added to a homogeneous term:

$$p(\gamma)=\alpha q(\gamma)+(1-\alpha)\quad,\quad q(\gamma)=\left(\frac{2}{\Delta\gamma_s}\right)^2 e^{-\left(\gamma/\Delta\gamma_s\right)^2},\Delta\gamma_s<<\pi\,, \tag{14}$$

which is normalized such that

$$\iint_{4\pi} p(\gamma)d\Omega = 4\pi\,. \tag{15}$$

$d\Omega$ is the differential solid angle about the scatter angle $\hat{s}$, $\Delta\gamma_s$ denotes the width of the forward lobe in the scatter pattern and α is the ratio of the forward scattered power to the total scattered power. The scattering function (14) was justified in [6] by referencing to the comparison of results theoretically and experimentally in [7,8], and by the experiments conducted by Ulaby et al. in [12].

Therefore, by taking the scattering function as specified in (14) and assuming that random scatter medium is statistically homogeneous, the forest medium is then characterized by four spatially constant statistical parameters—namely—$\sigma_a, \sigma_s, \Delta\gamma_s$ and α. These four parameters are understood to be "global" parameters so that they remain valid at all points in the random medium, governing the average scatter and absorption event that may occur at any given point in this medium.

2.4 The Scalar Time-Dependent Transport Equation in Cylindrical Coordinates

In transport theory, the specific intensity I of the field in a random medium is governed by the radiative transfer equation, also known as the transport equation. In the normalized cylindrical coordinate system (ρ', ϕ_x, z') for symmetric scattering about the direction of the incident radiation, the scalar transport equation takes the form [5]:

$$\frac{\partial}{\partial t'} I(\vec{r}', t', \hat{s}) + \hat{s} \cdot \nabla' I(\vec{r}', t', \hat{s}) = -I(\vec{r}', t', \hat{s}) + \frac{W_o}{4\pi} \iint_{4\pi} p(\gamma) I(\vec{r}', t', \hat{s}') d\Omega', \tag{16}$$

where

$$\hat{s}\cdot\nabla' \equiv \cos\theta\frac{\partial}{\partial z'} + \sin\theta\cos\psi\frac{\partial}{\partial \rho'} - \frac{1}{\rho'}\sin\theta\sin\psi\frac{\partial}{\partial\psi} \tag{17}$$

$$\hat{s}\cdot\hat{s}' = \cos\gamma = \cos\theta\cos\theta' + \sin\theta\sin\theta'\cos\left(\psi-\psi'\right) \tag{18}$$

$$\vec{r}' = \hat{\rho}\rho' + \hat{z}z',\ \psi = \phi - \phi_x,\ d\Omega' = \sin\theta' d\theta' d\psi' \tag{19}$$

The normalized space and time variables in (16)-(19) are given by

$$\rho' = \sigma_t\rho,\ z' = \sigma_t z,\ t' = \sigma_t ct \tag{20}$$

and

$$W_0 = \frac{\sigma_s}{\sigma_t}, \text{and } \sigma_t = \sigma_a + \sigma_s. \tag{21}$$

The parameter W_0 is called the albedo and the parameters σ_a, σ_s and σ_t are the absorption, scatter and extinction cross-sections per unit volume, respectively. Implicit in writing (16) is the assumption that all parameters are independent of frequency. Figure 2 illustrates the five basic spatial coordinates ρ,ϕ_x,z ; θ,ϕ used in (16); ρ and z are shown here before normalization.

To obtain a unique solution to (16), the intensity I, assumed to be periodic with time, requires the satisfaction of the following two boundary conditions:

$$\begin{aligned} &I = I_{inc} \text{ at } && z' = 0,\ 0 \le \theta \le \pi/2 \\ &I \to 0 \text{ as } && z' \to \infty \end{aligned} \tag{22}$$

CHAPTER 3

RIGOROUS SOLUTION FOR DIVERGENT BEAM WAVE

3.1 Introduction

As is customary [1], the specific intensity is separated into two components, namely, the reduced incident intensity I_{ri} and the diffuse intensity I_d by letting

$$I = I_{ri} + I_d . \tag{23}$$

Substituting (23) into (16) and (22) yields the defining equations for I_{ri} and I_d, which take the forms

$$\frac{\partial}{\partial t'} I_{ri} + \hat{s} \cdot \nabla' I_{ri} + I_{ri} = 0, \tag{24}$$

$$\frac{\partial}{\partial t'} I_d + \hat{s} \cdot \nabla' I_d + I_d = \frac{W_o}{4\pi} \iint_{4\pi} p(\gamma) I_d d\Omega' + \frac{W_o}{4\pi} \iint_{4\pi} p(\gamma) I_{ri} d\Omega', \tag{25}$$

with boundary conditions

$$\begin{aligned} &I_{ri} = I_{inc},\ I_d = 0 \quad \text{at } z' = 0,\ 0 \le \theta \le \frac{\pi}{2}, \\ &I_{ri} \to 0,\ I_d \to 0 \quad \text{as } z' \to \infty \end{aligned} \tag{26}$$

where $\hat{s} \cdot \nabla'$ is defined in (17). Thus, the reduced incident intensity is defined in the random medium as the incident intensity attenuated by both scattering and absorption. The absorbed power is lost while the scattered power, represented by the last term in (25), serves as the forcing term, which builds up the diffuse intensity.

To solve for (24) through (26), Fourier series representations are introduced for the time dependence of the intensities:

$$I_j(\rho',z',t',\theta,\psi)=\mathrm{Re}\left\{\sum_{\upsilon=0}^{\infty} I_{j,\upsilon}(\rho',z',\theta,\psi)e^{i\upsilon\omega' t'}\right\} \quad j=inc,ri,d \tag{27}$$

where $T'=\sigma_t cT$, $\omega'=2\pi/T'$ and the normalized angular frequency $\omega'=\omega/(c\sigma_t)$. Observe also that although the specific intensity (power quantity) is always positive, the individual Fourier constituents $I_{j,\upsilon}$ may be negative and thus cannot physically represent power. The Fourier series (27) as used here is a purely mathematical procedure without any physical interpretation.

Substituting (27) into (24) yields for $z'>0$

$$i\upsilon\omega' I_{ri,\upsilon}+\hat{s}\cdot\nabla' I_{ri,\upsilon}+I_{ri,\upsilon}=0 \tag{28}$$

$$i\upsilon\omega' I_{d,\upsilon}+\hat{s}\cdot\nabla' I_{d,\upsilon}+I_{d,\upsilon}=\frac{W_o}{4\pi}\iint_{4\pi} p(\gamma)I_{d,\upsilon}\sin\theta' d\theta' d\psi'+\frac{W_o}{4\pi}\iint_{4\pi} p(\gamma)I_{ri,\upsilon}\sin\theta' d\theta' d\psi' \tag{29}$$

with the following boundary conditions:

$$\begin{array}{llll} I_{ri,\upsilon}=I_{inc,\upsilon} & , \quad I_{d,\upsilon}=0 & at \quad z'=0 & , \quad 0\le\theta\le\pi/2 \\ I_{ri,\upsilon}\to 0 & , \quad I_{d,\upsilon}\to 0 & as \quad z'\to\infty & \end{array} , \tag{30}$$

where $\upsilon=0,1,2,\cdots$.

A comparison of (11) with (12) expressed in normalized variables with (27) gives

$$I_{inc,\upsilon}=\sigma_t^2 f_\upsilon \frac{F(\cos\theta_0)}{R'^2} e^{i\upsilon\omega' R'} \frac{\delta(\theta-\theta_0)\delta(\psi)}{\sin\theta_0} \tag{31}$$

where $R'=\sigma_t R=(z'+z_0')/\cos\theta_0$, $z_0'=\sigma_t z_0$, and $F(\cos\theta_0)$ is the antenna radiation intensity pattern specified in (5), respectively. The reduced incident intensity at a point in the forest is the

incident intensity, exponentially attenuated over the distance from the forest boundary to the observation point. Hence, tracking the incident intensity from the antenna, a distance R' in direction θ_0 to the point in the forest permits the construction of I_{ri}, which satisfies (28) and the forest boundary condition of (30). It is given by

$$\tilde{I}_{ri,\upsilon} = \sum_{\upsilon=0}^{\infty} I_{ri,\upsilon} e^{i\upsilon\omega' t'} = \sigma_t^2 \sum_{\upsilon=0}^{\infty} f_\upsilon \frac{F(\cos(\theta_0))}{R'^2} e^{-z'/\cos\theta_0} e^{-i\upsilon\omega'(z'+z_0')/\cos\theta_0} \frac{\delta(\theta-\theta_0)\delta(\psi)}{\sin(\theta)}. \tag{32}$$

Substitution of the reduced incident intensity $I_{ri,\upsilon}$ from (32) into (29) and (30) gives, for $z'>0$,

$$\begin{aligned}[1+i\upsilon\omega']I_{d,\upsilon} + [\sin\theta\cos\psi\frac{\partial}{\partial\rho'} - \frac{1}{\rho'}\sin\theta\sin\psi\frac{\partial}{\partial\psi} + \cos\theta\frac{\partial}{\partial z'}]I_{d,\upsilon} \\ = \frac{W_o}{4\pi}\iint_{4\pi}[p(\gamma)I_{d,\upsilon}]\sin\theta' d\theta' d\psi' + \sigma_t^2 \frac{W_o}{4\pi} f_\upsilon p(\gamma_0) \frac{F(\cos\theta_0)}{R'^2} e^{-z'/\cos\theta_0} e^{-(z'+z_0')/\cos\theta_0}\end{aligned} \tag{33}$$

with boundary conditions

$$\begin{aligned} I_{d,\upsilon} &= 0 \quad at \quad z' = 0 \quad , \quad 0 \le \theta \le \frac{\pi}{2} \\ I_{d,\upsilon} &\to 0 \quad as \quad z' \to \infty \end{aligned} \tag{34}$$

where $\upsilon = 0,1,2,\cdots$ and $\gamma = \gamma_0$ for $\theta' = \theta_0$ in (17).

To solve (33), let $I_{d,\upsilon} = \sigma_t^2 \bar{I}_{d,\upsilon}$ be represented in terms of the Fourier–Hankel transform by

$$\bar{I}_{d,\upsilon}(\rho',z',\theta,\psi) = \sum_{m=0}^{\infty}\int_{k'=0}^{\infty} A_m^\upsilon(k',z',\theta)\left[J_m(k'\rho')\cos(m\psi)\right]k'dk' \tag{35}$$

with inverse transform

$$A_m^\upsilon(k',z',\theta) = \int_{\psi=0}^{2\pi}\int_{\rho=0}^{\infty} \bar{I}_{d,\upsilon}(\rho',z',\theta,\psi)\left[J_m(k'\rho')\cos(m\psi)\right]\rho' d\rho' d\psi\,. \tag{36}$$

The representation in (35) for $I_{d,\upsilon}$ is an expansion in terms of the basis functions $\cos(m\psi)J_m(k'\rho')$, which are complete and obey well-known orthogonality properties. The θ-dependent coefficients $A_m^{\upsilon}(k',z',\theta)$ are further expanded in terms of Associate Legendre functions

$$A_m^{\upsilon}(k';z',\theta)=\sum_{l=m}^{\infty}(2l+1)\bar{A}_{m,l}^{\upsilon}(k';z')P_l^m(\cos\theta) \tag{37}$$

so that (35) becomes

$$\bar{I}_{d,\upsilon}(\rho',z',\theta,\psi)=\sum_{m=0}^{\infty}\int_{k'=0}^{\infty}\sum_{l=m}^{\infty}(2l+1)\bar{A}_{m,l}^{\upsilon}(k',z')P_l^m(\cos\theta)J_m(k'\rho')\cos(m\psi)k'dk'. \tag{38}$$

Since scattering is assumed to be symmetric about the direction of the incident wave, the phase function is a function of γ only (see (13), (14), and (18)) and is conveniently represented as a series of Legendre polynomials P_l [1]:

$$p(\gamma)=\sum_{l=0}^{\infty}(2l+1)g_lP_l(\cos\gamma). \tag{39}$$

The Legendre polynomials are then expressed in terms of Associated Legendre functions via the expansion [1]

$$\begin{aligned}P_l(\cos\gamma)&=P_l(\mu)P_l(\mu')+2\sum_{n=1}^{l}\frac{(l-n)!}{(l+n)!}P_l^n(\mu)P_l^n(\mu')\cos(n(\psi-\psi'))\\&=\sum_{n=0}^{l}\frac{2(l-n)!}{\varepsilon_n(l+n)!}P_l^n(\mu)P_l^n(\mu')\cos(n(\psi-\psi'))\end{aligned} \tag{40}$$

with

$$\mu=\cos\theta \qquad \text{and} \qquad \varepsilon_n=\begin{cases}2, & n=0\\1, & n=1,2,\ldots\\0, & n=-1\end{cases} \tag{41}$$

to give

$$p(\gamma)=\sum_{l=0}^{\infty}\sum_{n=0}^{l}(2l+1)\frac{2(l-n)!}{\varepsilon_n(l+n)!}g_l P_l^n(\mu)P_l^n(\mu')\cos n(\psi-\psi'). \tag{42}$$

For the scattering function (14),

$$g_l=\frac{2\alpha}{\Delta\gamma_s^2}\int_{\gamma=0}^{\pi}e^{-(\gamma/\Delta\gamma_s)^2}P_l(\cos\gamma)\sin\gamma d\gamma+(1-\alpha)\delta_{0l}\ ,\quad \delta_{0l}=\begin{cases}1, & for\ l=0\\ 0, & for\ l\neq 0\end{cases} \tag{43}$$

Substituting (38), (42) and (43) into (33), using orthogonal properties, recursion relations and various identities of the functions $J_m(k'\rho')$, $\cos(m\psi)$ and $P_l^m(\cos\theta)$, and truncating at ($m=N$, $l=N$) yield the following inhomogeneous system of linear first-order differential equations for the expansion coefficients $\bar{A}_{m,l}^{\upsilon}(k',z')$ of $\bar{I}_{d,\upsilon}$:

$$\begin{aligned}&(l-m)\left[\frac{\partial}{\partial z'}\bar{A}_{m,l-1}^{\upsilon}\right]+(l+m+1)\left[\frac{\partial}{\partial z'}\bar{A}_{m,l+1}^{\upsilon}\right]+(2l+1)\left[1-W_0 g_l+i\upsilon\omega'\right]\bar{A}_{m,l}^{\upsilon}\\&+\frac{k'}{2}\left[(l-m-1)(l-m)\bar{A}_{m+1,l-1}^{\upsilon}-(l+m+1)(l+m+2)\bar{A}_{m+1,l+1}^{\upsilon}\right]+\frac{k'}{2}\varepsilon_{m-1}\left[\bar{A}_{m-1,l-1}^{\upsilon}-\bar{A}_{m-1,l+1}^{\upsilon}\right]\\&=\frac{(2l+1)}{\varepsilon_m}\frac{(l-m)!}{(l+m)!}\frac{W_0}{2\pi}g_l g_{m,l}^{\upsilon}(k',z')\end{aligned}$$

for $m=0,\ 1,\ 2,\ \cdots,N$ $\qquad l=m,\ m+1,\ \cdots,$ $\qquad 0\le k'<\infty$ (44)

with

$$g_{m,l}^{\upsilon}(k',z')=f_{\upsilon}\int_{\rho'=0}^{\infty}\frac{F(\cos(\theta_0))}{R'^2}e^{-\frac{z'}{\cos(\theta_0)}}P_l^m(\cos\theta_0)J_m(k'\rho')e^{-i\upsilon\omega'\left(\frac{z'+z_0'}{\cos\theta_0}\right)}\rho' d\rho', \tag{45}$$

The normalization is introduced as follows:

$$\bar{A}_{m,l}^{\upsilon}(k',z')=b_{m,l}^{\upsilon}(k',z')\frac{1}{U_l^m V^m}, \tag{46}$$

where

$$U_l^m = \sqrt{\frac{2}{2l+1}\frac{(l+m)!}{(l-m)!}} \qquad V^m = \sqrt{\pi\varepsilon_m}\,. \tag{47}$$

This allows (38) to be rewritten as

$$\bar{I}_{d,\upsilon}(\rho',z',\theta,\psi) = \sum_{m=0}^{\infty}\int_{k'=0}^{\infty}\sum_{l=m}^{\infty}(2l+1)b_{m,l}^{\upsilon}(k',z')\frac{P_l^m(\cos\theta)}{U_l^m}\frac{\cos(m\psi)}{V^m}J_m(k'\rho')k'dk', \tag{48}$$

and (44) to become

$$\alpha_1\left[\frac{\partial}{\partial z'}b_{m,l-1}^{\upsilon}\right]+\alpha_2\left[\frac{\partial}{\partial z'}b_{m,l+1}^{\upsilon}\right]+\alpha_3\left[1-W_0g_l+i\upsilon\omega'\right]b_{m,l}^{\upsilon}+\frac{k'}{2}\sqrt{\varepsilon_m}\left[\alpha_4 b_{m+1,l-1}^{\upsilon}-\alpha_5 b_{m+1,l+1}^{\upsilon}\right] \tag{49}$$

$$+\frac{k'}{2}\sqrt{\varepsilon_{m-1}}\left[\alpha_6 b^{\nu}{}_{m-1,l-1}-\alpha_7 b_{m-1,l+1}^{\upsilon}\right]=\sqrt{2l+1}\frac{g_l\bar{g}_{m,l}^{\upsilon}}{V^m}(k',z')W_0$$

$$m=0,\ 1,\ 2,\ \cdots,N;\quad l=m,\ m+1,\ \cdots,N;\quad 0\le k',z'<\infty$$

with

$$\alpha_1 \equiv \sqrt{(l-m)(l+m)(2l-1)} \qquad \alpha_2 \equiv \sqrt{(l-m+1)(l+m+1)(2l+3)} \qquad \alpha_3 \equiv \sqrt{(2l+1)^3}$$
$$\alpha_4 \equiv \sqrt{(l-m-1)(l-m)(2l-1)} \qquad \alpha_5 \equiv \sqrt{(l+m+1)(l+m+2)(2l+3)}$$
$$\alpha_6 \equiv \sqrt{(l+m)(l+m-1)(2l-1)} \qquad \alpha_7 \equiv \sqrt{(l-m+2)(l-m+1)(2l+3)}$$

and $$\bar{g}_{m,l}^{\upsilon}(k',z') = \frac{g_{m,l}^{\upsilon}(k',z')}{U_l^m} = f_{\upsilon}\int_{\rho'=0}^{\infty}\frac{F(\cos\theta_0)}{R'^2}e^{-\frac{z'}{\cos\theta_0}}\frac{P_l^m(\cos\theta_0)}{U_l^m}J_m(k'\rho')e^{-i\upsilon\omega'\left(\frac{z'+z_0'}{\cos\theta_0}\right)}\rho'd\rho'. \tag{50}$$

3.2 Homogeneous Solution

Solving (49) requires the determination of both homogeneous and particular solutions. To find the homogeneous solution, the right hand side of (49) is set to zero, and the homogeneous solution is assumed to be of the form

$$b_{m,l}^{\upsilon,h}(k',z') = G_{m,l}^{\upsilon}(k')e^{-z'/\sigma(k')}. \tag{51}$$

Substitution of (51) into (49) with the right hand side set to zero yields the homogeneous system of linear equations

$$\alpha_1 G^{\upsilon}_{m,l-1} + \alpha_2 G^{\upsilon}_{m,l+1} = \sigma \Bigg\{ b_{\upsilon l}\left[\alpha_3 G^{\upsilon}_{m,l}\right] + \frac{k'}{2}\sqrt{\varepsilon_m}\left[\alpha_4 G^{\upsilon}_{m+1,l-1} - \alpha_5 G^{\upsilon}_{m+1,l+1}\right] + \frac{k'}{2}\sqrt{\varepsilon_{m-1}}\left[\alpha_6 G^{\upsilon}_{m-1,l-1} - \alpha_7 G^{\upsilon}_{m-1,l+1}\right] \Bigg\} \tag{52}$$

$$\text{for } m = 0,\ 1,\ 2,\ \cdots, N \qquad l = m,\ m+1,\ \cdots, N \qquad 0 \le k' < \infty,$$

where $b_{\upsilon l} = 1 - W_0 g_l + i\upsilon\omega'$; ε_m is given by (41) and α_n by (50), respectively. Writing (52) in matrix form gives the generalized eigenvalue equation

$$\left[\mathbf{A}_0\right]\mathbf{G} = \sigma\left[\mathbf{C}_0\right]\mathbf{G} \tag{53}$$

where $\left[\mathbf{A}_0\right]$ and $\left[\mathbf{C}_0\right]$ are matrices. The eigenvalues (σ) and eigenvectors ($\mathbf{G}$) are determined by using the ZGGEVX based on the QZ method algorithm in the LAPACK library. N is chosen to be odd due to the boundary condition, making the combined matrix $\left[\mathbf{A}_0\right] - \sigma\left[\mathbf{C}_0\right]$ to be of size $M \times M$, where $M = 0.5(N+1)(N+2)$ as seen from (52). It can be shown that the number of eigensolutions is $N_b = (N+1)^2/2 < M$, as the eigenvalues σ appear—somewhat in a complicated fashion—on the subdiagonal and the superdiagonal rather than the diagonal of the combined matrix. Moreover, the boundary condition (30)—requiring that $\tilde{I}_{d,\upsilon} \to 0$ for $z' \to \infty$—restricts the number of allowable solutions to those associated with eigenvalues satisfying $\mathrm{Re}(1/\sigma) > 0$. As such, only half of the eigensolutions conform with this requirement and the number of these allowable solutions is $N_b = [(N+1)/2]^2$, hence justifying why N is chosen to be odd.

The matrices $[\mathbf{A}_0]$ and $[\mathbf{C}_0]$ are sparse and their coefficients are given by simple algebraic expressions. Thus, even though the number of eigenfunctions to be determined for each pair of k' and υ values of interest is in the order of several hundred, the numerical effort remains within reasonable limits.

3.3 Particular Solution

To obtain the particular solution to the inhomogeneous system of equations (49), the forcing term $\bar{g}^{\upsilon}_{m,l}(k',z')$ is restructured. Note that $\bar{g}^{\upsilon}_{m,l}(k',z')$ is defined (and used) for the region $0 \le z' < \infty$ only. In the region $-\infty < z' \le 0$, $\bar{g}^{\upsilon}_{m,l}(k',z')$ can be defined arbitrarily; in the solution to the problem under discussion, $\bar{g}^{\upsilon}_{m,l}(k',z')$ in the region $z' \le 0$ is not used. Hence, it is defined here, for convenience, to be an even function of z', i.e. to satisfy the condition

$$\bar{g}^{\upsilon}_{m,l}(k',z') = \bar{g}^{\upsilon}_{m,l}(k',-z'). \tag{54}$$

Thus, it is postulated that $\bar{g}^{\upsilon}_{m,l}(k',z')$ is represented in terms of its Fourier cosine transform:

$$\bar{g}^{\upsilon}_{m,l}(k',z') = \int_0^{\infty} \tilde{G}^{\upsilon}_{m,l}(k',u')\cos(u'z')\,du', \tag{55}$$

$$= \frac{1}{2}\int_{-\infty}^{\infty} \tilde{G}^{\upsilon}_{m,l}(k',u')e^{iu'z'}\,du' \tag{56}$$

where

$$\begin{aligned} \tilde{G}^{\upsilon}_{m,l}(k',u') &= \tilde{G}^{\upsilon}_{m,l}(k',-u') \\ &= \frac{2}{\pi}\int_0^{\infty} \bar{g}^{\upsilon}_{m,l}\cos u'z'dz'. \end{aligned} \tag{57}$$

Viewing the forcing term (56) as a superposition of differential forcing terms

$$d\bar{g}^{\upsilon}_{m,l}(k',z') = \frac{1}{2}\bar{G}^{\upsilon}_{m,l}(k',u')e^{iu'z'}du', \tag{58}$$

the particular solution to (52) for the differential forcing (58) is assumed to have the same exponential z' – dependency, namely,

$$db^{\upsilon}_{m,l}(k',z') = F^{\upsilon}_{m,l}(k',u')e^{iu'z'}du', \tag{59}$$

$$\frac{d}{dz}\left(db^{\upsilon}_{m,l}\right) = iu'F^{\upsilon}_{m,l}(k',u')e^{iu'z'}du' \tag{60}$$

Hence, (49) reduces to the linear system of equations:

$$\begin{aligned}
&-iu'\left[\alpha_1 F^{\upsilon}_{m,l-1} + \alpha_2 F^{\upsilon}_{m,l+1}\right] + \alpha_3 b_{\upsilon l} F^{\upsilon}_{m,l} \\
&+\frac{k'}{2}\sqrt{\varepsilon_m}\left[\alpha_4 F^{\upsilon}_{m+1,l-1} - \alpha_5 F^{\upsilon}_{m+1,l+1}\right] + \frac{k'}{2}\sqrt{\varepsilon_{m-1}}\left[\alpha_6 F^{\upsilon}_{m-1,l-1} - \alpha_7 F^{\upsilon}_{m-1,l+1}\right] \\
&= \frac{\sqrt{2l+1}}{2} g_l \tilde{G}^{\upsilon}_{m,l}(k',u')
\end{aligned} \tag{61}$$

$$\text{for} \quad m = 0,1,\ldots,N \quad \text{and} \quad l = m, m+1,\ldots,N,$$

where $\tilde{G}^{\upsilon}_{m,l}(k',u')$ is given by (57) with $\bar{g}^{\upsilon}_{m,l}(k',z')$ given by (50) so that

$$\begin{aligned}
\tilde{G}^{\upsilon}_{m,l}(k',u') &= \frac{2}{\pi}\int_0^{\infty} \bar{g}^{\upsilon}_{m,l}(k',z')\cos uz'dz' \\
&= \frac{2}{\pi} f_{\upsilon} \int_{z'=0}^{\infty}\int_{\rho'=0}^{\infty} \frac{F(\cos\theta_0)}{R'^2}\frac{P_l^m(\cos\theta_0)}{U_l^m} J_m(k'\rho') e^{-z'/\cos\theta_0} e^{-i\upsilon\omega'(z'+z'_0)/\cos\theta_0} \cos(u'z')\rho' d\rho' dz'
\end{aligned} \tag{62}$$

For convenience, the integration over ρ' in (62) is changed to an integration over μ_0 by introducing the change of variables

$$\begin{aligned}
&\mu_0 = \cos\theta_0, \quad \sin\theta_0 = \sqrt{1-\mu_0^2}, \quad \tan\theta_0 = \frac{\sqrt{1-\mu_0^2}}{\mu_0} \\
&R' = \frac{z'+z_0'}{\cos\theta_0} = \frac{z'+z_0'}{\mu_0} \\
&\rho' = (z'+z_0')\tan\theta_0 = (z'+z_0')\sqrt{1-\mu_0^2}\Big/\mu_0 \\
&d\rho' = (z'+z_0')\sec^2\theta_0 d\theta_0 = \frac{z'+z_0'}{\cos^2\theta_0}\cdot\frac{-d\mu_0}{\sin\theta_0} = \frac{-(z'+z_0')d\mu_0}{\mu_0^2\sqrt{1-\mu_0^2}} \\
&d\mu_0 = -\sin\theta_0 d\theta_0
\end{aligned}, \tag{63}$$

which yield

$$\bar{G}^{\upsilon}_{m,l}(k',u') = \frac{2}{\pi} f_{\upsilon} \int_{\mu_0=\mu_{0M}}^{1} \frac{F(\mu_0)P_l^m(\mu_0)}{\mu_0 U_l^m} \int_{z'=0}^{z'_{\max}} J_m\left[k'(z'+z_0')\frac{\sqrt{1-\mu_0^2}}{\mu_0}\right] \cdot e^{-z'/\mu_0} e^{-i\upsilon\omega'(z'+z_0')/\mu_0} \cos(u'z')\, d\mu_0 dz' \tag{64}$$

In the numerical evaluation of (64), the limit on the integral over z' is truncated at $z' = z'_{\max}$ to provide sufficient numerical accuracy. The integral over μ_0 ranges from $\mu_0 = \mu_{0M}$ to 1 for $n \gg 1$.

In matrix form, (61) is rewritten as

$$[\mathbf{B}_0]\mathbf{F} = \mathbf{g} \tag{65}$$

where $[\mathbf{B}_0]$ is a matrix while $\mathbf{F}$ and $\mathbf{g}$ are column vectors. The ZGESVX routine from the LAPACK library is used to find the particular solution [13].

The general solution to (49) is the superposition of the particular solution and $N_h = (N+1)^2/4$ allowable homogeneous solutions that obey the condition $\mathrm{Re}\{1/\sigma\} > 0$, which ensure that solutions decay as $z' \to \infty$. Thus, the general solution is obtained as

$$b^{\upsilon}_{m,l}(k',z') = b^{\upsilon p}_{m,l}(k',z') + \sum_{j=1}^{N_h} a_j b^{\upsilon,j}_{m,l}(k',z') = \int_{u'=-\infty}^{\infty} F^{\upsilon}_{m,l}(k',u') e^{iu'z'} du' + \sum_{j=1}^{N_h} a_j G^{\upsilon,j}_{m,l}(k') e^{-z'/\sigma_j} \tag{66}$$

where a_j, $j = 1,...,N_b$, are arbitrary constants that are determined from the boundary condition at $z' = 0$.

Using (66) in (38) and incorporating the truncations, the diffuse intensity is expressed as

$$I_{d,\upsilon}(\rho',z',\theta,\psi) = \sum_{m=0}^{N} \int_{k'=0}^{k'_{\max}} f_\upsilon \sum_{l=m}^{N} \left\{ (2l+1)[b_{m,l}^{\upsilon,p}(k',z') + \sum_{j=1}^{N_b} a_j G_{m,l}^{\upsilon,j}(k') e^{-z'/\sigma_j} \frac{P_l^m(\cos\theta)}{U_l^m} \right\} \cdot J_m(k'\rho') k' dk' \frac{\cos(m\psi)}{V^m} \tag{67}$$

where

$$b_{m,l}^{\upsilon,p}(k',z') = \int_{-\infty}^{\infty} F_{m,l}^{\upsilon}(k',u') e^{iu'z'} du' . \tag{68}$$

3.4 Boundary Condition at Entrance to Forest ($z' = 0$) to Find the Coefficients a_j

From (30), $I_{d,\upsilon}$ must satisfy the boundary condition, such that

$$I_{d,\upsilon}(\rho', z' = 0, \theta, \psi) = 0 \quad \text{for} \quad z' = 0, \ 0 \le \theta \le \pi/2, \quad 0 \le \rho' < \infty, \quad 0 \le \psi \le 2\pi . \tag{69}$$

(67) shows that $I_{d,\upsilon}$ is an even function of ψ and that its dependence on the coordinates ρ' and ψ is given by the functions $J_m(k'\rho')\cos(m\psi)$. As already stated earlier, these functions form a complete orthogonal system into which any function of ρ' and ψ (that is even in ψ) can be expanded in a given plane z' =const. This includes the boundary plane $z' = 0$ of interest here. As a consequence, the boundary condition (69) reduces to the requirement that the coefficients of the functions $J_m(k'\rho')\cos(m\psi)$, as they appear in (67) under the integral over k' and the sum over m, must be zero individually for $z' = 0$. Thus,

$$\sum_{l=m}^{N}(2l+1)\left[b_{m,l}^{\upsilon,p}(k',z'=0)+\sum_{j=1}^{N_b}a_j G_{m,l}^{\upsilon,j}(k')\right]\frac{P_l^m(\cos\theta)}{U_l^m}=0$$

$$b_{m,l}^{\upsilon,p}(k',z'=0)=\int_{u'=-\infty}^{\infty}F_{m,l}^{\upsilon}(k',u')du' \qquad (70)$$

$$\text{for } 0\le\theta\le\pi/2,\ 0\le k'\le k'_{\max},\ m=0,1,2,...,N$$

The boundary condition (70) is satisfied and the unknown coefficients a_j of the homogeneous solutions are determined by using the normalized Associate Legendre functions $P_{l'}^m / U_{l'}^m$ as testing functions. Since (70) must be satisfied over the half-range $0\le\theta\le\pi/2$, only half of these polynomials are used, for which $l'=m+1,m+3,\ldots$. These "odd" polynomials $P_l^m(\cos\theta)$—i.e. those of order $l'-m=1,3,5,\ldots$—form a complete orthogonal system for the half-region $0\le\theta\le\pi/2$. The even Associate Legendre functions polynomials with $l'-m=0,2,4,\ldots$ may be used as an alternative set of testing functions. It can be shown that the number of equations obtained in this way equals to $N_b=[(N+1)/2]^2$ of the unknown coefficients a_j. These equations take the form

$$\sum_{l=m}^{N}(2l+1)[b_{m,l}^{\upsilon,p}(k',z'=0)+\sum_{j=1}^{N_b}a_j G_{m,l}^{\upsilon,j}(k')]C_{l,l'}^m=0 \qquad (71)$$

$$\text{for } l'-m=1,3,5,\ldots\ ;\ m=0,1,2,...,N$$

with

$$C_{l,l'}^{m} = \int_{\theta=0}^{\pi/2} \left[\frac{P_l^m(\cos\theta)}{U_l^m}\right]\left[\frac{P_{l'}^m(\cos\theta)}{U_{l'}^m}\right]\sin\theta d\theta$$
$$= \begin{cases} J_{l,l'}^{m} & \text{for } l'-l = odd \\ \frac{1}{2} & \text{for } l'-l = 0 \\ 0 & \text{for } l'-l = \text{even} \neq 0 \end{cases} \tag{72}$$

and

$$J_{l,l'}^{m} = \frac{1}{2}(-1)^{m+(l+l'+1)/2}\frac{\sqrt{(2l+1)(2l'+1)[(l'+1)^2 - m^2]}}{(l-l')(l+l'+1)} \cdot$$
$$\cdot R(l+m)R(l-m)R(l'+m+1)R(l'-m+1)$$

$$R(\chi) \equiv \frac{\sqrt{\chi!}}{2^{\chi/2}\left(\frac{\chi}{2}\right)!}, \quad \chi = \text{even} \tag{73}$$

The coefficients a_j are independent of l, l' but vary with k' and m, which implies that the system of equations (71) has to be solved separately for each pair of k' and m values of interest. The process—of course—has to be repeated for each value of υ.

3.5 Power Received by a Highly Directive Antenna in the Forest

A highly directive, lossless antenna of narrow-beam width and narrow-bandwidth is located inside the forest as was done in [11]. This receiving antenna is characterized by an effective aperture $A(\gamma_R)$, where γ_R is the angle included between the direction of observation (θ_R, ψ_R) and the pointing direction of the antenna axis, i.e., the main beam direction (θ_M, ψ_M); see Figure 2. Hence,

$$\cos\gamma_R = \cos\theta_R\cos\theta_M + \sin\theta_R\sin\theta_M\cos(\psi_R - \psi_M) \tag{74}$$

Since powers add the transport theory, the instantaneous power received by the antenna is the sum of the intensity contributions coming from all directions, multiplied by the effective aperture of the antenna, such that

$$P^R(\rho',z',t',\theta_M,\psi_M)=\mathrm{Re}\left\{\sum_{\upsilon=0}^{\infty}P_\upsilon^R(\rho',z',\theta_M,\psi_M)e^{i\upsilon\omega' t'}\right\} \tag{75}$$

where

$$P_\upsilon^R(\rho',z',\theta_M,\psi_M)=\iint_{4\pi}A_e(\gamma_R)I_\upsilon(\rho',z',\theta_R,\psi_R)\sin\theta_R d\theta_R d\psi_R \tag{76}$$

and

$$I_\upsilon = I_{d,\upsilon}+I_{ri,\upsilon}. \tag{77}$$

Note that $\theta=\theta_R$ and $\psi=\psi_R$.

For millimeter waves, the carrier frequency is very large, and—therefore—the relative bandwidth of the received signal is narrow. For such a small bandwidth, the effective aperture and the gain of the receiving antenna can be taken to be independent of frequency and are related by the general expression

$$A_e(\gamma_R)=\frac{\lambda_o^2}{4\pi}D_R(\gamma_R) \tag{78}$$

where λ_o is the free space wavelength and $D(\gamma_R)$ is the directive gain of the receiving antenna at the carrier frequency.

The directive gain is assumed to be Gaussian with a narrow beam width $\Delta\gamma_M$ and with no sidelobes given by

$$D_R(\gamma_R) = \left(\frac{2}{\Delta\gamma_M}\right)^2 e^{-(\gamma_R/\Delta\gamma_M)^2} \quad , \quad \Delta\gamma_M << \pi \, , \tag{79}$$

which is normalized such that

$$\iint_{4\pi} D_R(\gamma_R)\sin\theta_R d\theta_R d\psi_R = 4\pi \, . \tag{80}$$

Using (75) - (79), the received instantaneous power P^R in (75) is obtained as the sum of the diffuse power P_d^R and the reduced incident power P_{ri}^R. The received diffuse instantaneous power is obtained as

$$P_d^R(\rho',z',t',\theta_M,\psi_M) = \mathrm{Re}\left\{\sum_{\upsilon=0}^{\infty} P_{d,\upsilon}^R(z',\rho',\theta_M,\psi_M)e^{i\upsilon\omega' t'}\right\}, \tag{81}$$

where

$$P_{d,\upsilon}^R(\rho',z',\theta_M,\psi_M) = \iint_{4\pi} A_e(\gamma_R) I_{d,\upsilon}(\rho',z',\theta_R,\psi_R)\sin\theta_R d\theta_R d\psi_R = \lambda_o^2 I_{d,\upsilon}(\rho',z',\theta_M,\psi_M) \tag{82}$$

It is assumed here that the beam width $\Delta\gamma_M$ of the receiving antenna is much narrower than the beam width of $I_{d,\upsilon}$. Similarly, the received reduced incident instantaneous power is obtained as

$$P_{ri}^R(\rho',z',t',\theta_M,\psi_M) = \mathrm{Re}\left\{\sum_{\upsilon=0}^{\infty} P_{ri,\upsilon}^R(z',\rho',\theta_M,\psi_M)e^{i\upsilon\omega' t'}\right\}, \tag{83}$$

where

$$\begin{aligned} P_{ri,\upsilon}^R(\rho',z',\theta_M,\psi_M) &= \iint_{4\pi} A_e(\gamma_R) I_{ri,\upsilon}(\rho',z',\theta_R,\psi_R)\sin\theta_R d\theta_R d\psi_R \\ &= \frac{\lambda_o^2}{4\pi} D_R(\gamma_M) f_\upsilon \sigma_t \frac{F(\cos\theta_0)}{R'^2} e^{-\frac{z'}{\cos\theta_0}} e^{-i\upsilon\omega'(z'+z_0')/\cos\theta_0} \end{aligned} \, , \tag{84}$$

where

$$\cos\gamma_M = \cos\theta_0\cos\theta_M + \sin\theta_0\sin\theta_M\cos\psi_M \tag{85}$$

For convenience, the instantaneous received power is normalized to the received time-average power at $\rho' = 0$, $z' = 0$, $\theta_M = 0$ and $\psi_M = 0$, which—since $I_{d,\upsilon}$ is zero at $z' = 0$ and by using (6) and (7)—is given by

$$\left\langle P^R(0,0,t',0,0)\right\rangle \equiv \frac{1}{T'}\int_{-T'/2}^{T'/2} P^R(0,0,t',0,0)dt' = \frac{\sigma_t^2\lambda_o^2}{4\pi} D_R(0)\frac{2(n+1)}{z_0'^2}, \tag{86}$$

where $$\gamma_M = \theta_0 = 0°.$$

Thus, the normalized total instantaneous received power is the sum of the reduced incident and the diffuse normalized received powers, namely,

$$P'(\rho',z',t',\theta_M,\psi_M) = \frac{P^R(\rho',z',t',\theta_M,\psi_M)}{\left\langle P^R(0,0,t',0,0)\right\rangle} = P'_{ri} + P'_d. \tag{87}$$

Using (81)-(86), the total normalized instantaneous received power in (87) becomes

$$P'(\rho',z',t',\theta_M,\psi_M) = P'_{ri} + P'_d = \mathrm{Re}\left\{\sum_{\upsilon=0}^{\infty} P'_\upsilon(z',\rho',\theta_M,\psi_M)e^{i\upsilon\omega' t'}\right\} \tag{88}$$

where

$$\begin{aligned} P'_\upsilon(\rho',z',\theta_M,\psi_M) &= P'_{ri,\upsilon} + P'_{d,\upsilon} \\ &= \frac{z_0'^2 D_R(\gamma_M)F(\cos\theta_0)}{R'^2 D_R(0)(2n+2)} f_\upsilon e^{-z'/\cos\theta_0} e^{-i\upsilon\omega'(z'+z_0')/\cos\theta_0} \\ &+ \frac{4\pi z_0'^2}{\sigma_t^2 D_R(0)(2n+2)} I_{d,\upsilon}(\rho',z',\theta_M,\psi_M) \end{aligned} \tag{89}$$

Thus, (88) and (89)

$$\begin{aligned} P' &= P'_{ri,\upsilon} + P'_{d,\upsilon} \\ &= \frac{z_0'^2 D_R(\gamma_M)F(\cos\theta_0)}{R'^2 D_R(0)(2n+2)} e^{-z'/\cos\theta_0} f(t'-R') \\ &+ \frac{4\pi z_0'^2}{\sigma_t^2 D_R(0)(2n+2)} \mathrm{Re}\left\{\sum_{\upsilon=0}^{\infty} I_{d,\upsilon}(\rho',z',\theta_M,\psi_M)e^{i\upsilon\omega' t'}\right\} \end{aligned} \tag{90}$$

Observe that for z'=0 we have

$$P' = P'_{ri} = \frac{z_0'^2 D_R(\gamma_M) F(\cos\theta_0)}{R'^2 D_R(0)(2n+2)} f(t'-R') \tag{91}$$

which is in agreement with expectation. The diffuse power P'_d, on the other hand, is determined by $I_{d,\upsilon}$ and, thus, is zero in the boundary condition (34) in the boundary plane z' for all ρ' and ψ, and for $0 \le \theta_M \le \pi/2$.

The result (90) was expected since the reduced incident power P'_{ri} is the power of the incident beam wave pulse train that, as it travels through the forest along a straight path, decays exponentially due to absorption and scattering, but maintains its narrow beam width and its time dependence. No beam broadening or pulse broadening occurs. The θ-dependence of P'_{ri}, thus reproducing the radiation pattern of the receiving antenna. On the other hand, the diffuse intensity, generated by scattering of the reduced incident intensity and by self-regeneration due to multiscattering, is characterized by a broad beam width—which is larger than that of the receiving antenna. Hence, the receiving antenna acts to probe the angular distribution of the diffuse intensity $I_{d,\upsilon}$ as seen from (89). Multiscattering also causes pulse broadening. Due to the increasing length of their propagation paths, multiscattered wave trains arrive later and the pulses develop tails. In the numerical results, the summation in (90) is truncated at a value $\upsilon = \upsilon_{\max}$ that ensures convergence.

CHAPTER 4

NUMERICAL RESULTS

4.1 Background

A significant part of this research is the numerical simulation. The simulation for one set of parameters required running 160 processors continuously for eight days. The reason the numerical simulation takes such a long time is because the solution to the transport equation involves five variables, which requires implementation of multiple numerical integrations and several solutions to very large linear systems of equations (both dense and sparse matrices).

The three-dimensional scalar transport equation is an integro-differential equation for the specific intensity that, in general, depends on six independent variables—three positional variables (ρ',ϕ_x,z'), two scattering directional variables (θ,ϕ), and one temporal variable (t')—and several parameters $(W_0;\Delta\gamma_s;z_0,n)$. For the cylindrical symmetry case considered here, these six variables reduce to five independent variables, which include the rotational azymuthal angle $\psi=\phi-\phi_x$. Further development reduces the integro-differential equation of five variables in (16) to solving discretized linear equations in (52), (61), (71), which permit implementation of a numerical solution on the computer.

To obtain the discretized equations, use is made of the Fourier series to transform from t' to υ, the Spherical Harmonics to transform from (θ,ψ) to (m,l), the Fourier-Hankel

transform to transform from ρ' to k' (ranging from 0 to $k'_{\max}$), and the Fourier-cosine transform to transform from z' to u' (ranging from $-u'_{\max}$ to $u'_{\max}$). Consequently, it is necessary to determine the accuracy of the discretizations. To do so, a few test cases are conducted before running any lengthy simulations. In addition, the parameters of the simulations are chosen in such a way that they can be computed within a reasonable amount of time due to limited computational resources for this research. Next, methods of integration are chosen carefully to obtain numerical solutions for the phase function, for the Fourier-Hankel transform, for the forcing term of the particular solution, and for the inverse Fourier transform of the particular solution. The particular solution, the homogeneous solution, and the boundary condition at $z'=0$ are then computed for all chosen values of υ and k'. Subsequently, the diffuse intensity is calculated for different values of the dependent variables $(\rho', z'; \upsilon; \theta, \psi)$. Finally, the time-dependent received power is computed using the diffuse intensity over a range of time t' and the reduced incident power.

The solutions to the linear system of equations (61) for finding the particular solution and (71) for solving the boundary condition at $z'=0$ were obtained by using LU factorization, linear equation solver, and iterative refinement packages provided by the optimized LAPACK library. The eigenvalue solutions were obtained by using the ZGGEVX routine from the LAPACK library that is based on the QZ method in EISPACK [13]. When tested, both of these procedures gave absolute errors ranging from 10^{-10} to 10^{-16}. This accuracy is acceptable, as the library routines handle all variables using double precision, which means a precision that is accurate up to about

sixteen digits. The phase function, the pattern function for the incident divergent beam, and the satisfaction of the boundary condition at $z'=0$ will be discussed before showing any numerical results for the received power. Next, the graphs will be illustrated and discussed in this chapter, thereby concluding the theoretical development of the work.

4.2 Global Parameters

In the simulations, the following parameters are global in that are used in all of the simulations, as was done in [11]:

$$\begin{aligned} W_0 &= 0.75 \\ \alpha &= 0.8 \\ \alpha_0 &= 4\sqrt{5} \\ \Delta\gamma_s &= 0.3 \\ \Delta\gamma_M &= 0.012 \\ T' &= 2 \end{aligned} \tag{92}$$

In addition, in most cases unless specified otherwise, the following parameters are used:

$$\begin{aligned} z_0' &= 40 \\ N &= 31 \end{aligned} \tag{93}$$

Moreover, there are other parameters determined by trial and error to ensure that the system can be solved accurately within a reasonable amount of time. For example, $k'_{\max}$ is determined by observing how much the forcing function of the linear system of equations (61) is attenuated, allowing better selections of n and z_0', which determine the beam width of the incident beam and the distance between the transmitting antenna and the forest boundary, respectively. Meanwhile, the $u'_{\max}$ is determined through several test cases by taking the inverse Fourier transform of the Fourier-cosine

transform of the forcing function in the particular solution. This allows one to observe the range of u' needed for acceptable convergence for the given parameters. In all of these test cases, it is shown that 100 is sufficiently large for $u'_{\max}$. The following quantities vary among different simulations: $N, k_{\max}, \upsilon_{\max}, w', \rho', z', \theta, \psi$.

Truncation at $l_{\max} = N \geq 27$ of the series representation (39) for the phase function in terms of Legendre polynomials was shown in [11] to exhibit the required shape of a pronounced forward lobe superimposed on an isotropic background and to agree with the exact expression (14) for the phase function to within a relative accuracy of 10^{-6}.

The $k'_{\max}$ value that is required in the truncation of the Hankel transform in (38) is taken so that more than 99% of the integrand is included. The truncation at $\upsilon_{\max} \geq 12$ of the series representation (8) for the Gaussian incident pulses was found to yield values that are sufficiently close to the exact values determined from (7) as was done in [11].

4.3 Phase Function

Phase function (14) is a power scattering function that describes how electromagnetic energy is scattered and absorbed by objects in the random medium. The scatterers—which are the objects (such trees and leaves) in the random medium (the vegetation)—scatter energy strongly in the forward direction and weakly in the backward direction. Recall that the phase function is normalized in (15) such that

$$\iint_{4\pi} p(\gamma)d\Omega = 4\pi \tag{94}$$

This dictates that g_0 in (43) must equal unity. However, g_0 does not equal unity when determined numerically from (43), which gives $g_0 = 0.9881$ for $\Delta\gamma_s = 0.3, \alpha = 0.8$. To ensure that g_0 is unity, the phase function $p(\gamma)$ is redefined as $p_{norm}(\gamma) = p(\gamma)/g_0$, which guarantees that (94) is satisfied with $p(\gamma)$ replaced by $p_{norm}(\gamma)$. The three-dimensional rotationally symmetric phase (scatter) function given in (14) is plotted in Figure 3. As one can see, there is a tiny back lobe in the graph, which shows that the scattering is weak in the backward direction.

4.4 Pattern Function

The pattern function $F(\cos\theta_0)$ given in (5) represents the radiation intensity pattern of the transmitting antenna; it is plotted in Figure 4 and Figure 5 for integer powers $n=50$, 200, and 1000. Observe that the pattern becomes narrower as n increases.

Figure 4 shows the overlapping of the pattern function $F(\cos\theta_0)$ of the spherical incident beam having integer power $n=1000$ with the Gaussian amplitude function $A(\rho')$ for the cylindrical incident beam having beam width $w' = 1.79$; see [11]. This was expected because the half-power beam width of the $n = 1000$ spherical beam equals that of the cylindrical beam width having $w' = 1.79$. For these two incident beams, the powers received by antenna in the forest are identical. The numerical results for these cases provide verification of the theory presented here for

the spherical (diverging) incident beam because the results for the incident collimated beam have been validated by comparisons to alternative approaches in [11].

4.5 Forcing Function

The forcing function for the particular solution is written in (64) and is repeated as follows:

$$\bar{G}^{\upsilon}_{m,l}(k',u') = \frac{2}{\pi} f_{\upsilon} \int_{\mu_0=\mu_{0M}}^{1} \frac{F(\mu_0) P_l^m(\mu_0)}{\mu_0 U_l^m} \int_{z'=0}^{z'_{\max}} J_m\left[k'(z'+z'_0)\frac{\sqrt{1-\mu_0^2}}{\mu_0} \right] \cdot e^{-z'/\mu_0} e^{-i\upsilon\omega'(z'+z'_0)/\mu_0} \cos(u'z') dz' d\mu_0 \tag{64}$$

The factor $F(\mu_0)P_l^m(\mu_0)/\mu_0$ over μ_0 from μ_{0M} to 1 is not highly oscillatory. In (5), μ_{0M} is defined in the range $0<\theta_{0M}<\pi/2$ such that $\cos^{n+1}\theta_{0M} \ll 1$. The truncation value $z'_{\max}$ in the upper limit of the integral over z' is obtained from the exponential decay term in (64) because it is the most attenuated term in the integrand. Because the remaining portions of the integral over z' can be oscillatory, it is necessary to integrate over enough points within one spatial period in order to compute the integral accurately. To determine an estimate for this period, one adds the individual periods of each oscillatory term in (64), i.e. the periods for the Bessel function, the oscillating exponential term and the cosine term. The asymptotic form of the Bessel function term is used to obtain the period of the Bessel function as the worst-case scenario. Therefore, the spatial period is found to be given as

$$\underset{\sim}{p} = \left| k' \frac{\sqrt{1-\mu_0^2}}{\mu_0} \right| + |u'| - |\upsilon\omega'/\mu_0|,$$

where $$\underset{\cdot\cdot}{p}\Delta z' = 2\pi, \qquad z'_{max} = N_0 \Delta z', \qquad N_0 = 1,2,3,\ldots. \tag{95}$$

(95) is used to estimate how many points are needed for the z'-integration range.

4.6 Discussions

Computational results for diffuse intensity are presented for the time-independence case in Figure 6 to Figure 23. To be acceptable, these solutions must satisfy the boundary condition (34), which requires that the diffuse intensity $I_{d,\upsilon}$ be zero at $z'=0$ throughout the forward angular range $0 \le \theta \le \pi/2$. Observe that in Figure 6 the boundary condition (34) is very satisfied for the time-independent case ($\upsilon=0$) for different incident beams and improves as N increases (shown for convergence). Numerical inaccuracies produce the negligibly small, non-zero values for $I_{d,0}$ over the range $0 \le \theta \le 90°$. Although only the $\upsilon = 0$ case is illustrated in Figure 6, satisfaction of the boundary condition was also obtained for $\upsilon > 0$ for which values of $|I_{d,\upsilon}|$ were shown to be significantly smaller than $|I_{d,0}|$.

To validate the results determined for the spherical beam case, comparisons are made between the very narrow spherically divergent incident beam case ($n = 1000$) and the collimated incident beam case for which $w' = 1.79$. Note that results previously obtained for the incident collimated beam case were shown to reduce correctly to the incident plane wave case and to agree with results obtained by the Quadrature method [11]. As mentioned earlier, the particular incident collimated beam wave having $w' = 1.79$ possesses the same half-power beam width as the spherical

incident beam wave with $n=1000$ and to have identical beam patterns (see Figure 4 and Figure 5). Figure 7 shows that the two cases also yield almost identical results for the diffuse intensity over the full range $0\le\theta\le 180°$.

To enable comparison between results for the spherical and cylindrical beams, intensity $I_{d,\upsilon}$ is normalized by using the received time-average power P' given in (86) for the spherical beam and (39) in [11] for the cylindrical beam. Hence, in Figure 6 and Figure 7,

$$\underline{I}_{d,\upsilon}(\rho',z';\theta,\psi)=\frac{4\pi z_0^2}{2(n+1)}I_{d,\upsilon}(\rho',z';\theta,\psi). \tag{96}$$

is plotted for the spherical beam while $I_{d,\upsilon}$ given by (33) in [11] is plotted for the cylindrical beam.

Figure 7 (top) shows how different intensities for the cylindrical beam ($w'=1.79$) and the narrow spherical beams ($n=200$ and $n=1000$) behave as a function of penetration depth z' into the forest. This figure shows that close to the interface at $z'=0$, the diffuse intensity grows rapidly, reaches its peak for $z'=1-2$ and then falls (attenuates) more slowly as z' increases. Comparisons of Figure 7 (top) and Figure 7 (bottom) show that $I_{d,0}$ is strongest on the $z'-$axis (for $\rho'=0$) at its maximum value and has a smaller maximum value at off-axis points, which decrease as ρ' gets larger.

Figure 8 to Figure 10 characterize how $I_{d,0}$ varies with the penetration depth for $n=200$ and $n=1000$ at different off-axis locations ($\rho'>0$) in different scatter directions. Figure 8 shows that a smaller maxima occurs over at larger values of ρ' and the maxima all occur near the same penetration depth, but slightly to the right for smaller ρ'. Note that for the scatter direction

$\theta = 0°$: as ρ' increases, the maximum decreases; but for $\theta = 15°$, as ρ' increases, the maximum first increases then decreases. Figure 9 demonstrates that the maximum decreases as ρ' increases for $\theta = 0°$ and that the locations of these maxima shift slightly to the right as ρ' increases. However, for $\theta = 45°$ on the same graph, one can see that as ρ' increases, the maximum first increases then decreases and the locations of the maxima shift noticeably. In Figure 10, the location of the maximum of I_{d0} shift to the right as ρ' increases.

Figure 11 shows that the maximum decreases as θ increases from $0°$ to $75°$, that the peak shift to the right initially as θ increases but then after $\theta = 45°$ in the top figure the location of the maximum shifts to smaller z' values. In Figure 11 (bottom), the maxima shift to the left after $\theta = 30°$. Figure 12 shows the same behavior as in Figure 11, but the maxima shift to smaller values of $z' = z'_{max}$ (the penetration depth at which $I_{d,0}$ is maximum) as θ increases.

Figure 13 to Figure 15 display $I_{d,0}$ at different ρ' values in the backscatter direction. Figure 13 shows that over the backscatter direction for $\theta = 105°$ to $\theta = 180°$, the I_{d0} seems almost unchanged for $n = 1000$; note that data for $\theta = 180°$ is not reliable. Figure 13 to Figure 15 show the behavior of I_{d0} in the backscatter direction with $I_{d,0}$ largest in the $\theta = 105°$, but decreases to smaller values as θ increases towards $180°$.

Figure 16 to Figure 21 show plots of I_{d0} versus scatter direction θ. In these figures, beam broadening occurs as z' increases. In Figure 16, for $\rho' = 0$, all scattering is symmetric about the $z'-$axis. Note in Figure 18 that all scattering is symmetric about a tilt angle measured positive

from the positive $z'-$axis. In Figure 18, beam broadening occurs as z' increases for fixed ρ' whereas in Figure 19, beam broadening occurs as ρ' increases for fixed z'. In Figure 20, the beam is symmetric about the $z'-$axis ($\theta = 0°$) for $\rho' = 0$ but it is symmetric about θ=38° for $\rho' = 0.5$. Figure 21 shows similar behavior.

Figure 22 and Figure 24 shows the three-dimensional plots of I_{d0} in different scatter directions ($\theta = 0°, 30°, 60°, 120°, 150°, 180°$). In Figure 24 to Figure 28, the normalized received diffuse power P_d' versus normalized time t' for the spherical beam ($n = 1000$) and the cylindrical beam ($w' = 1.79$) are plotted. These figures show that the diffuse power are identical for $\theta = 0$ and $\rho' = 0$ at different z' locations. In plotting these cases, the time-delay between the spherical and cylindrical case is taken into consideration to synchronize the received signals. These curves verify the theory developed here for the spherical beam wave since these curves agree so well with the cylindrical beam case which has been independently verified in [11].

Figure 29 gives the normalized received reduced incident power versus normalized time for both the spherical beam ($n = 1000$) and the cylindrical beam ($w' = 1.79$) for different penetration depths z'. Here, no compensation is given for the time-delay between these two beams. In addition, the error in the diffuse power received at $z' = 0$ is shown to be very small. Figure 30 to Figure 35 show the total received power at different locations ρ' in the forward direction ($\theta_M = 0° \ \psi_M = 0°$) for different values of z'. One sees how energy progresses, attenuates and distorts the further it travels in the forest.

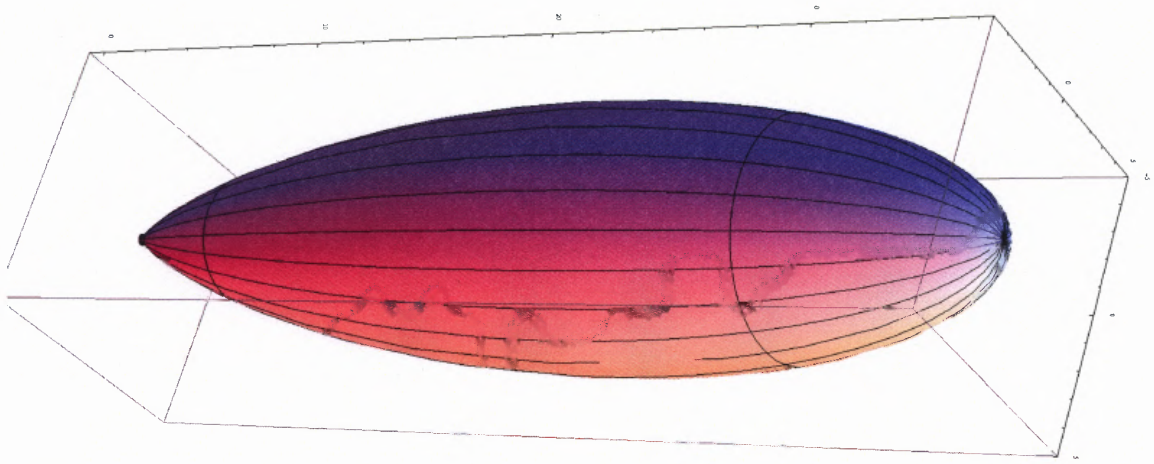

Figure 3 The plot of the phase function (power scattering function) for strong forward scattering by the discrete scatterers in the random medium: notice that there is a small back-lobe at the far left, thus indicating that the energy scatters weakly in the backward direction but strongly in the forward direction.

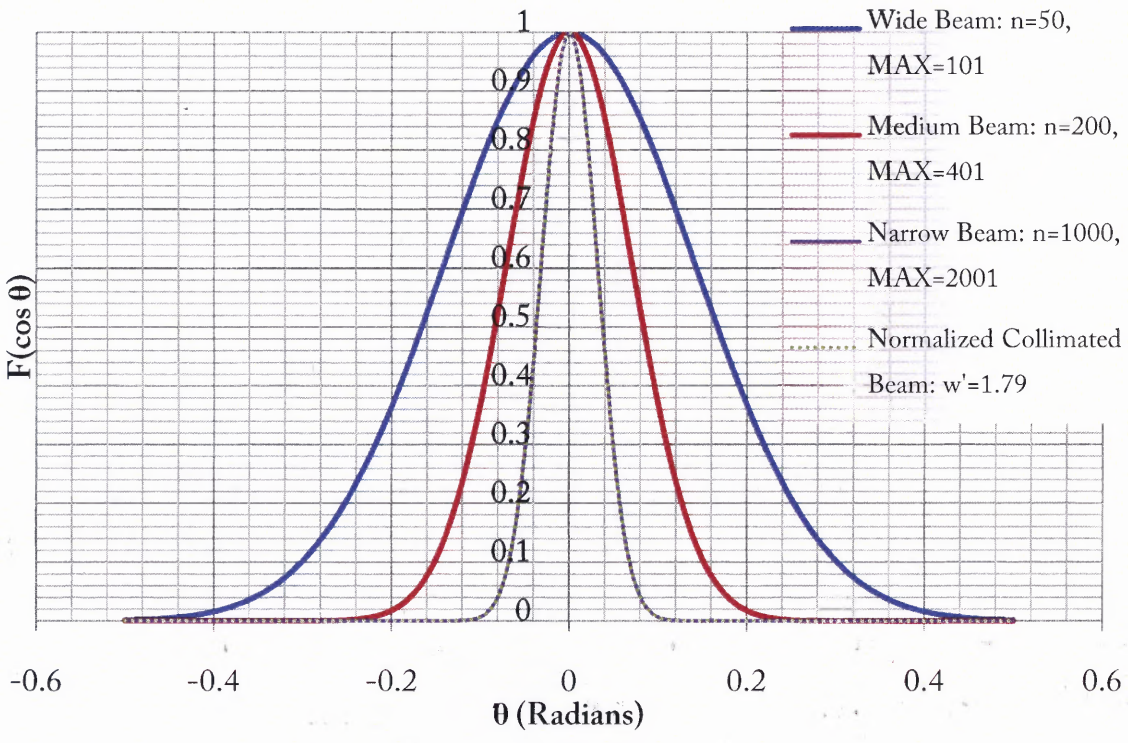

Figure 4 Plot of the incident divergent beam's pattern functions $F(\cos\theta_0)$ for different values of positive integral powers n.

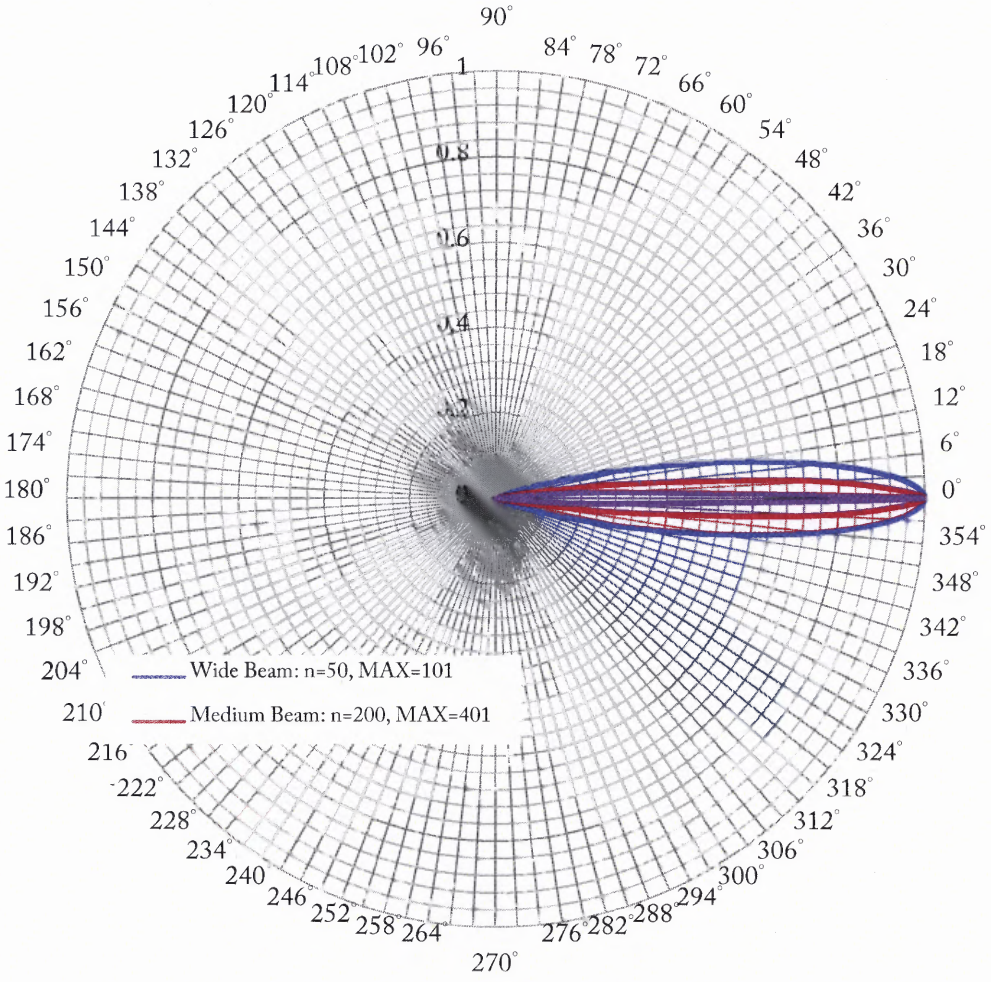

Figure 5 Plot of the incident divergent beam's pattern functions $F(\cos\theta_0)$ for different values of integer power n in polar coordinates.

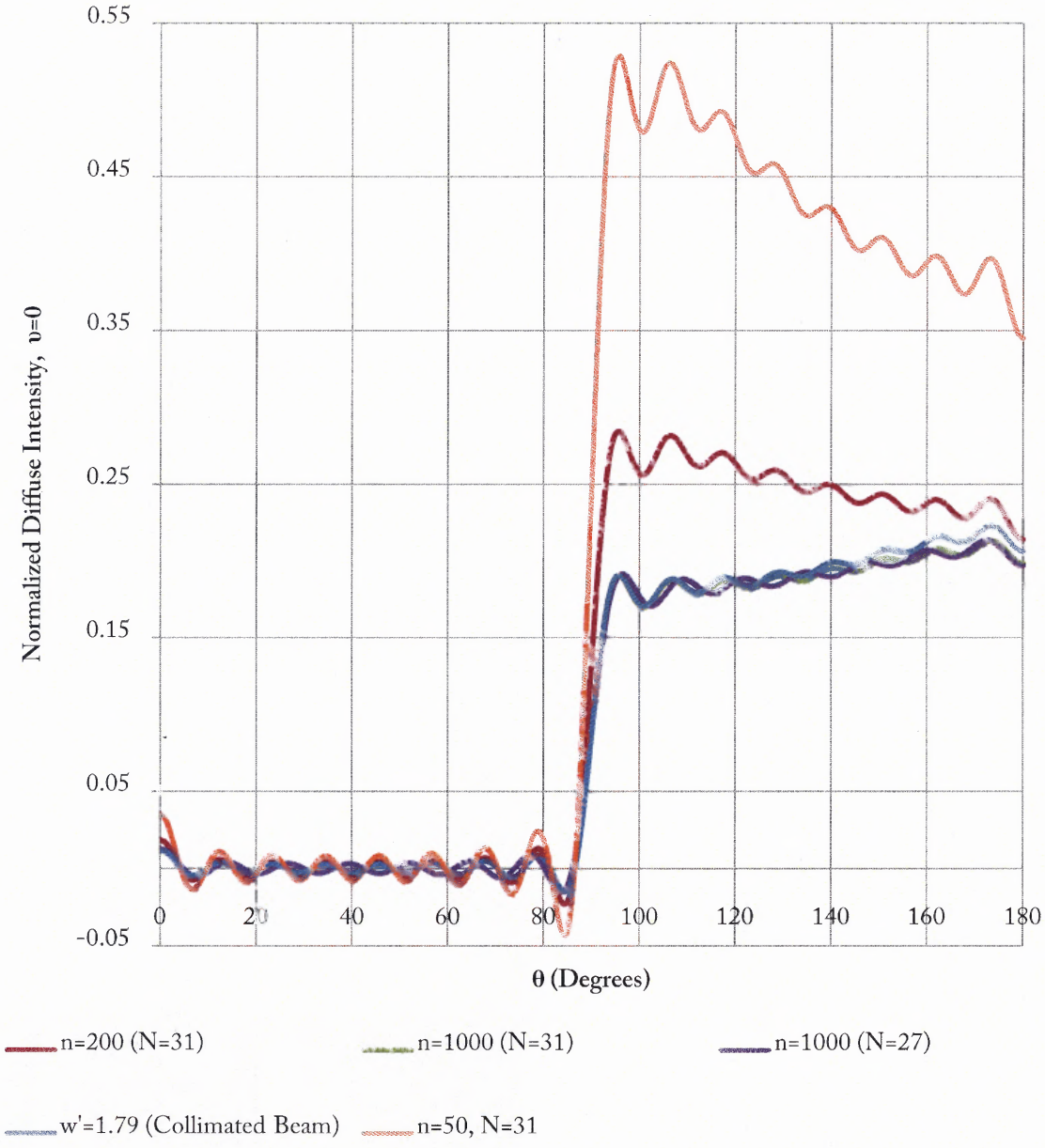

Figure 6 Boundary condition plot for the normalized diffuse intensity of different incident beam cases with $\rho' = 0.0$, $z' = 0.0$, $\theta = 0°$, $\psi = 0°$ versus the scattering angle θ. Other parameters include: $N = 31$, $\upsilon = 0$, and $z_0' = 40$; note: the values for the $\upsilon = 0$ diffuse intensity of the divergent beam have been normalized.

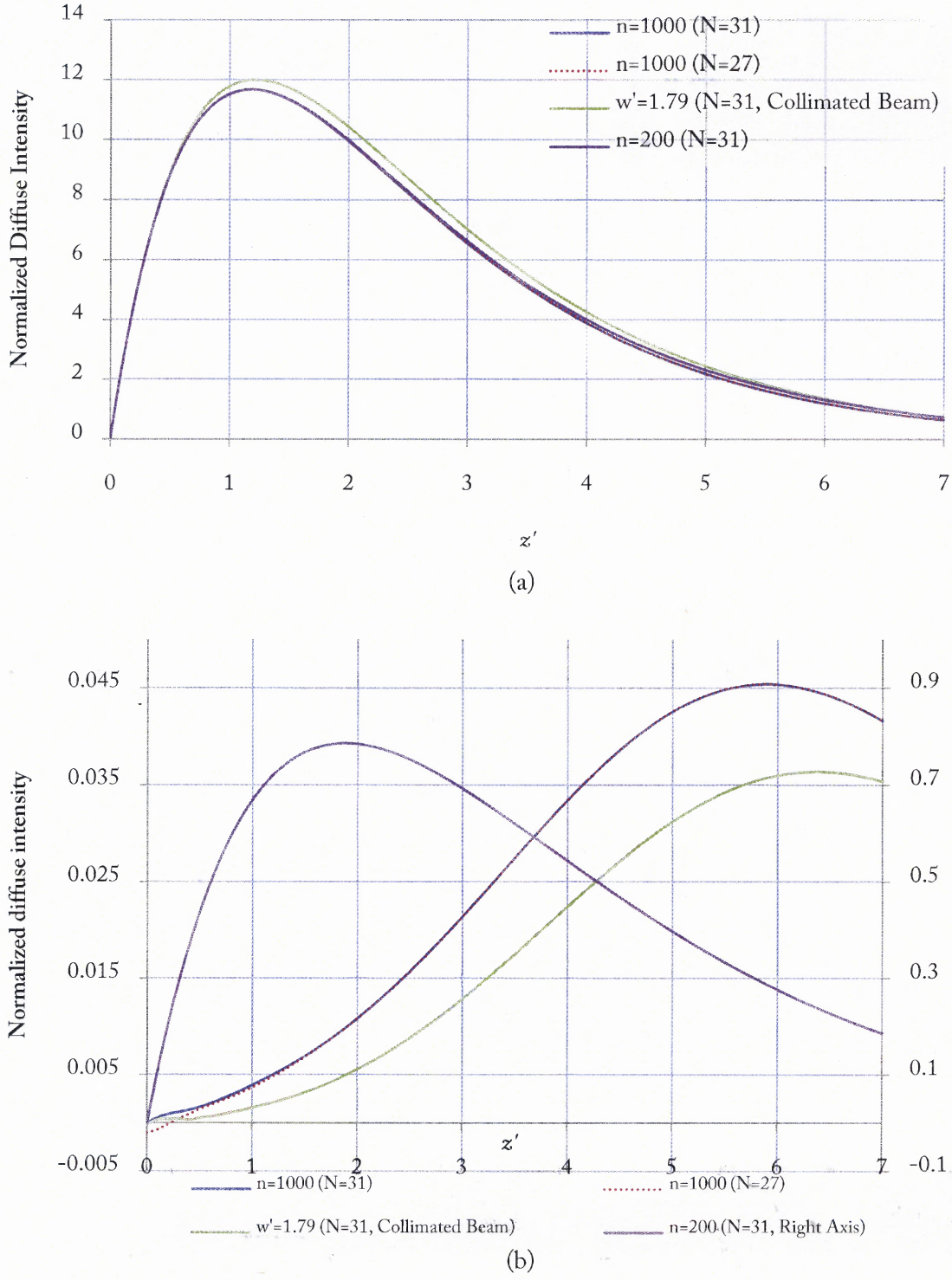

Figure 7 Normalized diffuse intensity versus the penetration depth: (a) $\rho' = 0.0$, $\theta = 0°$, $\psi = 0°$; and (b) $\rho' = 5.0$, $\theta = 30°$, $\psi = 0°$. Other parameters include: $N = 31$, $\upsilon = 0$, and $z'_0 = 40$; note: the curve with $n = 200$ uses the right axis and the remaining curves use the left axis.

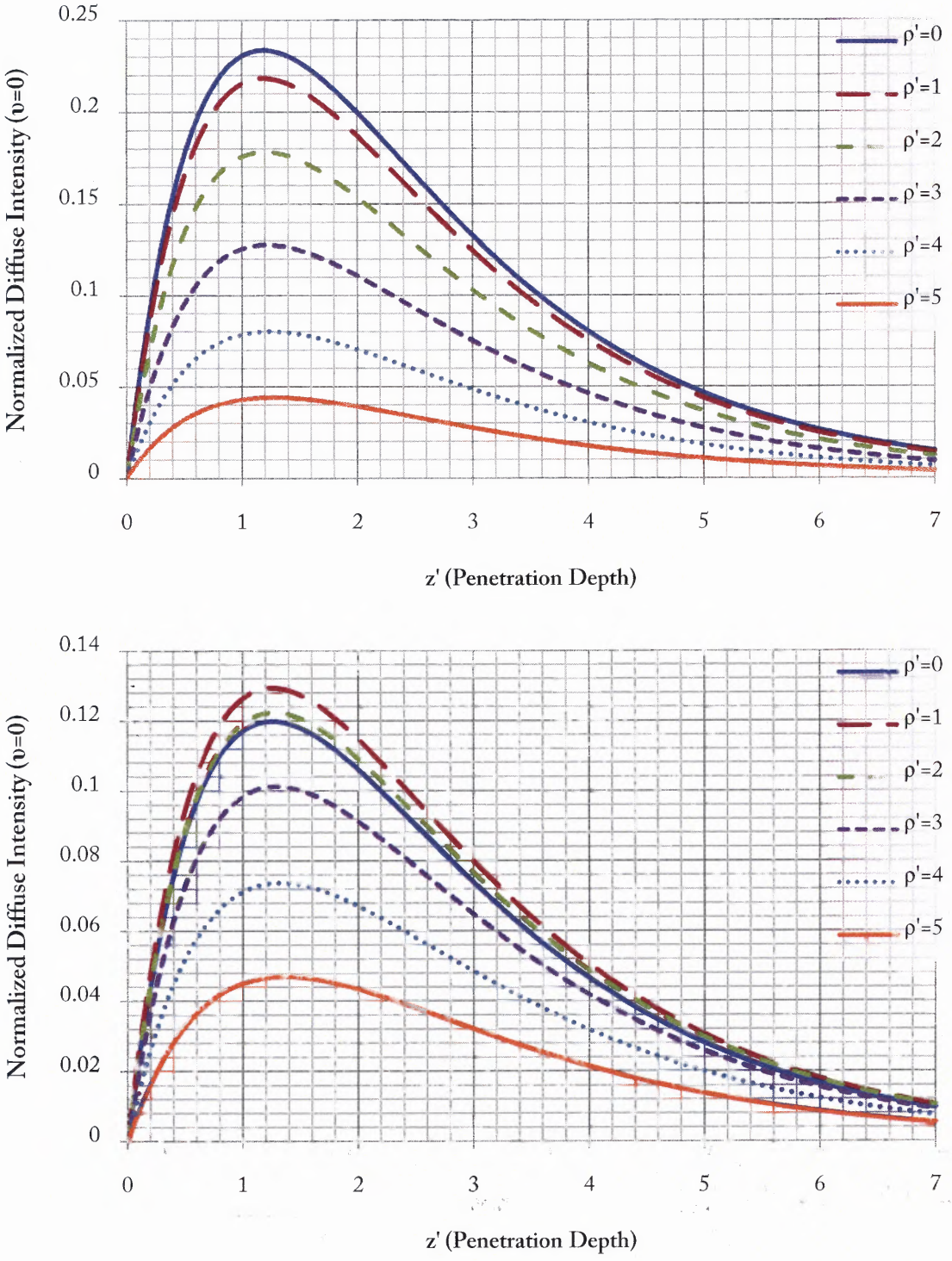

Figure 8 Normalized diffuse intensity versus the penetration depth: $\theta=0°$ (top) and $\theta=15°$, $\upsilon=0$ and $n=200$ for different values of ρ' ranging from 0 to 4.

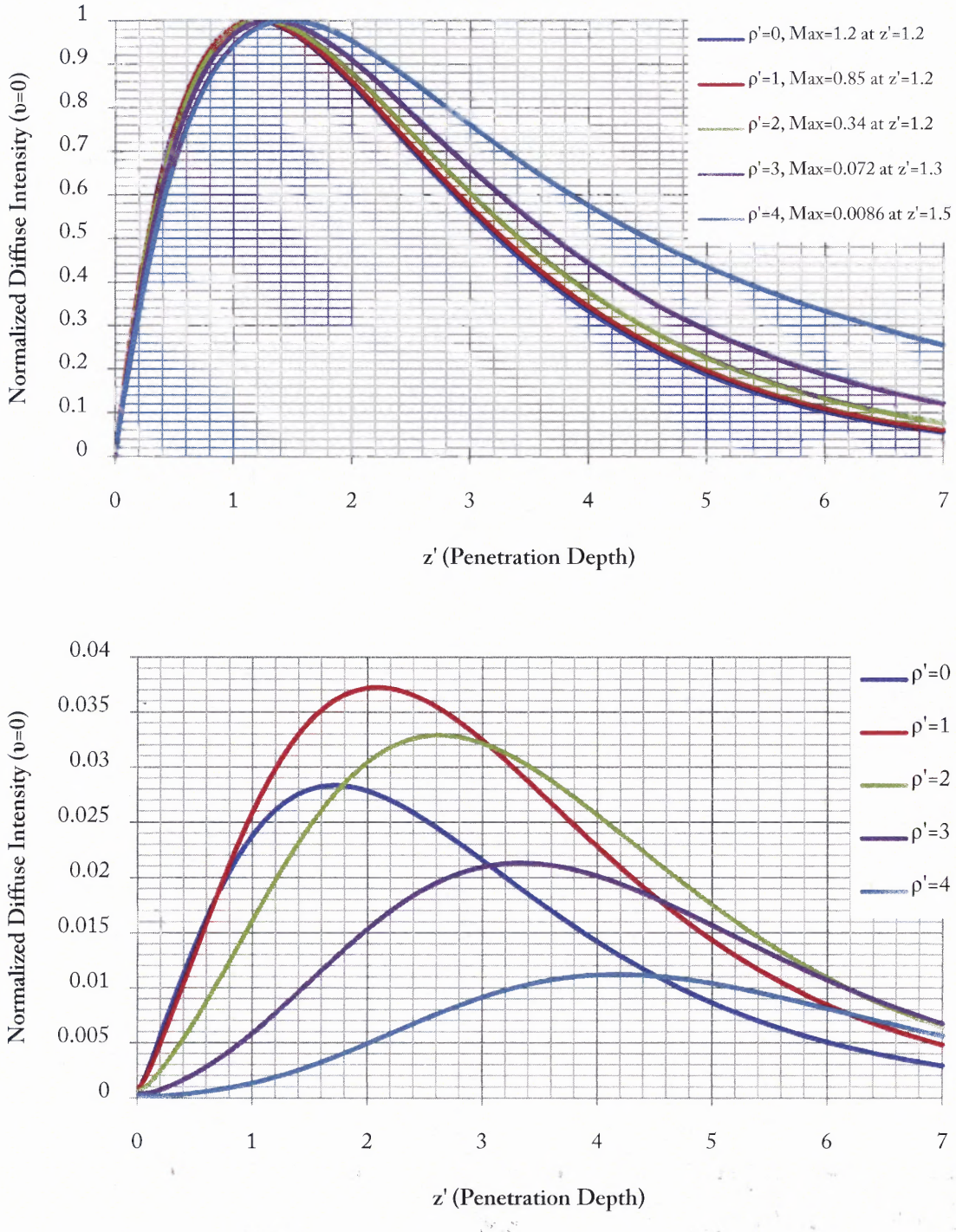

Figure 9 Normalized diffuse intensity versus the penetration depth when $n=1000$ (narrow beam): $\theta=0°$ (top) and $\theta=45°$ (bottom), and $\upsilon=0$ for different values of ρ'. In this plot, the pulse tends to "spread" as ρ' increases. In addition, because the values of the diffuse intensity differ greatly in the top graph, the diffuse intensity for the top graph has been normalized to 1.

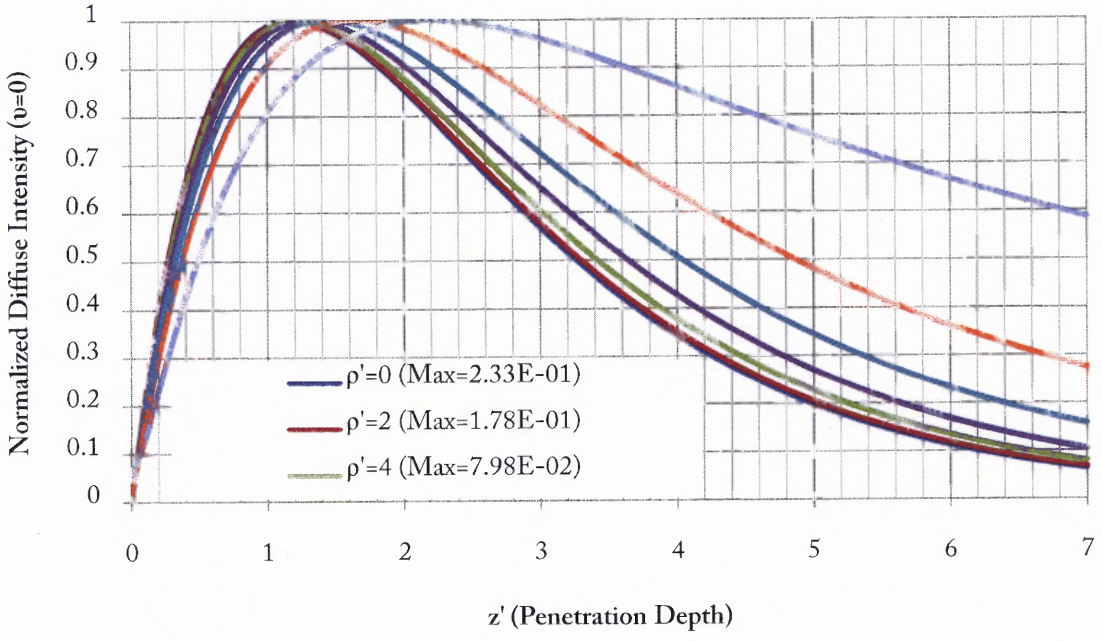

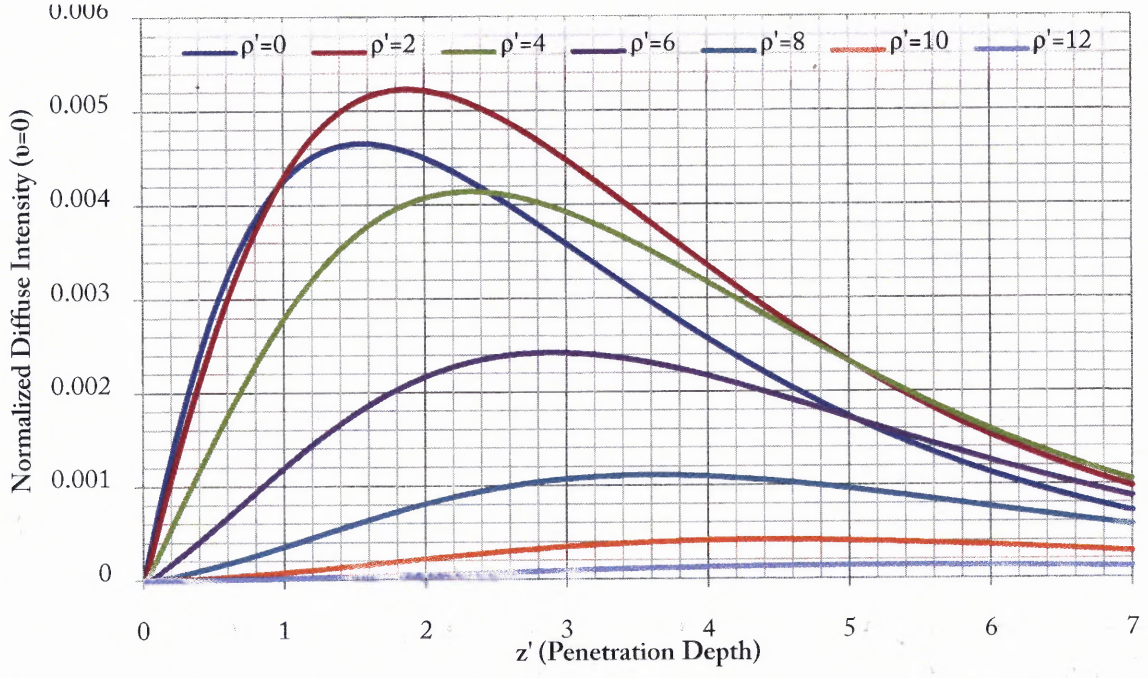

Figure 10 Normalized diffuse intensity versus the penetration depth when $n=200$: $\theta=0°$ (top) and $\theta=60°$ (bottom), $\psi=0°$, and $\upsilon=0$ for different values of ρ'. The top graph have been normalized to a maximum of one.

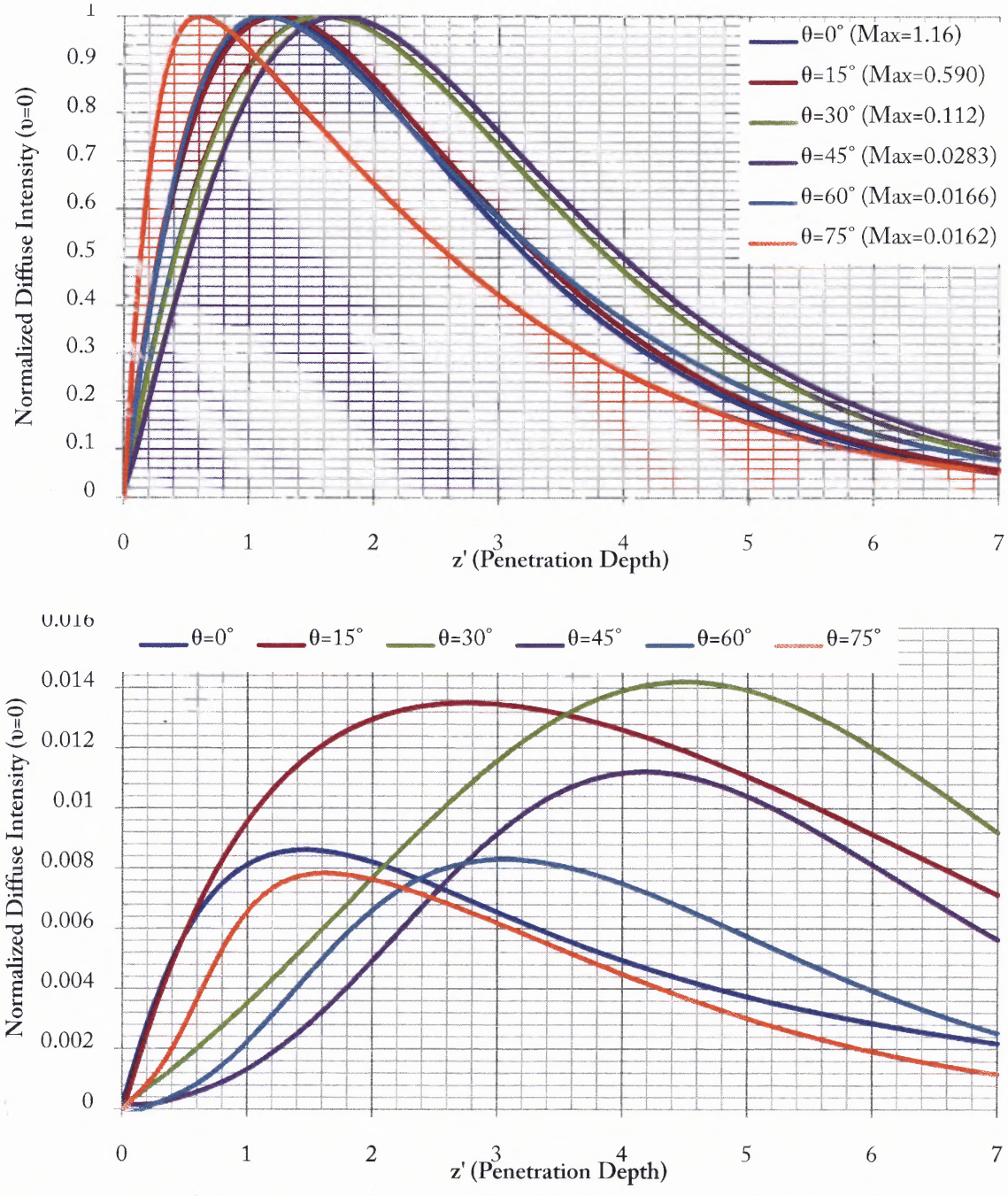

Figure 11 Normalized diffuse intensity versus the penetration depth when $n=1000$: $\rho'=0$ (top) and $\rho'=4$ (bottom), $\psi=0°$, and $\upsilon=0$ for different values of θ. Note: all of the curves on the upper graph are normalized to 1.

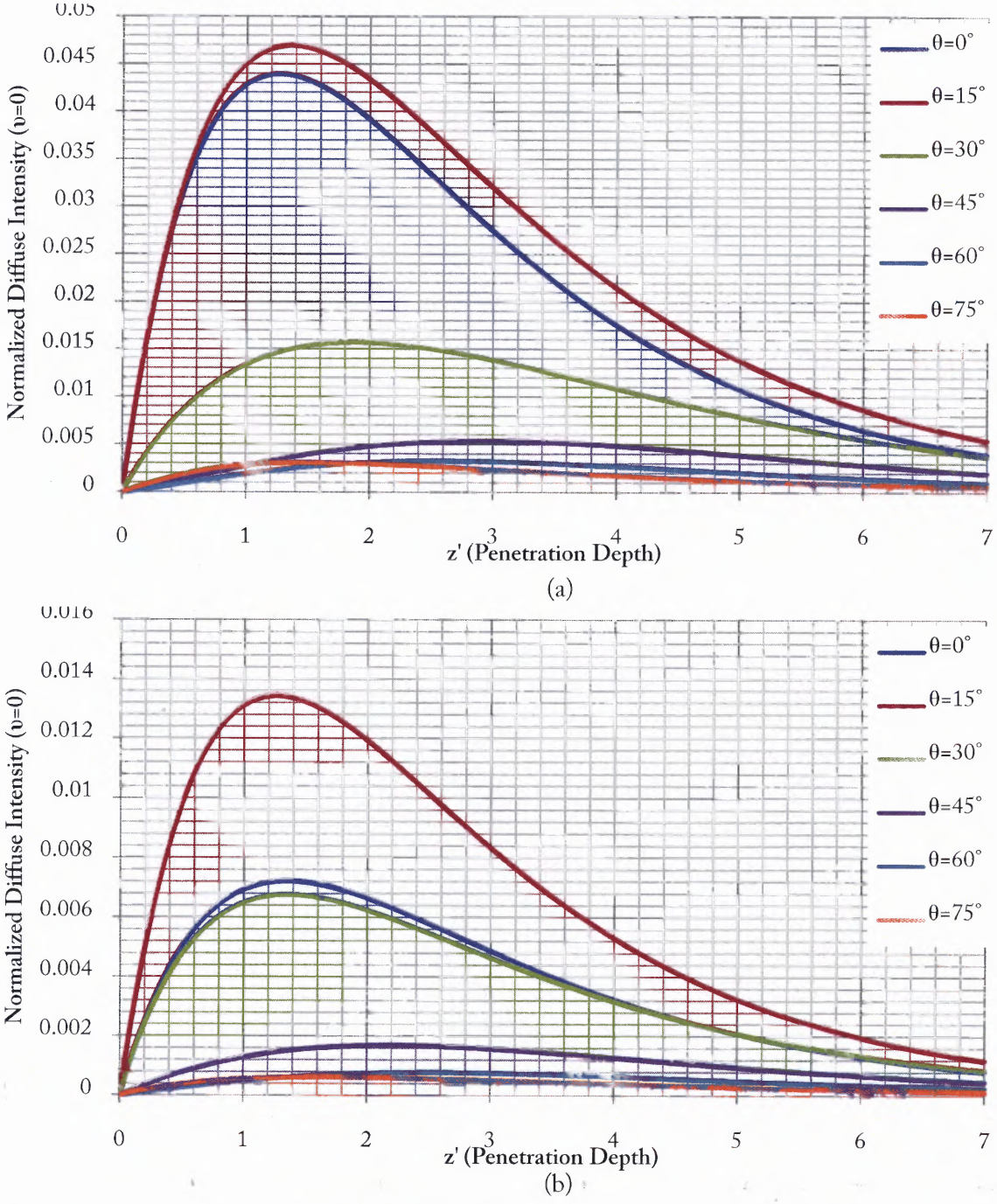

Figure 12 Normalized diffuse intensity versus the penetration depth: (a) $n=200$ and $\rho' = 5$ (b) $n=50$ and $\rho' = 10$.

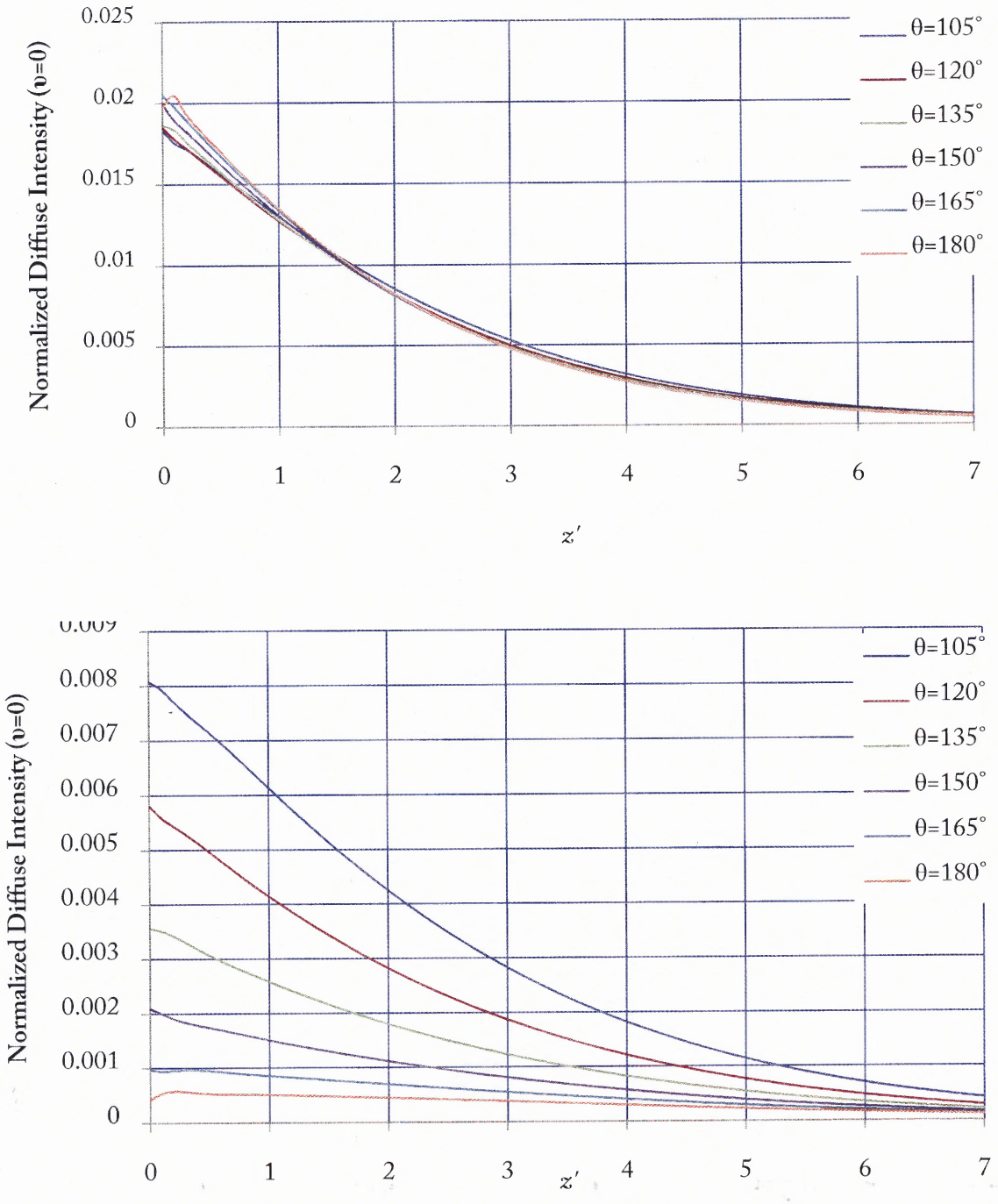

Figure 13 Normalized diffuse intensity versus the penetration depth z' when $n=1000$ (narrow incident beam), $\psi=0°$, and $\rho'=0$ (top) and $\rho'=4$ (bottom) for different values of θ.

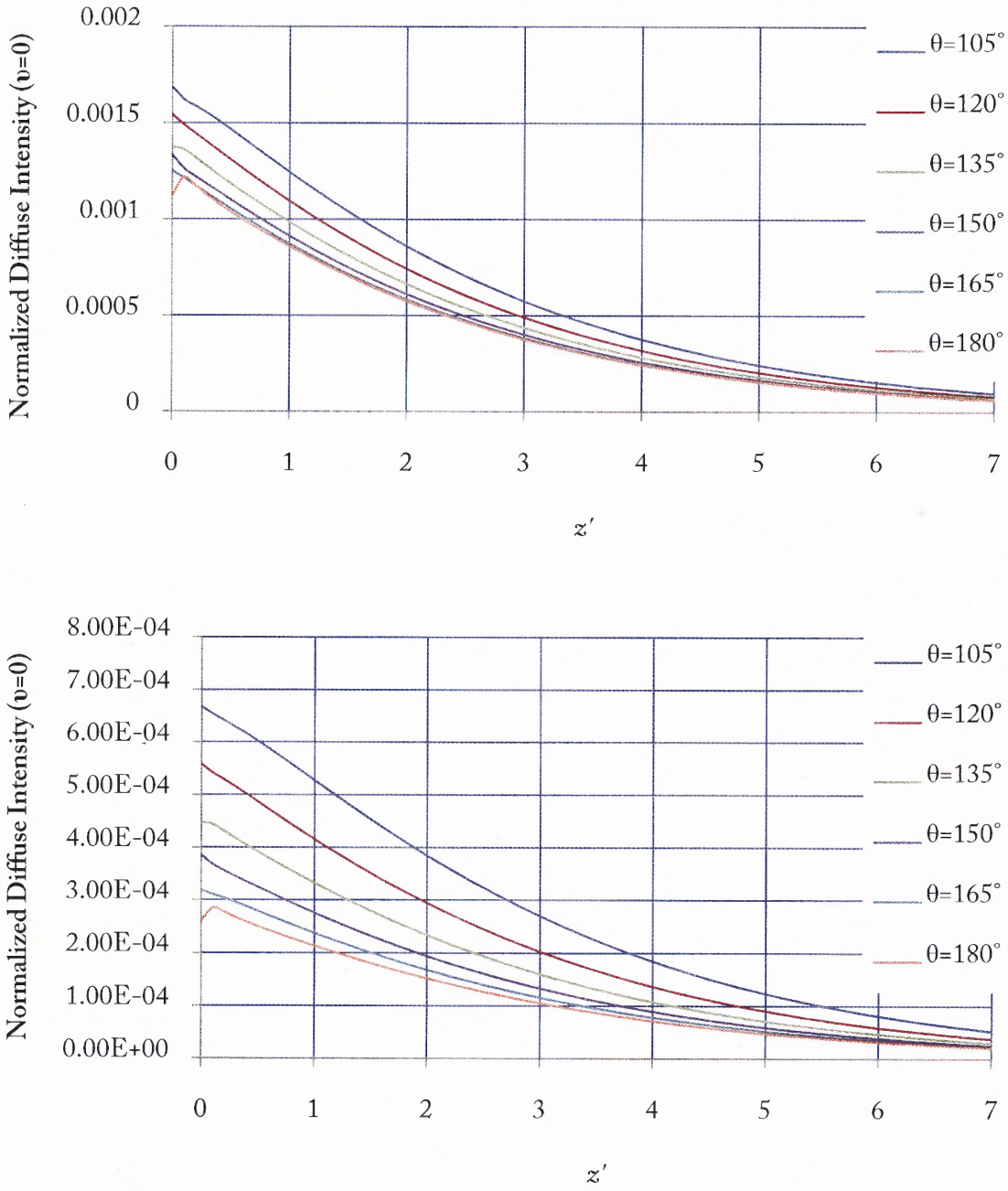

Figure 14 Normalized diffuse intensity versus the penetration depth z' when $n=50$ (wide incident beam), $\psi=0°$, and $\rho'=0$ (top) and $\rho'=10$ (bottom) for different values of θ.

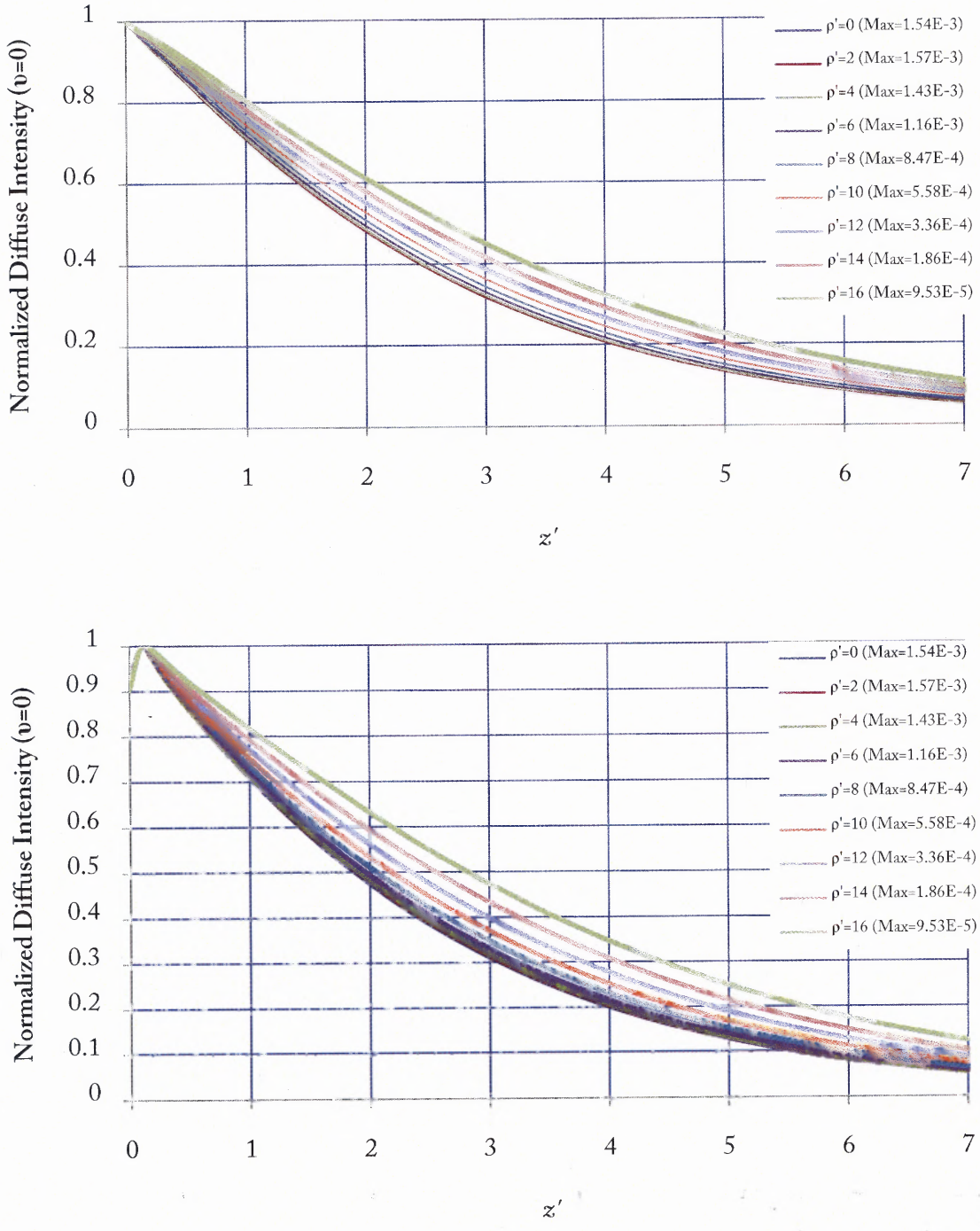

Figure 15 Normalized diffuse intensity versus the penetration depth z' when $n=50$ (wide incident beam), $\psi=0°$, and $\theta=120°$ (top) and $\theta=180°$ (bottom) for different values of ρ'. The normalized diffuse intensity in both of the graphs have been normalized to the maximum of one.

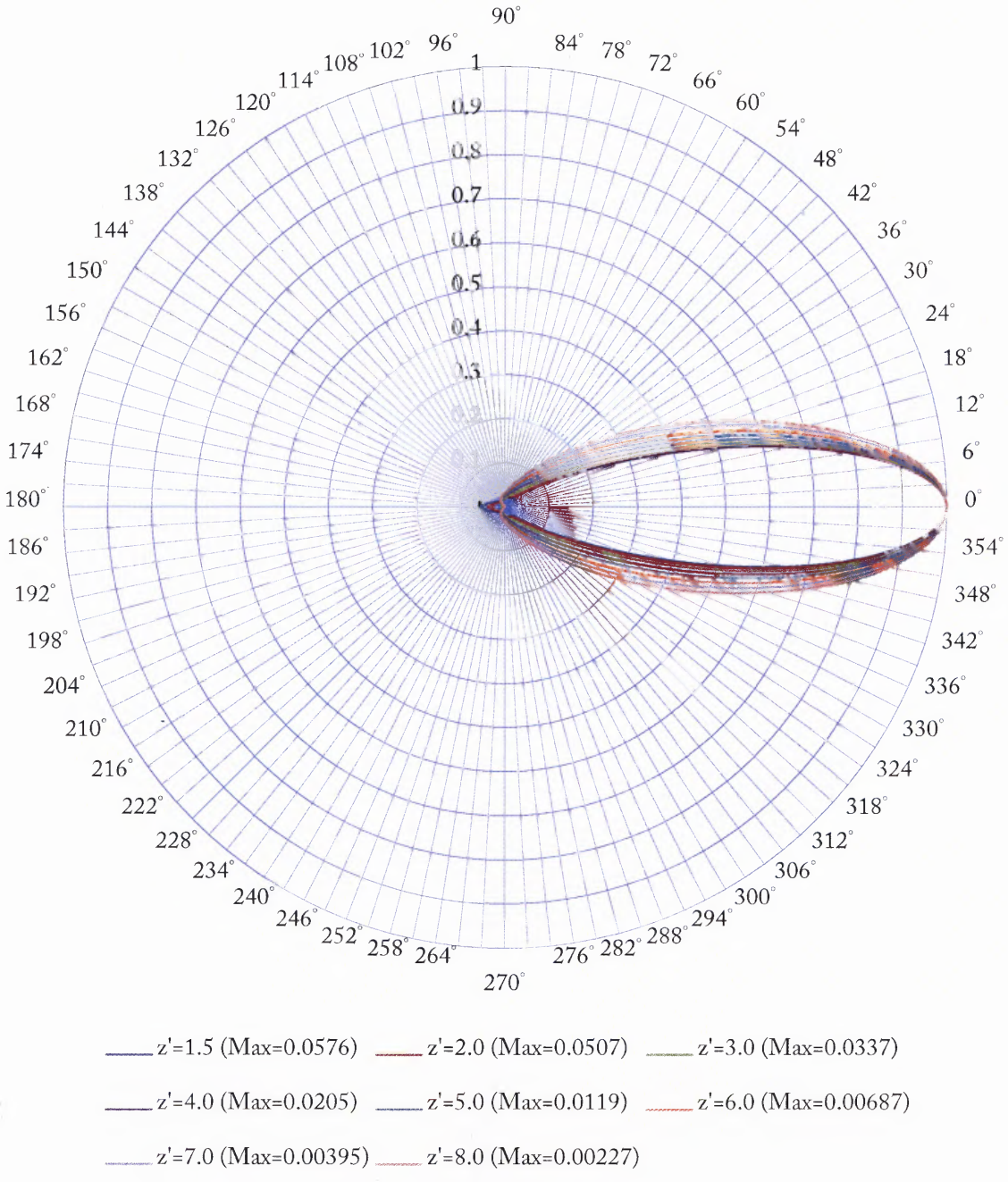

Figure 16 Normalized diffuse intensity versus the scattering angle θ when $n=50$, $\psi=0°,180°$, and $\rho'=0$ for different values of z': notice how the beam broadens as z' increases.

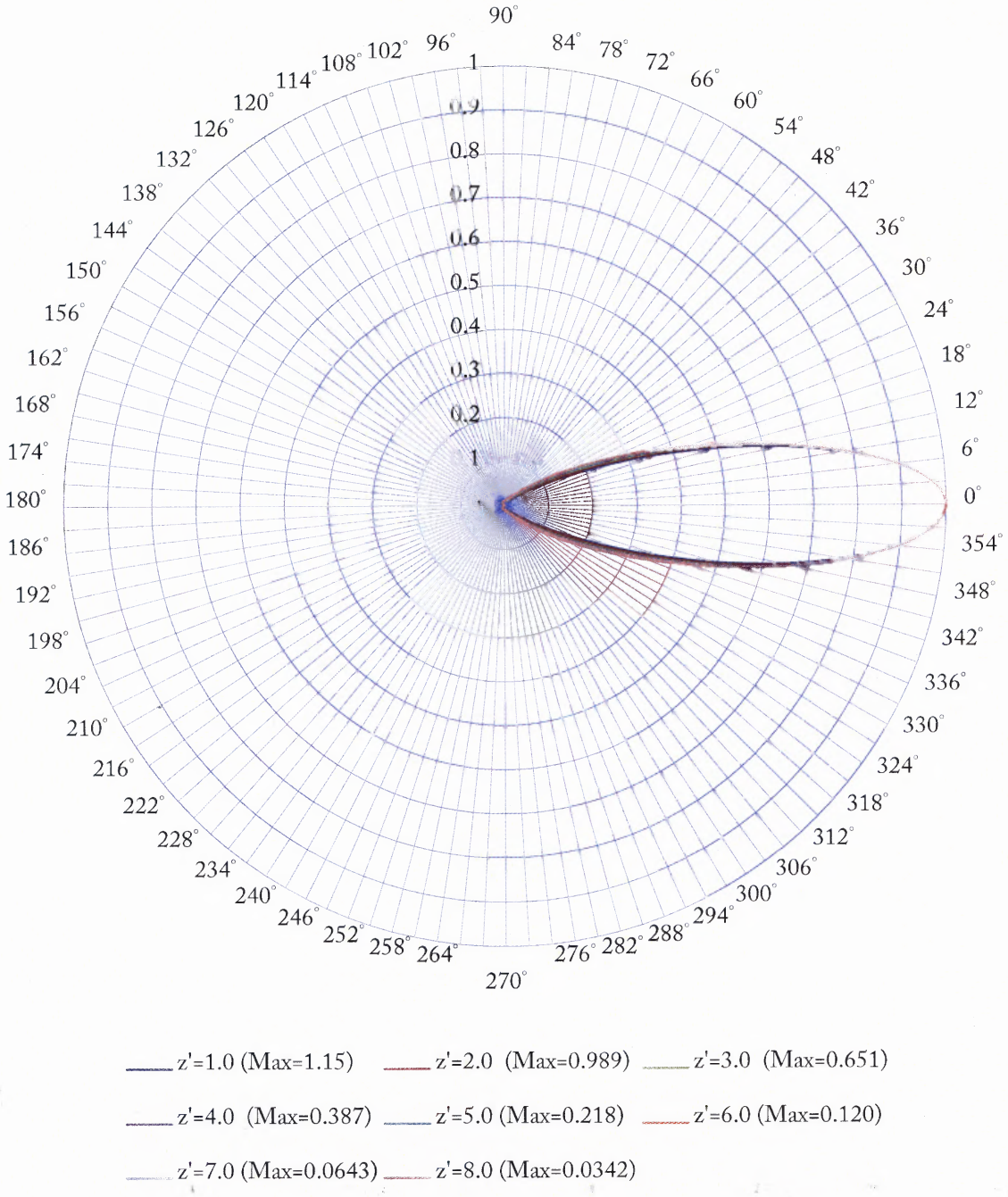

Figure 17 Normalized diffuse intensity versus the scattering angle θ when $n=1000$ (narrow incident beam), $\psi = 0°, 180°$, and $\rho' = 0$ for different values of z': notice how the beam broadens as z' increases.

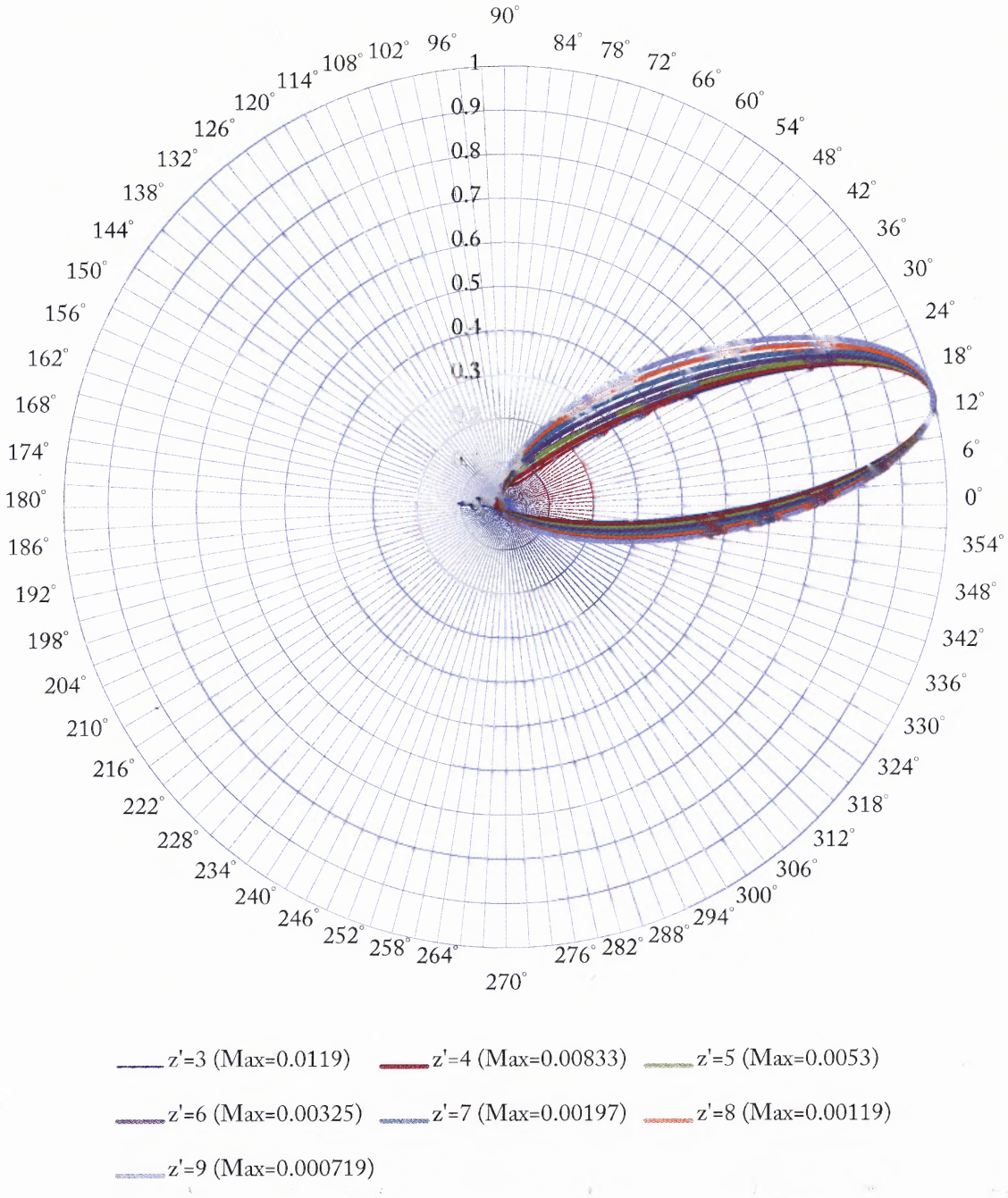

Figure 18 Normalized diffuse intensity versus the scattering angle θ when $n=50$, $\psi=0°,180°$, and $\rho'=10$ for different values of z': notice how the beam broadens as increases. These curves have been normalized to a maximum of a unity.

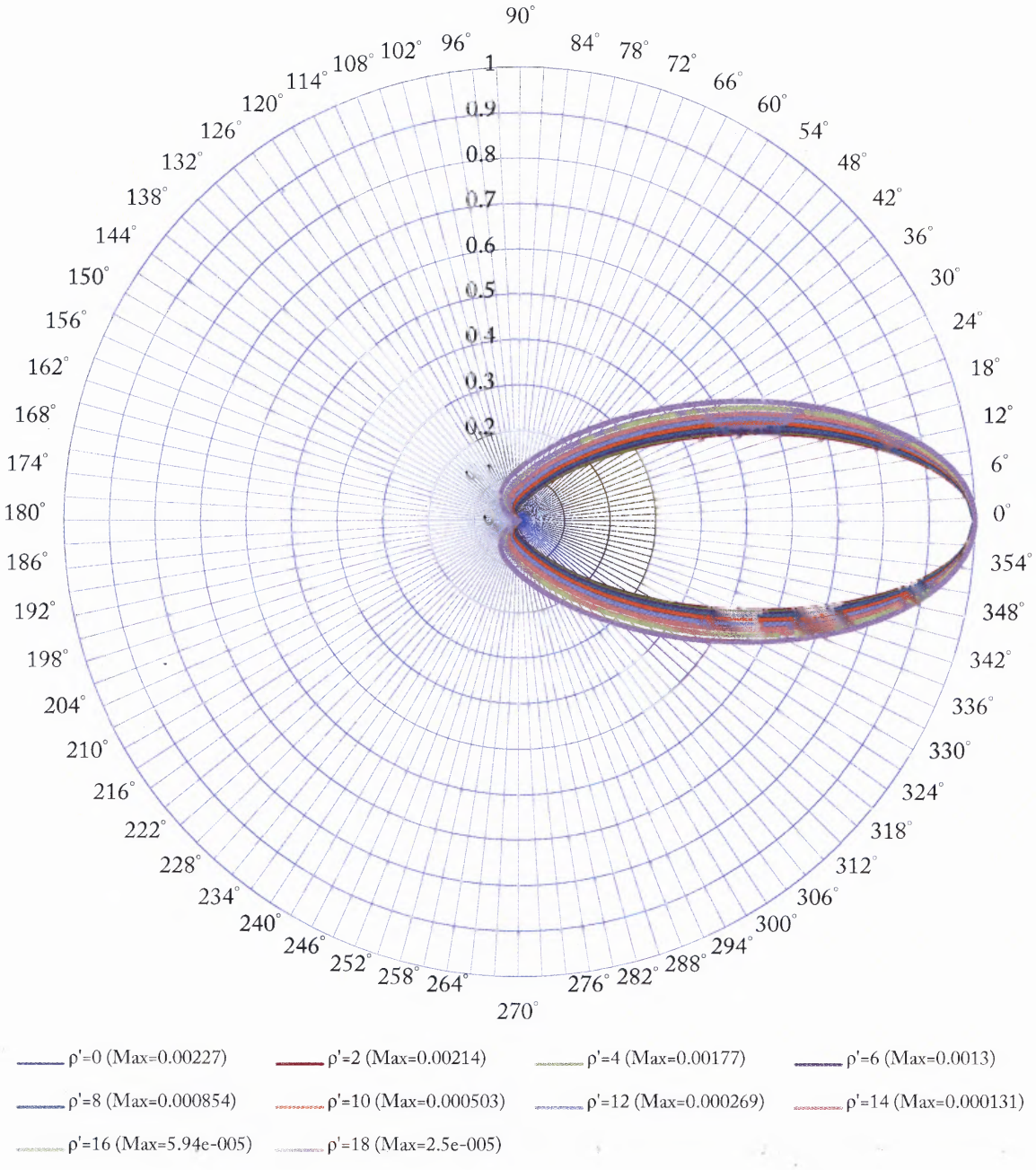

Figure 19 Normalized diffuse intensity versus the scattering angle θ when $n=50$, $\psi=-90°, 90°$, and $z'=8$ for different values of ρ': notice how the beam broadens as ρ' increases.

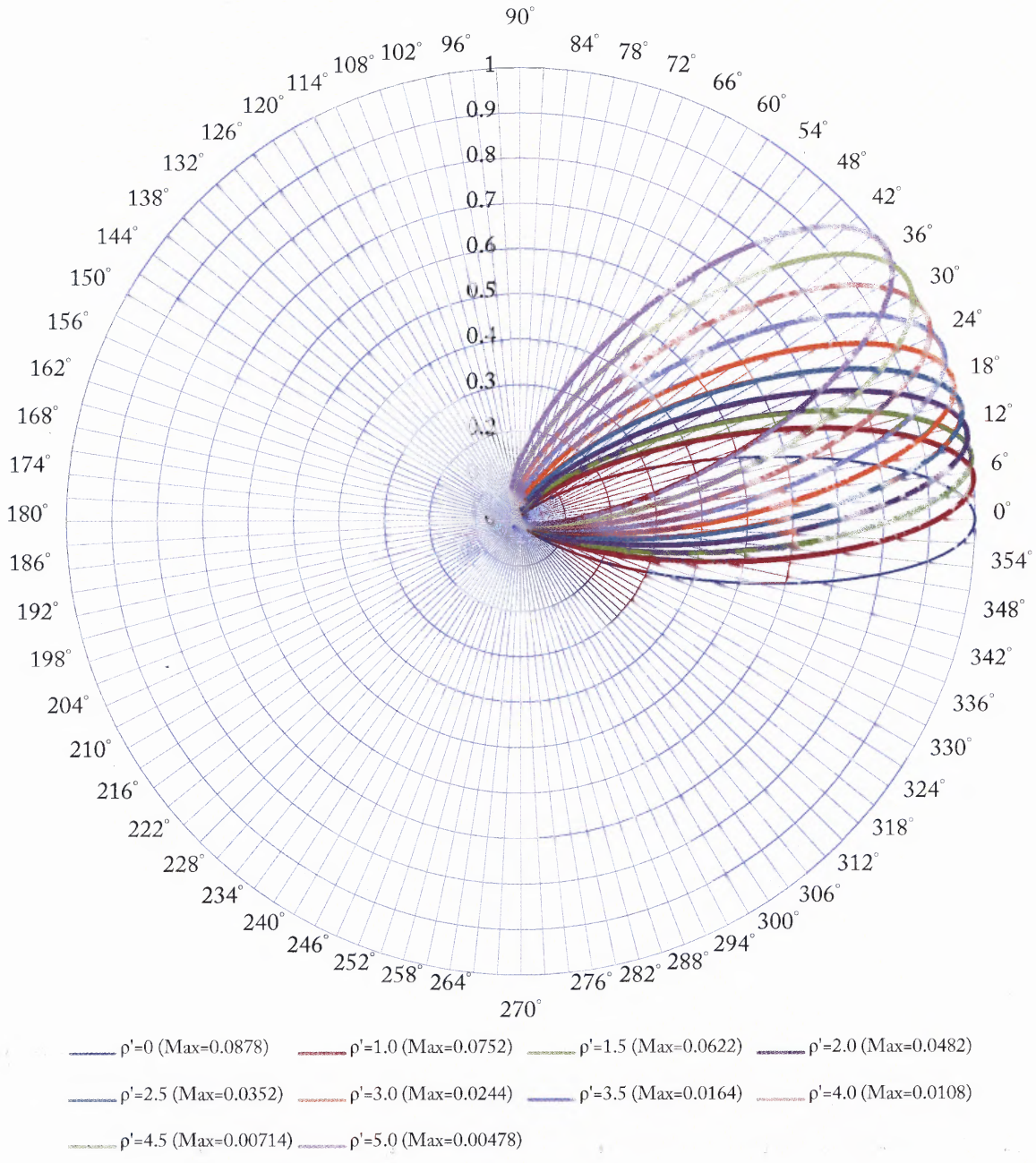

Figure 20 Normalized diffuse intensity versus the scattering angle θ when $n=1000$ (narrow incident beam), $\psi = 0°, 180°$, and $z' = 6.5$ for different values of ρ'

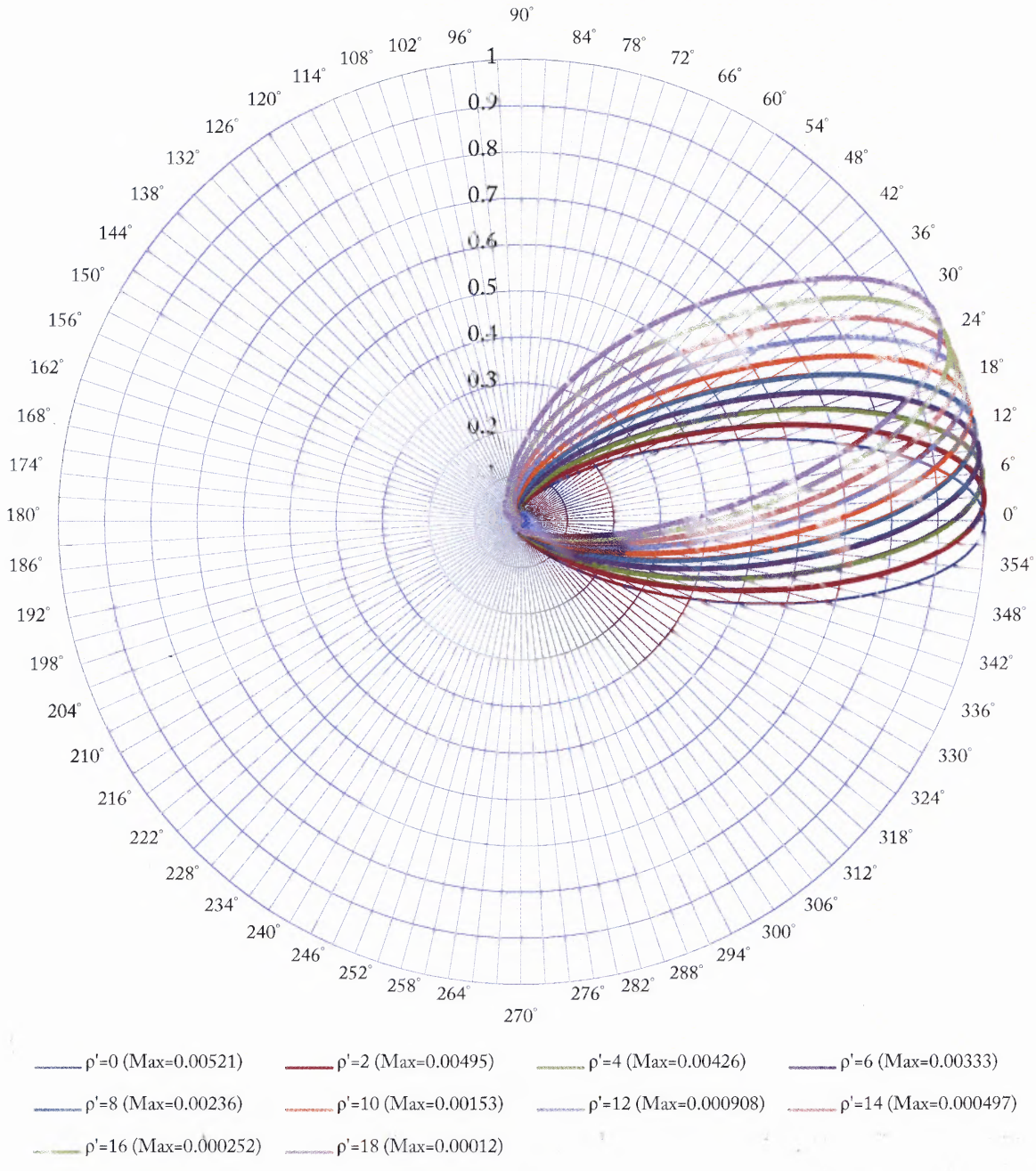

Figure 21 Normalized diffuse intensity versus the scatter angle θ when $n=50$ (wide incident beam), $\psi = 0°, 180°$, and $z' = 6.5$ for different values of ρ' : notice how the beam tilts slightly upwards as ρ' increases while getting smaller.

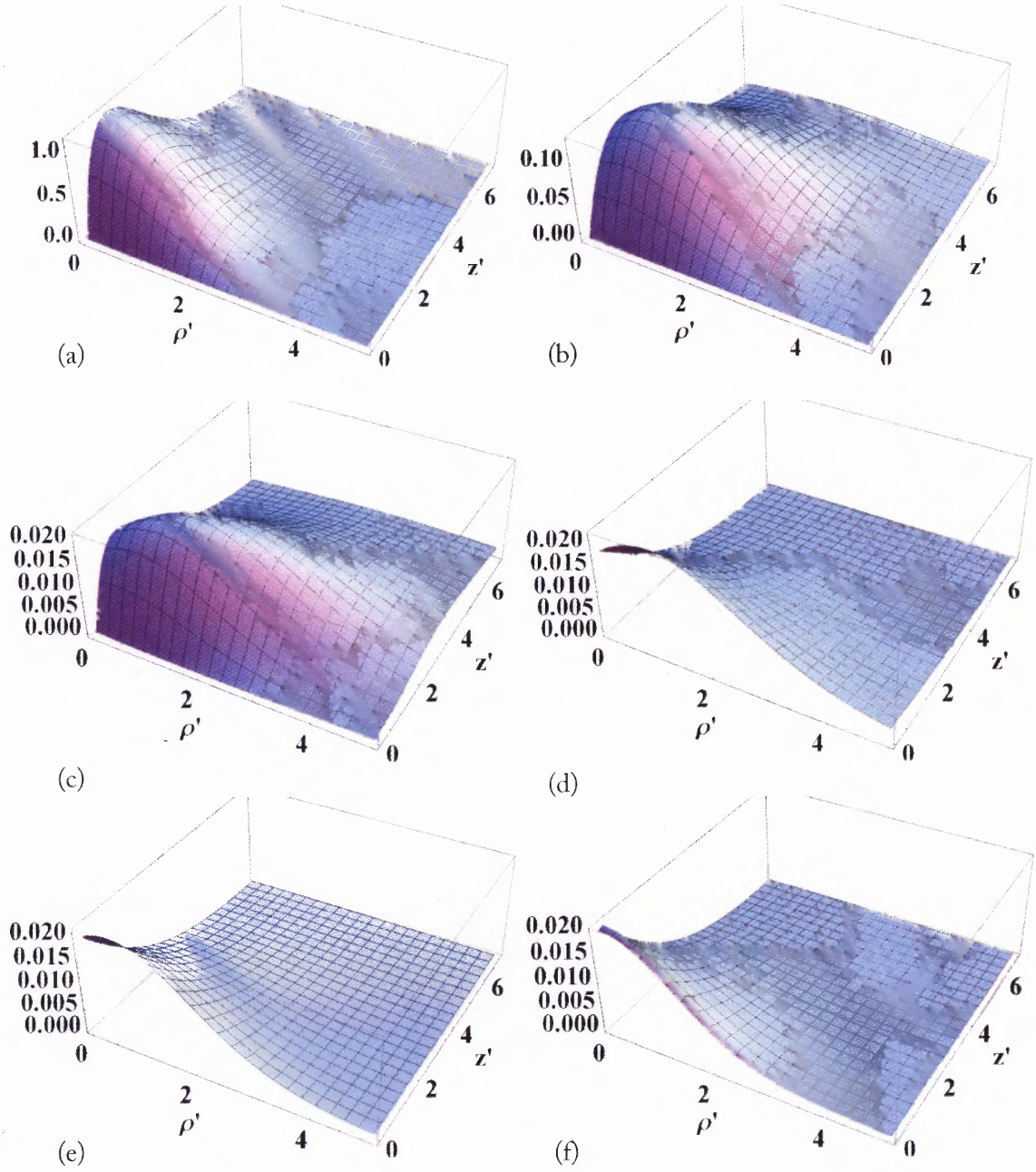

Figure 22 Three-dimensional graphs for $I_{d,0}(\rho',z';\theta,\psi=0)$ vs (ρ',z') when $n=1000$, where (a) $\theta=0°$, (b) $\theta=30°$ (c) $\theta=60°$ (d) $\theta=120°$ (e) $\theta=150°$ (f) $\theta=180°$.

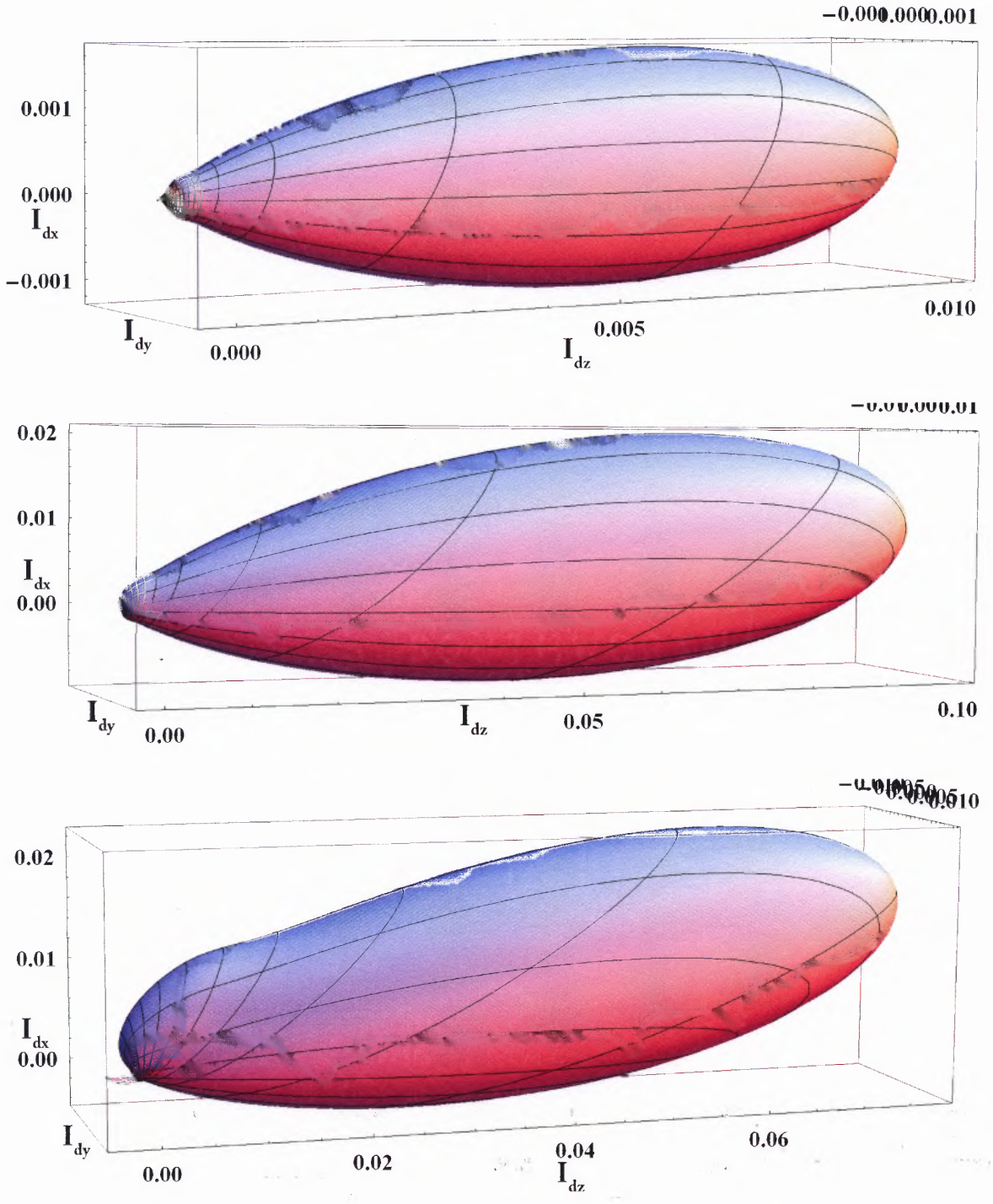

Figure 23 Radiation scattering plots for $I_{d,0}(\rho',z';\theta,\psi)$ versus (θ,ψ) in spherical coordinate, where $\rho'=6, z'=3$ and $n=50$ (top), $n=200$ (middle), and $n=1000$ (bottom); note there's a very small backscattering lobe and that y-axis is the same scale as the x-axis.

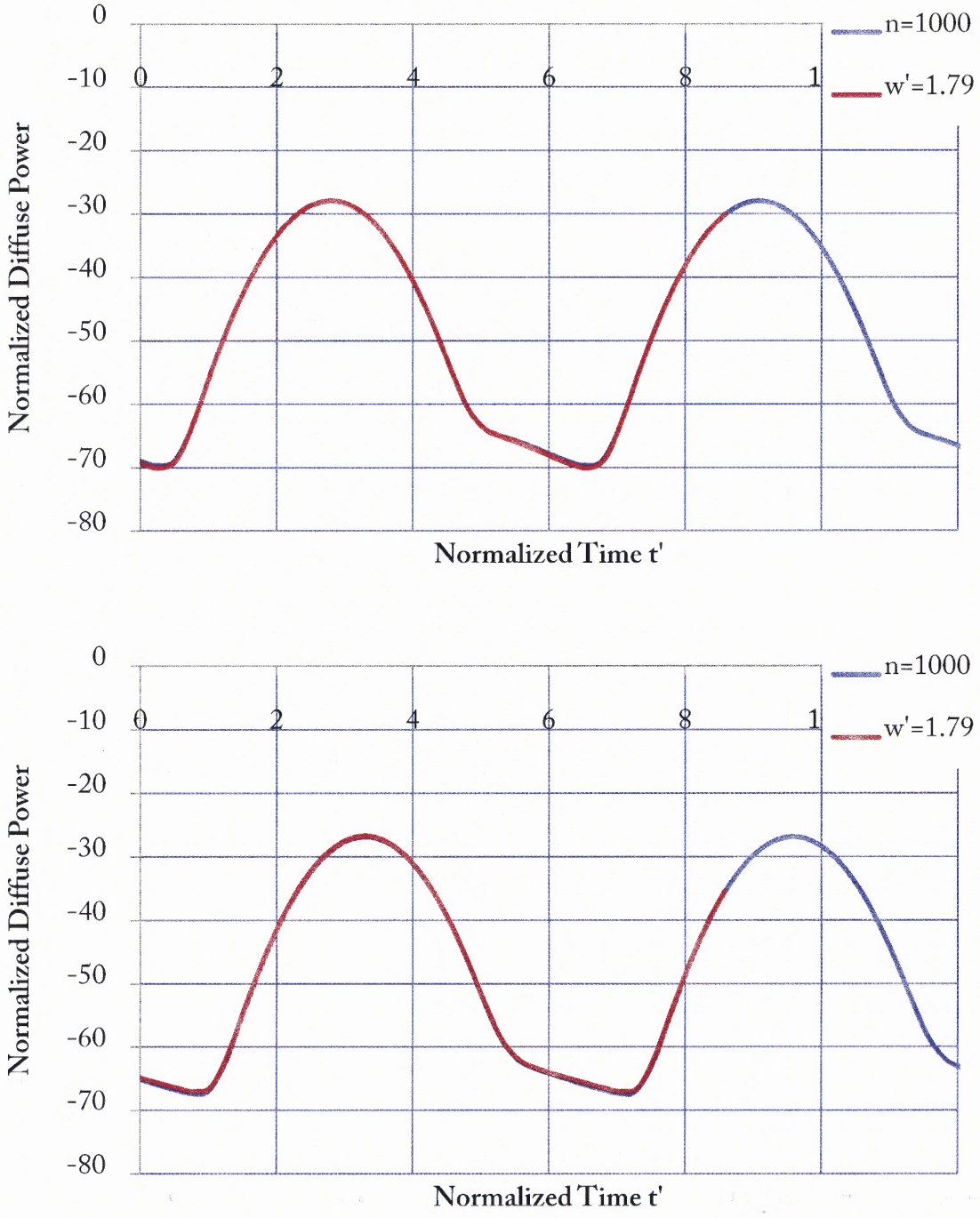

Figure 24 Normalized diffuse power versus normalized time comparing the divergent incident beam ($n=1000$) with the incident collimated beam case ($w'=1.79$) for $z'=0.5$ (top), $z'=1.0$ (bottom), $\theta=0°$, $\psi=0°$. Other parameters include: $N=31$, $\upsilon_{max}=15$, and $z'_0=40$. Note: the curves for the collimated beam have been synchronized to the divergent beam for better comparisons.

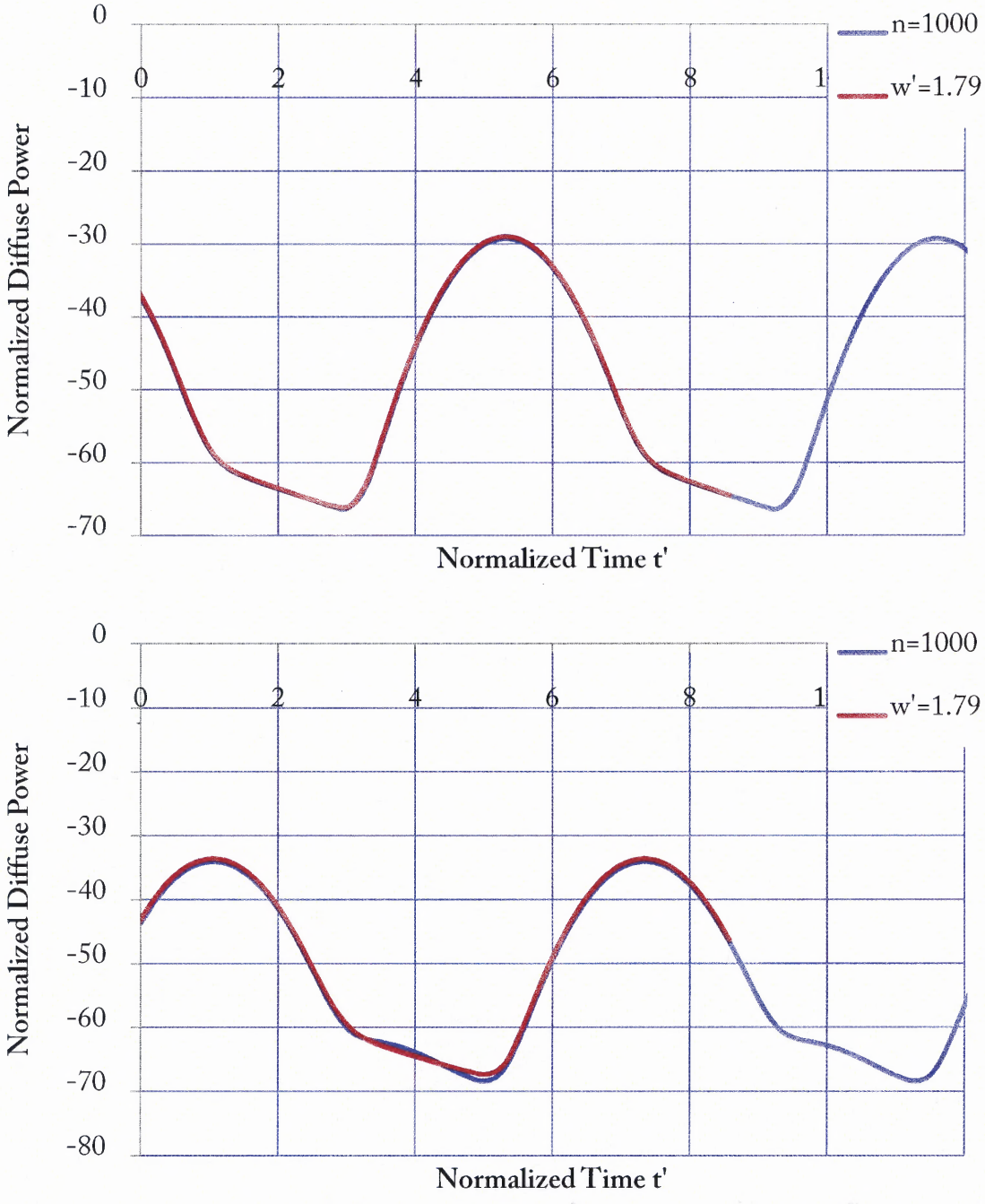

Figure 25 Normalized diffuse power versus normalized time comparing the divergent incident beam ($n=1000$) with the incident collimated beam case ($w'=1.79$) for $\rho'=0$, $z'=3.0$ (top), $z'=5.0$ (bottom), $\theta=0°$, $\psi=0°$. Other parameters include: $N=31$, $\upsilon_{max}=15$, and $z'_0=40$. Note: the curves for the collimated beam have been synchronized to the divergent beam for better comparisons.

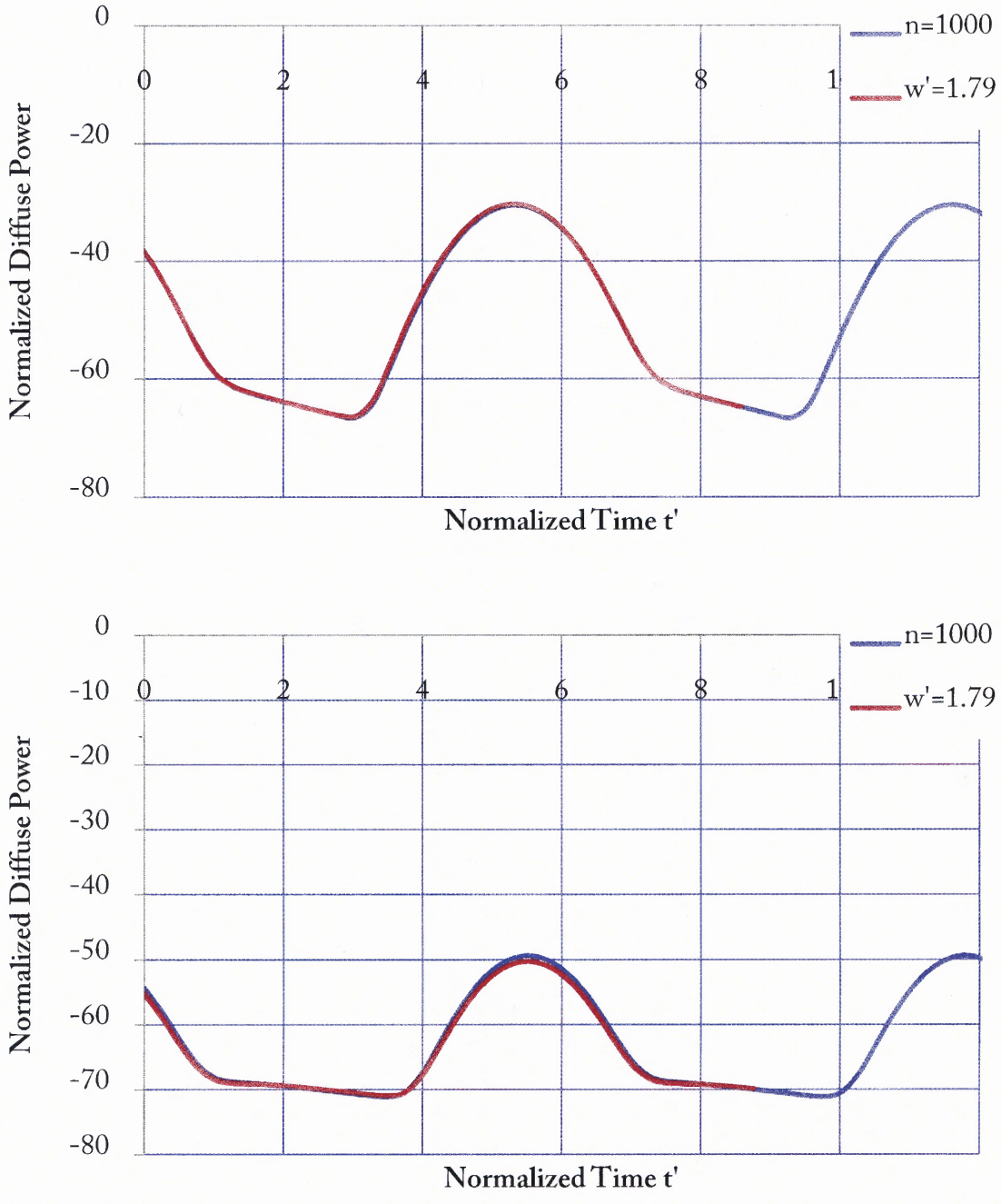

Figure 26 Normalized diffuse power versus normalized time comparing the divergent incident beam ($n=1000$) with the incident collimated beam case ($w'=1.79$) for $\rho'=1.0$ (top), $\rho'=4.0$ (bottom), $z'=3.0$, $\theta=0°$, $\psi=0°$. Other parameters include: $N=31$, $\upsilon_{max}=15$, and $z_0'=40$. Note: the curves for the collimated beam have been synchronized to the divergent beam for better comparisons.

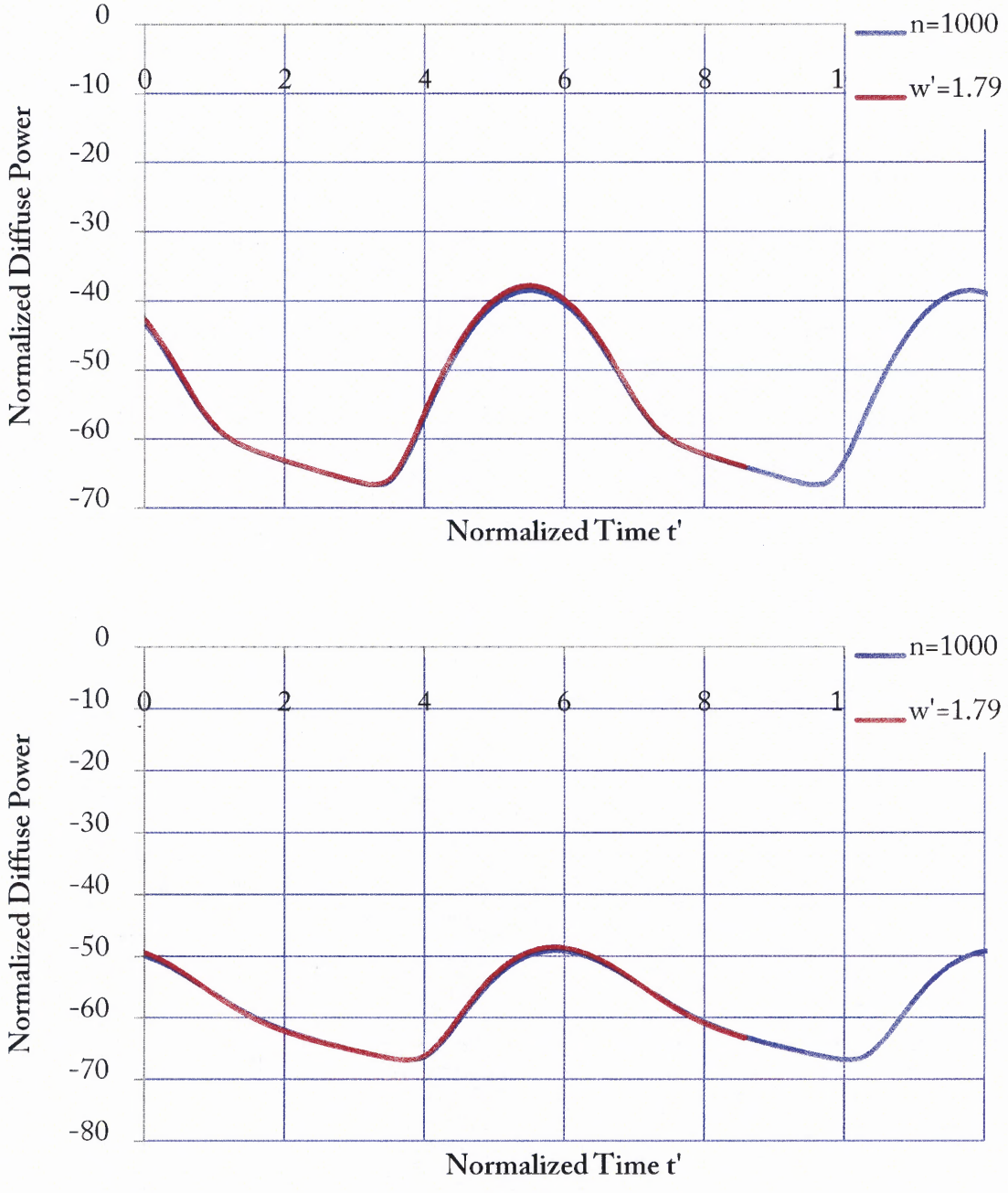

Figure 27 Normalized diffuse power versus normalized time comparing the divergent incident beam ($n=1000$) with the incident collimated beam case ($w'=1.79$) for $\rho'=0.0$, $z'=3.0$, $\theta=30°$ (top), $\theta=60°$ (bottom), $\psi=0°$. Other parameters include: $N=31$, $\upsilon_{max}=15$, and $z'_0=40$. Note: the curves for the collimated beam have been synchronized to the divergent beam for better comparisons.

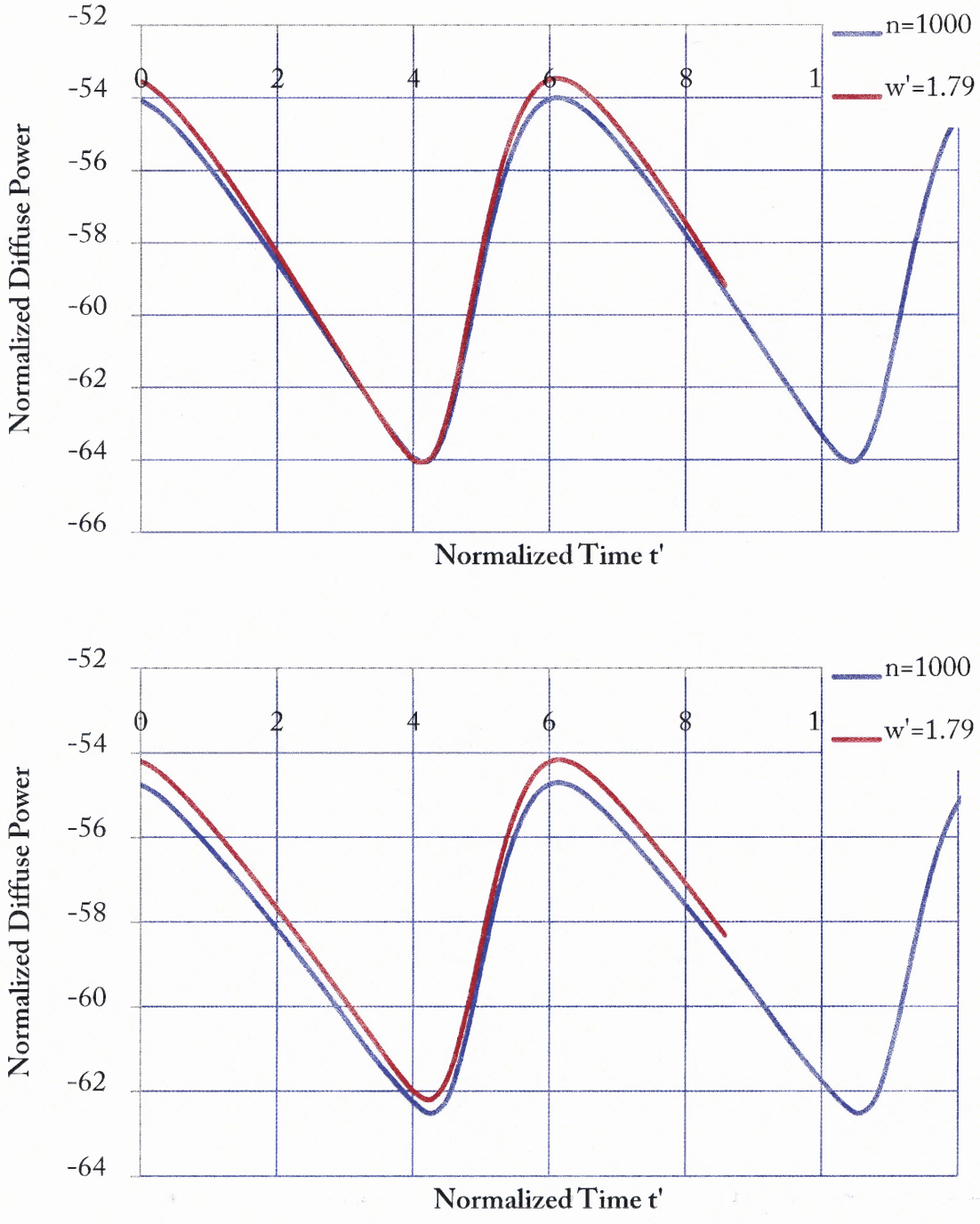

Figure 28 Normalized diffuse power versus normalized time comparing the divergent incident beam ($n=1000$) with the incident collimated beam case ($w'=1.79$) for $\rho'=0.0$, $z'=3.0$, $\theta=120°$ (top), $\theta=150°$ (bottom), $\psi=0°$. Other parameters include: $N=31$, $v_{max}=15$, and $z'_0=40$. Note: the curves for the collimated beam have been synchronized to the divergent beam for better comparisons.

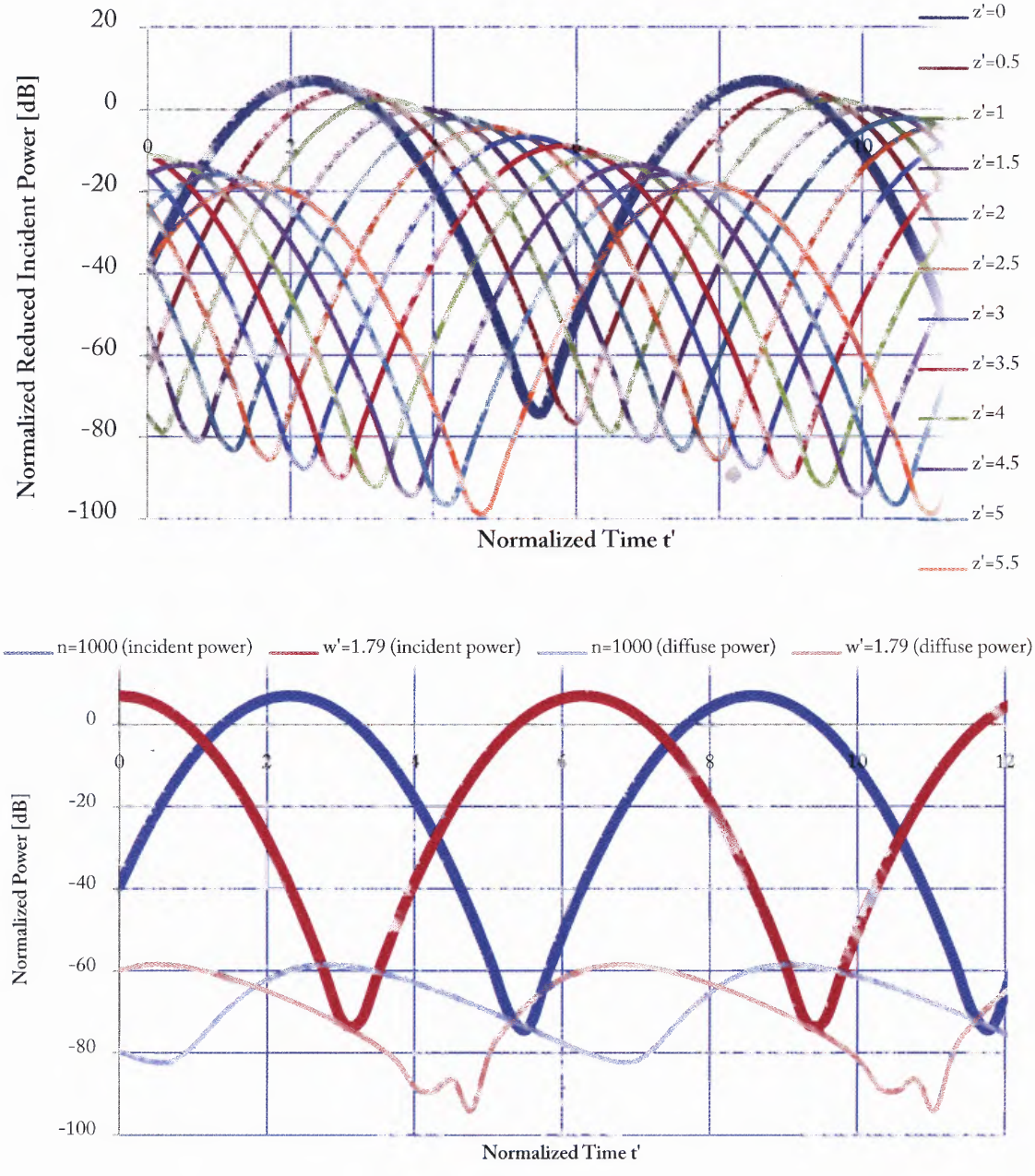

Figure 29 Normalized power versus normalized time for different values of z' (top) and for different types of incident beams when $z'=0$ (bottom): note that the thick lines are the reduced incident power at the origin, where the incident beam starts to penetrate into the forest, or, namely, the incident power. In addition, the thin lines on the lower graph are the diffuse power at the boundary, which is essentially 0. Other parameters include: $N=31$, $\upsilon_{max}=15$, $\theta=0$, and $\psi=0$.

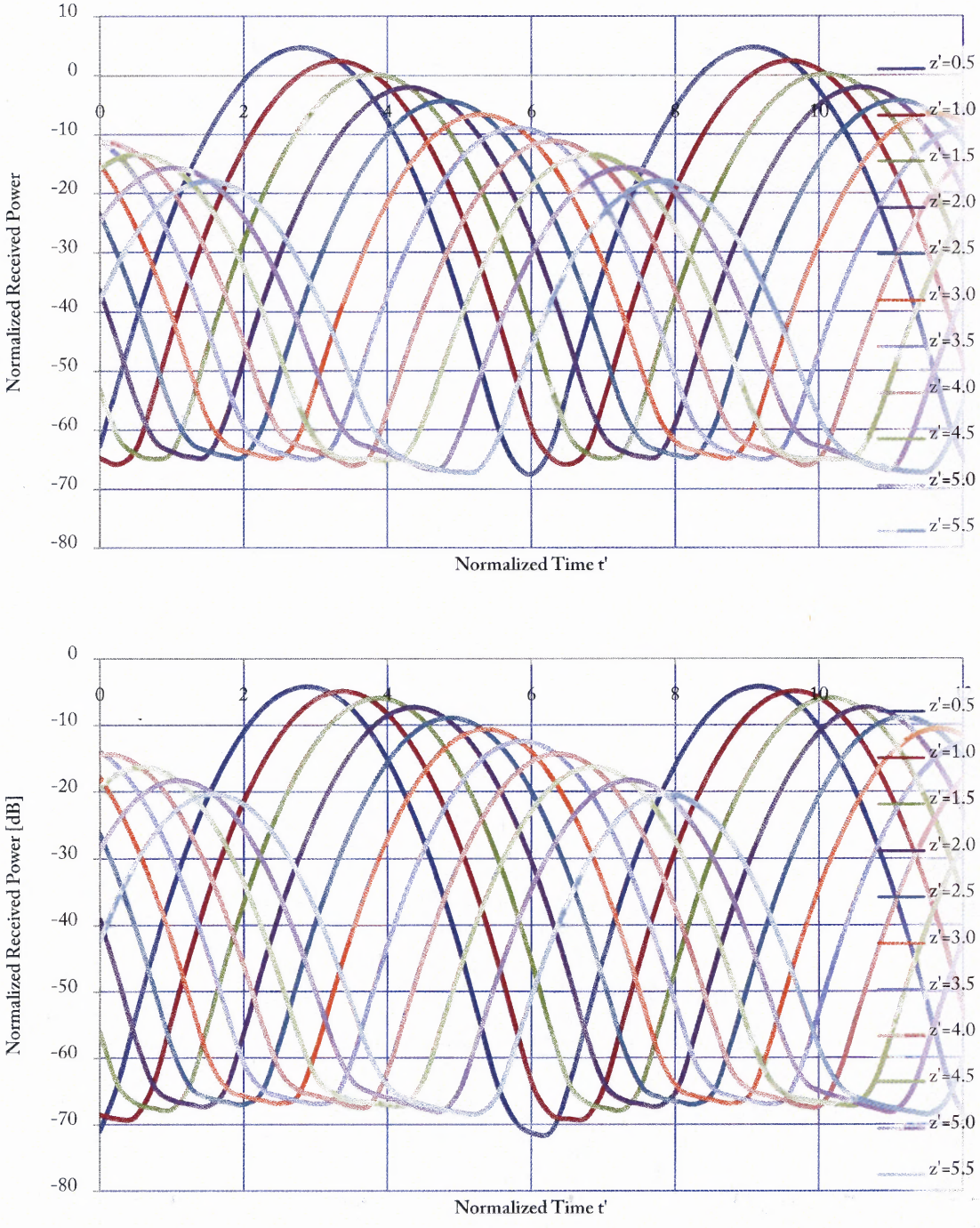

Figure 30 Normalized received power verus normalized time for $n=1000$, $\rho'=0$ (top) and $\rho'=2.5$ (bottom), $\theta=0°$, and $\psi=0°$ versus different values of z'

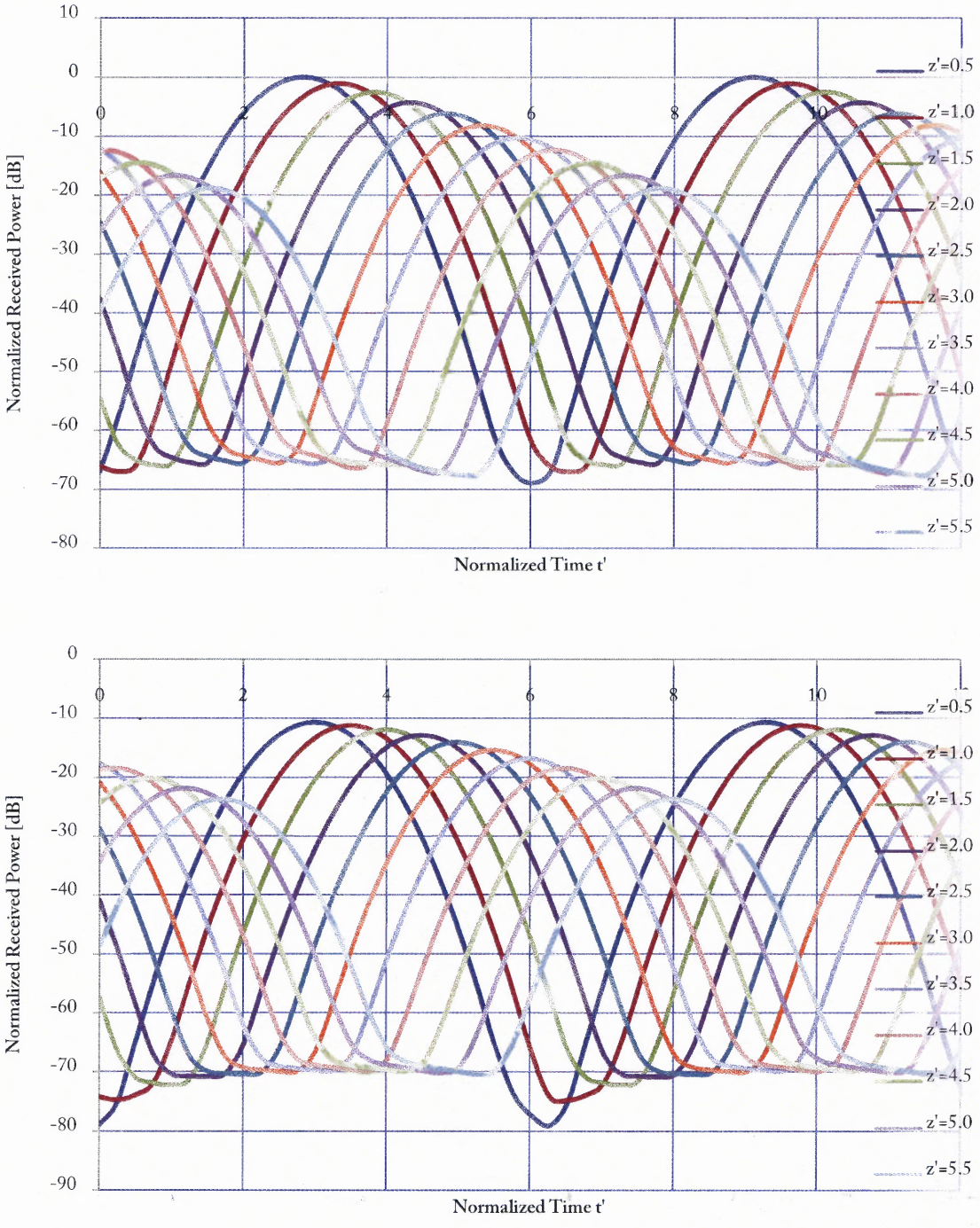

Figure 31 Normalized received power for $n=1000$, $\rho'=1.5$ (top) and $\rho'=4$ (bottom), $\theta=0°$, and $\psi=0°$ versus different values of z'

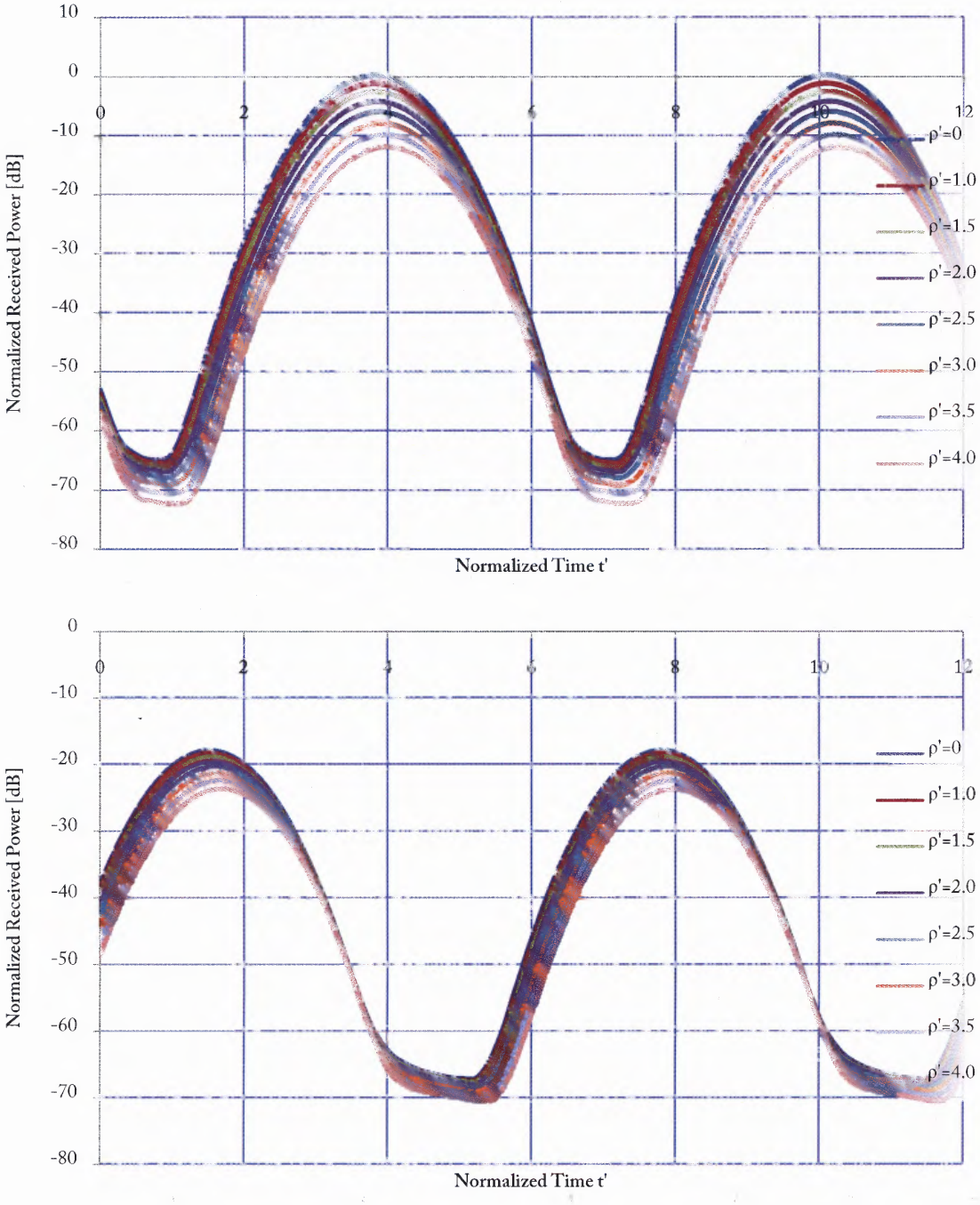

Figure 32 Normalized received power for $n=1000$, $z'=1.5$ (top) and $z'=5.5$ (bottom), and $\psi=0°$ versus different values of ρ'; note: at $\theta=0°$, the received power has contributions directly from the incident beam.

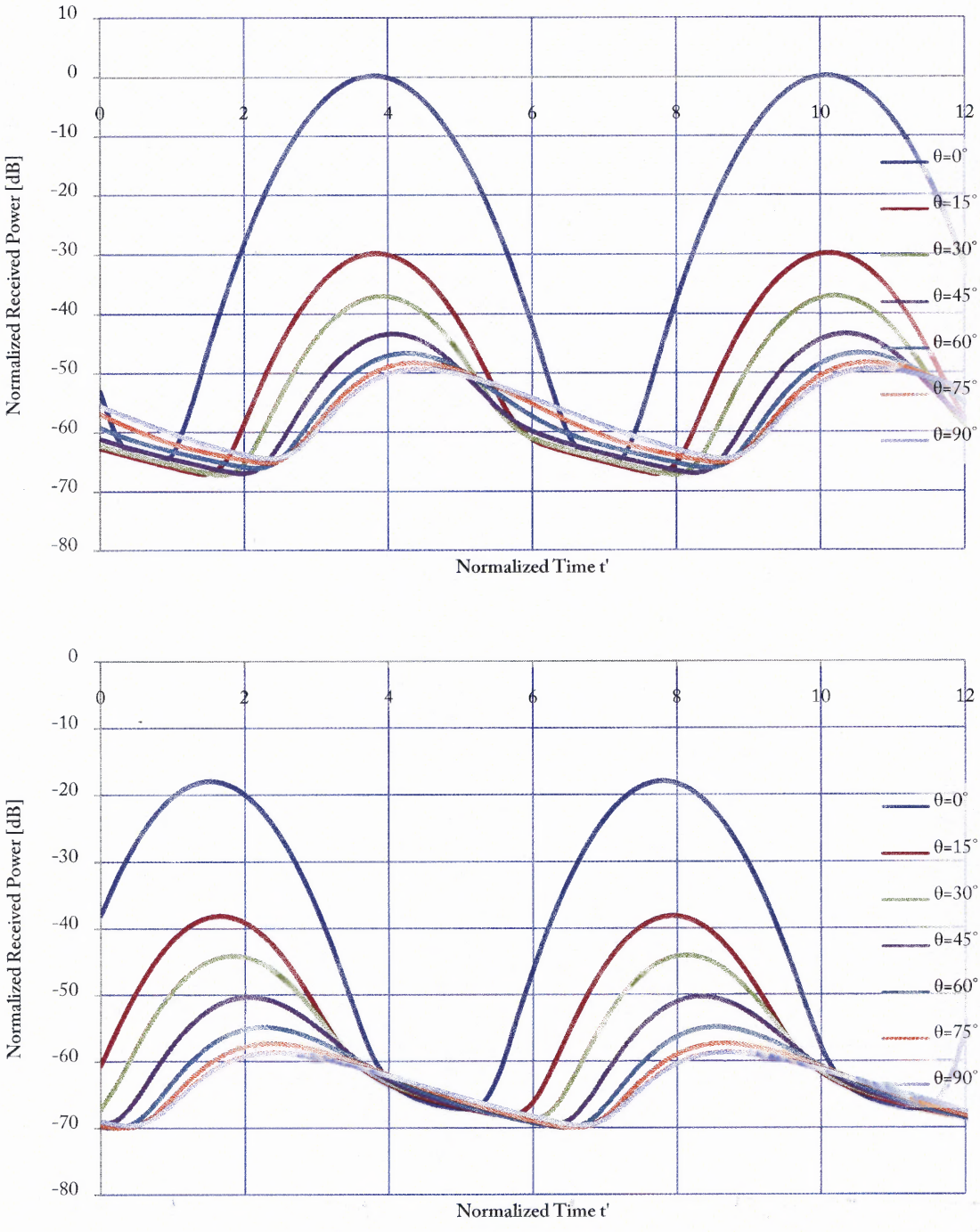

Figure 33 Normalized received power versus normalized time for $n=1000$, $\rho'=0.0$, $z'=1.5$ (top) and $z'=5.5$ (bottom), and $\psi=0°$ versus different values of θ; note: at $\theta=0°$, the received power has contributions directly from the incident beam.

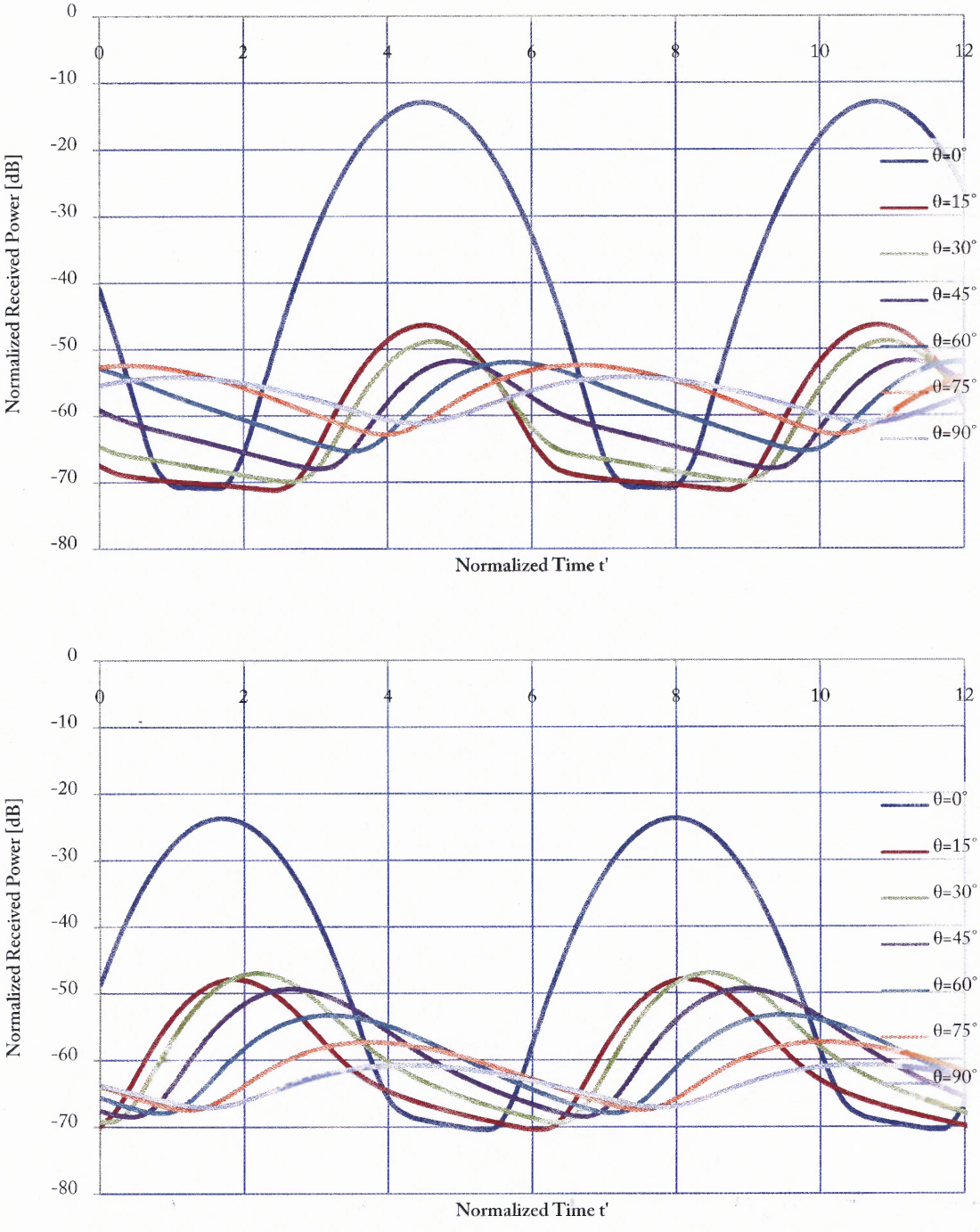

Figure 34 Normalized received power versus normalized time for $n=1000$, $\rho'=4.0$, $z'=1.5$ (top) and $z'=5.5$ (bottom), and $\psi=0°$ versus different values of θ; note: at $\theta=0°$, the received power has contributions directly from the incident beam.

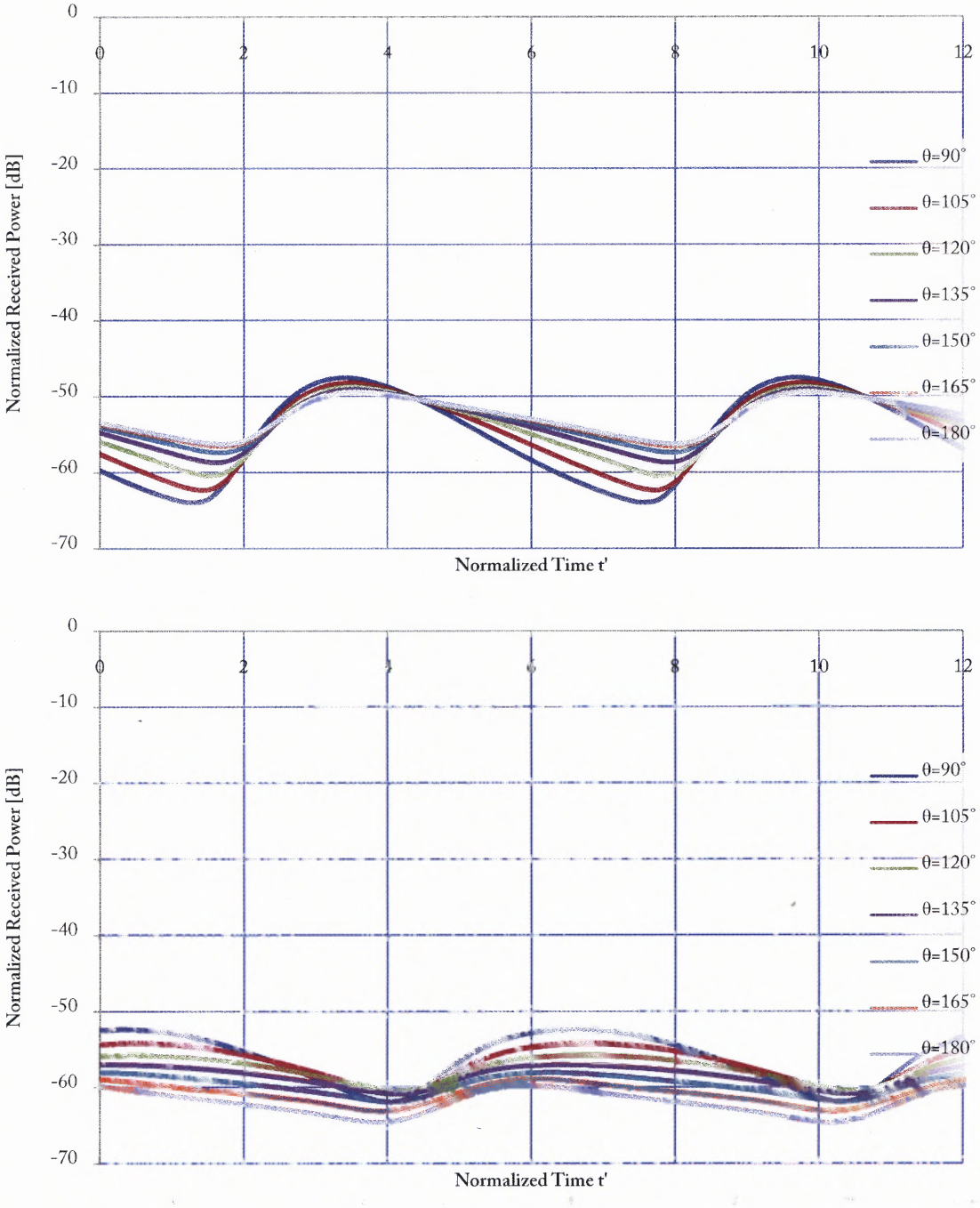

Figure 35 Normalized received power versus normalized time for $n=1000$, $(\rho',z')=(0,0.5)$ (top), $(\rho',z')=(2.5,2.5)$ (bottom), and $\psi=0°$ versus different values of θ.

CHAPTER 5

CONCLUSION

The scalar time-dependent equation of radiative transfer was used to develop a theory of divergent beam wave pulse propagation and scattering in vegetation, a medium characterized by many random discrete scatterers which scatter energy strongly in the forward scattering direction. The specific problem analyzed is that of a spherically divergent beam wave pulse train with θ-dependent cosine radiation pattern incident from free-space onto the planar boundary surface of a random medium, half-space, such as a forest, that possesses a power scatter (phase) function consisting of a strong, narrow forward lobe superimposed over an isotropic background. After splitting the specific intensity into the reduced incident and the diffuse intensities, the solution of the transport theory expressed in cylindrical coordinates was obtained by expanding the angular dependence of both the scattering function and the diffuse intensity in terms of Associate Legendre functions, by using a Fourier series/Hankel transform to obtain the equation of transfer for each spatial frequency, and by satisfying the boundary conditions that the forward traveling diffuse intensity be zero at the interface and zero at infinity.

Plots of intensity and received power in the random medium (forest) showed distortion due to pulse broadening, power attenuation (especially at large penetration depths), beam angular spreading and out-of-beam scattering.

APPENDIX A

TIME-DEPENDENT TRANSPORT EQUATION

The time-dependent transport equation—an integro-differential equation for the specific intensity $\mathbf{I}(\mathbf{r},t;\hat{s})$—is defined as the flow of power per unit area and per unit solid angle at position $\mathbf{r}$ and time t, crossing a surface perpendicular to the direction of the travelling scattered wave $\hat{s}$.

$$\mathbf{I}(\mathbf{r},t;\hat{s}) = \frac{\Delta \mathbf{P}(\mathbf{r},t;\hat{s})}{\Delta S \Delta \Omega} \qquad \left[\frac{\text{watts}}{\text{m}^2\text{rad}^2}\right] \tag{97}$$

where $\Delta \mathbf{P}(\mathbf{r},t;\hat{s})$ is the differential power.

To derive the transport equation, a beam of radiation is assumed to flow along a path in direction $\hat{s}$ through a medium characterized by absorption σ_a and the scattering σ_s cross-sections. In the medium, a cylindrical volume element with a cross-sectional area of $\Delta \mathbf{S}$ and length Δr that surrounds a segment of the path is constructed. Let the specific intensity at $\mathbf{r}$ and t be $I(\mathbf{r};t,\hat{s})$; hence, at $\mathbf{r} + \Delta \mathbf{r}$ and at $t + \Delta t$,

$$\mathbf{I}(\mathbf{r} + \Delta \mathbf{r}, t + \Delta t; \hat{s}) = \mathbf{I}(\mathbf{r},t;\hat{s}) + \Delta \mathbf{I} \tag{98}$$

where $\Delta \mathbf{I}$ is the change in intensity, occurring between position $\mathbf{r}$ at time t and $\mathbf{r} + \Delta \mathbf{r}$ and $t + \Delta t$.

The difference in the radiant energy ΔW between the wave entering into the volume element at $\mathbf{r}$ and the wave exiting it at $\mathbf{r} + \Delta \mathbf{r}$ through the cross-sectional area ΔS during a time interval Δt is given by

$$\Delta W = \Delta \mathbf{I} \Delta \mathbf{S} \Delta \Omega \Delta t \qquad \text{[joules]} \tag{99}$$

Hence, the net gain in energy per unit volume is

$$\mathbf{W}_e = \frac{\Delta W}{\Delta V \Delta\Omega \Delta t} = \frac{\Delta \mathbf{I}}{\Delta \mathbf{r}} \qquad \left[\frac{\text{watts}}{\text{m}^3 (\text{rad})^3}\right]. \tag{100}$$

Since the spherical intensity on the vegetation medium propagates at the speed of light, the distance traveled in time Δt is $\Delta r = c\Delta t$; hence, (100) becomes

$$\mathbf{W}_e = \frac{1}{c}\frac{d\mathbf{I}}{dt}. \tag{101}$$

The total or the substantial derivative of the intensity is given by

$$\frac{d\mathbf{I}}{dt} = \frac{\partial \mathbf{I}}{\partial t} + \frac{\partial \mathbf{I}}{\partial x}\frac{\partial x}{\partial t} + \frac{\partial \mathbf{I}}{\partial y}\frac{\partial y}{\partial t} + \frac{\partial \mathbf{I}}{\partial z}\frac{\partial z}{\partial t} = \frac{\partial \mathbf{I}}{\partial t} + \frac{d\hat{r}}{dt}\cdot\nabla\mathbf{I} \tag{102}$$

where

$$\begin{aligned} d\mathbf{r} &= \hat{x}dx + \hat{y}dy + \hat{z}dz = \hat{r}dr \\ \nabla\mathbf{I} &= \hat{x}\frac{\partial \mathbf{I}}{\partial x} + \hat{y}\frac{\partial \mathbf{I}}{\partial y} + \hat{z}\frac{\partial \mathbf{I}}{\partial z} \end{aligned} \tag{103}$$

and $\hat{x}, \hat{y}, \hat{z}$, and $\hat{r}$ are unit vectors. Since $d\mathbf{r} = \hat{r}dr = \hat{r}cdt$, (101) and (102) yield

$$W_e = \frac{1}{c}\frac{d\mathbf{I}}{dt} = \frac{1}{c}\frac{\partial \mathbf{I}}{\partial t} + \hat{r}\cdot\nabla\mathbf{I} \tag{104}$$

The net gain in the radiative power W_e is given by

$$W_e = -W_{abs} - W_{scat} + W_{in-scat}, \tag{105}$$

where the loss of energy due to absorption is given by

$$W_{abs} = \sigma_a \mathbf{I}(\mathbf{r}, t; \hat{s}), \tag{106}$$

the loss due to scattering by

$$W_{scat} = \sigma_s \mathbf{I}(\mathbf{r}, t; \hat{s}), \tag{107}$$

and the gain due to in-scattering from all directions is

$$W_{in-scat} = \frac{\sigma_S}{4\pi} \iint_{4\pi} p(\hat{s},\hat{s}')\mathbf{I}(\mathbf{r},t;\hat{s}')d\Omega' \tag{108}$$

with normalized scatter (phase) function $p(\hat{s},\hat{s}')$. Implicit in writing (106)-(108) is the assumption that the scatter medium free of dispersion. Therefore, all of the parameters characterizing the medium are independent of the frequency. Combining (101) to (108) yields the time-dependent transport equation:

$$\frac{1}{c}\frac{\partial \mathbf{I}}{\partial t} + \hat{s}\cdot\nabla\mathbf{I} = -(\sigma_a + \sigma_s)\mathbf{I} + \frac{\sigma_s}{4\pi}\iint_{4\pi} p(\hat{s},\hat{s}')\mathbf{I}(\mathbf{r},t;\hat{s})d\Omega'. \tag{109}$$

APPENDIX B

DIVERGENCE BEAM TO COLLIMATED BEAM

The pattern function for the divergence incident beam is as:

$$F(\mu_0) = 2(n+1)\mu_0^n, \tag{110}$$

where $\mu_0 = \cos\theta_0$ and $\sin\theta_0 = \frac{\sqrt{1-\mu_0^2}}{\mu_0}$. The collimated incident beam takes the following form:

$$I_{INC} = S_p e^{-(\rho'/w')^2}. \tag{111}$$

Since the Gaussian term ($e^{-(\rho'/w')^2}$) in (111) and the power term (μ_0^n) in (110) have maximum of one, it is easy to equate them to half in order to compare between the collimated beams and the divergence beams:

$$\mu_0^n = \frac{1}{2} \text{ and } e^{-(\rho'/w')^2} = \frac{1}{2}. \tag{112}$$

Since the interest is at the forest boundary, where $z' = 0$,

$$\rho' = z_0' \tan\theta_0 = z_0' \frac{\sqrt{1-\mu_0^2}}{\mu_0} = z_0' \sqrt{\mu_0^{-2} - 1}. \tag{113}$$

Solving for μ_0 in (112) gives

$$\mu_0 = 0.5^{1/n}, \tag{114}$$

which then gets substituted back into the Gaussian term in (112) along with (113) to reveal that

$$0.5 = e^{-\left(z_0'\sqrt{2^{2/n}-1}/w'\right)^2}. \tag{115}$$

Solving for w' gives the following expression:

$$\sqrt{\ln 2} = \sqrt{\left(z_0' \sqrt{2^{2/n} - 1} / w'\right)^2}$$
$$\therefore w' = z_0' \sqrt{\frac{2^{2/n} - 1}{\ln 2}} \quad . \tag{116}$$

Solving for n in (116) reveals that

$$n = \frac{2 \ln 2}{\ln\left[\left(\frac{w'}{z_0'}\right)^2 \ln 2 + 1\right]} . \tag{117}$$

For example when $n = 1000$ and $z_0' = 40$, the equivalent collimated beam width will be, based on (116),

$$w' = 40 \sqrt{\frac{2^{2/1000} - 1}{\ln 2}} = 1.790 . \tag{118}$$

The requirement to use the half-power beam width equivalence is that the transmitting antenna pattern beam width has to be narrow, i.e. n has to be very large ($n \gg 0$), so that the diverging beam can be close to the collimated beam. In this research, a narrow divergent beam (n=1000) is used in the simulations.

APPENDIX C

CODES

This short script is written in MATLAB and is used to observe the forcing function quickly without going through a significant amount of calculations.

Example to obtain k_{max} : k = 0:0.01:5 ; G = geng(k , 1 , 0 , 0 , 1000 , 40) ; plot(k , G)

```
function G = geng( k_ , z_ , m , l , n , z0 )
i = 0 ; j = 0 ; k = 0 ;
G = zeros( length( k_ ) , l ) ;

[gw , gx] = gaussQuad96( ) ; % 48-point Gaussian Quadrature weights and values
gw = [ gw gw ] ;
gx = [ -gx gx ] ;
ax = ( 1E-10 / ( 2 * n + 2 ) ) ^ ( 1 / n )
bx = 0.5 * ( 1 - ax ) ;
ax = 0.5 * ( ax + 1 ) ;
k_i = 0 ;
T = zeros( length( gx ) , 1 ) ;
for i = 1 : length( gx ) ;
  x = bx * gx( i ) + ax ;
  L = legendre( l , x ) ;
  T( i ) = ( 2 * n + 2 ) * x^( n - 1 ).* L( m + 1 ) ;
end

for k__ = k_
  k_i = k_i + 1 ;
  g = 0 ;
  j = 0 ;
  for x = bx * gx + ax
    j = j + 1 ;
    kk = k__ * sqrt( 1 ./ ( x .* x ) - 1 ) ;
    g = g + exp( -z_ / x ) .* besselj( m , kk * ( z_ + z0 ) ) * gw( j ) * T( j ) ;
  end
  G( k_i ) = G( k_i ) + g * ax ;
end
```

REFERENCES

1. Ishimaru, A. (1978). Wave Propagation and Scattering in Random Media, vol.1. New York: Academic Press.

2. Chandrasekkar, S. (1960). Radiative Transfer. New York Dover.

3. Case, K. and Zweifel, P. (1969). Linear Transport Theory. Upper Saddle River, NY: Addison Wesley.

4. Ozisik, N. M. (1973). Radiative Transfer and Interactions With Conduction and Connection. New York: Wiley.

5. Weinberg, A. and Weigner, E. (1958). The Physical Theory of Neutron Chain Reactions. Chicago, IL: University Chicago.

6. Whitman, G. M., Schwering, F. K., Triolo, A., & Cho, N. (1996, January). A Transport Theory of Pulse Propagation in a Strongly Forward Scattering Random Medium. IEEE Transactions on Antenna & Propagation, 44 (1), 118-128.

7. Schwering, F. K., Violette, E. J., and Espeland, R. H. (1988, May). Millimeter-Wave Propagation in Vegetation: Experiments and Theory. IEEE Transactions on Geoscience and Remote Sensing, 26 (3), 355-367.

8. Schwering, F. K. and Johnson, R. A. (1986, April). A Transport Theory of Millimeter-Wave Propagation in Woods and Forests. J. Wave-Material Interaction, 1 (2), 205-235.

9. Whitman,G.M., Schwering,F.K., & Yuan,J. (1985, August). Chebyshev Method of Solution to the Time-Dependent Transport Equation in Planar Geometry. Proceedings of the 1985 International Symposium on Antennas and EM Theory (pp. 171-177). Beijing, China: China Academic Publishers.

10. Whitman,G. M., Schwering,F.K., & Cho,N. (1985, August). Moment Method Solution of the Time Dependent Transport Equation in Planar Geometry. Proceedings of the 1985 International Symposium on Antennas and Propagation (pp. 687-690). Kyoto, Japan.

11. Whitman,G.M., Scherwing,F.K., Wu,M.Y. (2007,June).Collimated Beam Wave Pulse Propagation and Scattering in Vegetation Using Scalar Transport Theory. IEEE Transactions on Antennas and Propagation 55(6), 1599-1612.

12. Markel,V.A. (2000) Modified Spherical Harmonics Method for Solving the Radiative Transport Equation. Waves in Random Media, 14, pp. L13-L19.

13. Ulaby,F.T., Van Deventer,T.A., East,J.R., Haddock,T.F., & Coluzzi,M.E. (1988, May). Millimeter-Wave Bistatic Scattering from Ground Vegetation Targets. IEEE Transactions on Geoscience and Remote Sensing, 26 (26), 229-243.

14. Anderson,E., Bai,Z., Bischof,C., Blackford,S., Demmel,J., Dongarra,J., Du Croz,J., Greenbaum,A., Hammarling,S., McKenney,A., & Sorensen, D. (1999). LAPACK Users' Guide (third edition). Philadelphia, PA: Society for Industrial and Applied Mathematics. http://www.netlib.org/lapack/lug/lapack_lug.html (1999, October 1).